SEARCHING FOR SUPERSYMMETRY WITH SAME-SIGN DI-LEPTONS USING THE
CMS EXPERIMENT AT THE LARGE HADRON COLLIDER

By

RONALD C. REMINGTON

A DISSERTATION PRESENTED TO THE GRADUATE SCHOOL
OF THE UNIVERSITY OF FLORIDA IN PARTIAL FULFILLMENT
OF THE REQUIREMENTS FOR THE DEGREE OF
DOCTOR OF PHILOSOPHY

UNIVERSITY OF FLORIDA

2011

ACKNOWLEDGMENTS

me to settle on which type of research I would pursue for my PhD. During my first year on CMS I had the fortune of working along side Bobby Scurlock, Rick Cavanaugh, and Mike Schmitt. Their guidance and mentorship provided me with the tools I needed to make meaningful contributions to the CMS community very early on. Working with them was a true delight, and I feel that much of the success I have enjoyed during my graduate career can be attributed to each of them in some way.

The endless love and support of my family has helped me to persevere through the frequent and arduous periods of long work hours, sleepless nights, and imposing deadlines. My wife Jeannette has endured this process since the day I declared my major as an undergraduate and she has been unwavering in her support during each subsequent phase in my long path to becoming a physicist. The role of a graduate student's spouse is far from glamorous and can be incredibly unfulfilling. Jeannette has nonetheless been utterly committed to seeing this through, even as the demands of my research began to significantly compromise her own career aspirations, a price that could have been easily viewed as to much to bear. She endorsed the idea of moving to CERN when she did not have to, because she knew it would bring me better opportunities. She humbled herself to working as an overqualified au-pair while we lived there in order for us to make ends meet. Her sacrifices have been far greater than mine during this process, and for that I am greatly indebted. This dissertation is a tribute to my love, Jeannette.

TABLE OF CONTENTS

LIST OF TABLES

LIST OF FIGURES

Abstract of Dissertation Presented to the Graduate School
of the University of Florida in Partial Fulfillment of the
Requirements for the Degree of Doctor of Philosophy

SEARCHING FOR SUPERSYMMETRY WITH SAME-SIGN DI-LEPTONS USING THE
CMS EXPERIMENT AT THE LARGE HADRON COLLIDER

By

Ronald C. Remington

August 2011

Chair: John Yelton
Major: Physics

The year 2010 marked the beginning of a new era in collider physics as the Large
Hadron Collider (LHC) began colliding proton beams at a record-setting, center-of-mass
energy of 7 TeV. The work described herein represents one of the first efforts to search
for evidence of R-parity conserving supersymmetry (SUSY) using the Compact Muon
Solenoid (CMS) experiment at the LHC. The analysis exploits an event topology based
on same-sign di-leptons, hadronic jets, and missing transverse energy. This signature is
expected to be featured in a variety of new physics scenarios and is known to be heavily
suppressed by the Standard Model. The search uses data produced during the 2010
LHC run, corresponding to $\int L \, \mathrm{d}t = 35$ pb^{-1}. An extensive overview of the data-driven
methods used to model the behavior of background processes is given. After imposing
the event selection requirements that define the signal region, 1 event is observed,
which is statistically consistent with the total expected Standard Model background
rate of 0.80 ± 0.33. Given this lack of an excess, exclusion limits are calculated on the
parameter space of SUSY models with universal gaugino and scalar mass scales. The
general limit on cross-section σ multiplied by branching ratio BR and the event selection
acceptance $A^{\mathrm{experiment}}$ is $\sigma \times BR \times A^{\mathrm{experiment}} < 13$ pb at 95% C.L. In order to make the
results of this search accessible to the wider theoretical community, a parameterization
of the experimental acceptance is presented. Using this parameterization, the viability

of a large class of new physics models, not restricted to supersymmetry, can be tested against the limits set by this search.

CHAPTER 1
INTRODUCTION

The year 2010 marked the beginning of a new era in collider physics. The Large

Hadron Collider (LHC) surpassed the energy frontier, formerly set by the Tevatron, by

colliding proton beams at a center-of-mass energy of 7 TeV. The main goal of the LHC

is to succeed where its predecessors have failed, and finally elucidate the nature of

electroweak symmetry breaking (EWSB), which is the hypothesized mechanism for

imparting masses to the fundamental particles of nature. The particle that is expected

to be responsible for EWSB is the Higgs boson, which today remains the only particle

predicted by the Standard Model of particle physics to elude observation.

While discovery of the Higgs boson would be a true triumph of the Standard Model,

it would not mark the end of the story. The path to understanding the laws of physics

at nature's most fundamental level must extend beyond the Standard Model for several

reasons which will be described in Chapters 2 and 3. The Higgs hypothesis, if proven

to be true, invites further speculation about the existence of potentially numerous other

particle states, previously not included in the Standard Model. This speculation can be

attributed to the unique qualities of the Higgs particle that distinguish it from all others in

the Standard Model, namely its quantum spin and its ground state energy. Many believe

that in order for the Higgs boson to fit consistently into the Standard Model, a new

symmetry of nature must be invoked. This symmetry is referred to as *supersymmetry*

and its existence implies that a host of new and exotic particle states might be created

in high-energy particle collisions. The search for evidence of supersymmetry using data

recorded by the Compact Muon Solenoid (CMS) experiment at the LHC is the focus of

this dissertation.

The laws of special relativity and quantum mechanics, when combined, yield

important consequences which provide the underlying principles exploited by collider

physics experiments. Special relativity demonstrated the equivalence between mass and

energy via Einstein's famous equation $E = mc^2$. Quantum mechanics demonstrated that small distances (ΔX) can be related to large energies (ΔE) via Heisenberg's famous uncertainty principle $\Delta E \cdot \Delta X \geq \hbar c$. These two theoretical insights imply that particles are not indestructible objects, but that they can be annihilated or created if the conditions are right, i.e. if $\Delta E \approx 2mc^2$, and if other conservation laws are satisfied. The main function of particle colliders is to create the appropriate conditions for particle creation, in essence, by forcing two particles into a small enough ΔX. Clearly, if one wants to manufacture very massive particles, then one needs to accelerate the colliding particles to very high energies.

The laws of quantum mechanics prohibit a deterministic outcome to any particular particle collision. Instead, all outcomes are probabilistic. The Standard Model can be viewed as the master probability distribution function of particle interactions. It provides a prescription for calculating the probabilities of particular outcomes, which are typically manifested as *scattering cross-sections*. Rare outcomes (e.g., production of heavy particles) are characterized by small cross-sections. For example, Higgs particle production at the LHC is expected to have a cross-section of order picobarns (1 pb $= 10^{-36}$ cm^2). It is much more likely to produce light particles, like pairs of quarks, which have cross-sections of order millibarns (1 mb $= 10^{-27}$ cm^2). There are, of course, other factors besides mass that influence the production cross-sections of various outcomes, for instance the strength of the force that is mediating the interaction and the attributes of the colliding particles. From the qualitative discussion of these respective cross-sections, it is clear that for every one collision resulting in the production of a Higgs particle, there will be billions of collisions resulting in the production of mundane (and usually uninteresting) particles. For this very reason, it is essential that a collider can not only produce high-energy collisions, but can also produce them very rapidly. This is a unique feature that truly sets the LHC apart from its predecessors: it is designed to cross proton beams at a rate of 40 million times per second with 25

nanosecond intervals. Each crossing can produce up to 20 distinct collisions, yielding a nominal collision rate of 1 GHz. More details will be discussed on the technical aspects of the LHC in Chapter 4.

When discussing quantities in the context of high-energy physics it is convenient to do so using the convention of *natural units*. This requires one to modify the definitions of two constants of nature: the speed of light in a vacuum c, and Planck's quantum of action $\hbar$. Normally, these have dimensions:

$$[c] \quad = \quad \text{(length)} \cdot \text{(time)}^{-1}, \tag{1--1}$$

$$[\hbar] \quad = \quad \text{(length)}^2 \cdot \text{(mass)} \cdot \text{(time)}^{-1}. \tag{1--2}$$

In natural units, they become dimensionless and are set to unity, i.e.,

$$\hbar = c = 1. \tag{1--3}$$

In this scheme the units of mass and momentum are unified with that of energy, which typically is measured in eV (electron-volts). The characteristic energy scale of physics at the LHC is the GeV (or TeV) which is equivalent to 10^9 eV (or 10^{12} eV). Another meaningful consequence of Eq. 1–3 relates to Newton's gravitational constant G. In natural units it takes on dimensions of inverse mass-squared, i.e.

$$[G] = \frac{1}{M_p^2}. \tag{1--4}$$

Thus, the force of gravity becomes associated with a mass scale (or equivalently an energy scale), which is typically referred to as the Planck mass, carrying a value of $M_p \sim \mathcal{O}(10^{18}$ GeV$)$. This value has particular importance to theories of physics beyond the Standard Model, which will be revisited in Chapters 2 and 3.

In the context of collider physics, collision energies are quoted in the center-of-mass reference frame,[1] and are denoted by the square-root of the Mandelstam parameter s. The LHC is designed to collide protons at an energy of $\sqrt{s} = 14$ TeV, but due to engineering difficulties has thus far only operated up to $\sqrt{s} = 7$ TeV. This is still significantly higher than that of previous colliders.

The organization of this dissertation is as follows. Chapter 2 provides an overview of the Standard Model of particle interactions, describing its successes and shortcomings. Chapter 3 describes the important aspects of supersymmetry, which is a leading theory for a description of physics beyond the Standard Model. In particular, the experimental signatures of supersymmetry are discussed, with special attention devoted to those which are the focus of this research (e.g., lepton pairs with identical electromagnetic charge plus missing energy). An overview of the design and performance of the LHC is given in Chapter 4. A complete description of the CMS particle detector, the technological challenges of operating in the LHC environment, and the methods required to perform analysis of the data is provided in Chapter 5. Chapter 6 gives a full account of the methods employed and the results obtained in this search for evidence of supersymmetry with the data produced by the LHC during 2010. Finally, some concluding remarks , which are given in Chapter 7, relate to future searches for supersymmetry at the LHC using the signature exploited by this analysis.

---

[1] The frame in which the initial momenta sums to zero

CHAPTER 2
THE STANDARD MODEL OF PARTICLE INTERACTIONS

2.1   Overview and Theoretical Foundation

The Standard Model represents the successful mathematization of nature at a
very fundamental level. Formally, it is a low-energy, effective quantum field theory
of gauge-invariant particle interactions, which has enjoyed huge successes over the
past several decades [1, 2]. It describes three of the four known fundamental forces
with great precision (i.e., electromagnetic, weak, and strong interactions), with the
gravitational force still eluding a consistent quantum description. At the time of writing,
no statistically significant deviations from the predictions of the Standard Model have
been observed, aside from the interesting phenomenon of neutrino oscillations [3–5].
All particles known to exist thus far fit elegantly into the mathematical framework of the
Standard Model.

The dynamics of a physical system can often be elegantly and concisely described
using the Lagrangian formalism. This holds true for both classical and quantum systems,
whether they be relativistic or not. Quantum field theory deals with relativistic particle
states, which are characterized by fields that permeate space-time as plane-waves.
These fields are amenable to a Lagrangian treatment, in that, the fields and their
respective space-time derivatives can be cast as the generalized coordinates in a
configuration space. The *action* $\mathcal{S}$, which represents the time-integral of the Lagrangian
can be minimized accordingly, yielding the so-called Euler-Lagrange equations of
motion which govern the dynamics of the fields. The validity of these equations relies
on Hamilton's principle of least-action, which is a fundamental axiom in physics
that encapsulates the notion that objects travel through configuration space (on
average) along geodesics (i.e., via the most efficient way possible). This principle is
equivalent to the assumption that there is a frugal economy—one in which *action* is the
resource—belonging to all physical systems in the cosmos, regardless of scale.

Lagrangians offer more than simply aesthetic appeal. They are useful for several reasons. First, they provide a convenient way to unveil symmetries. Symmetries are important because they yield conservation laws (i.e., *universal truths*) via Noether's Theorem [6]. For example, the classical laws of momentum and energy conservation are born from the space and time translational symmetries of the Lagrangian governing Newtonian mechanics. Analogous conservations laws can be derived in quantum mechanics. Second, the canonical template of the Lagrangian, representing the difference between kinetic and potential energy, is easy to intuit and carries over naturally to free fields (kinetic terms) and interacting fields (potential terms). If one desires to incorporate new fields or interactions into a theory, it is simply a matter of adding more terms to the Lagrangian, while the preexisting terms remain in most cases unaltered. Finally, a Lagrangian composed of fields can easily be made to yield local interactions. Non-locality or *action at a distance* proved to be one of the most unappealing and experimentally contradictory consequences of some of the earlier classical laws of physics formulated by Newton and Coulomb. By imposing the condition that the fields must be functions of space-time coordinates (i.e., $\phi = \phi(x)$) and that they couple at the same space-time coordinate (i.e., $\phi(x)\phi(y)$ where $x = y$), locality can be made manifest in the Lagrangian, and hence the theory.[1]

A few guiding principles are adopted by (most) theorists when building candidate Lagrangians for quantum field theories that could be realized in nature. In particular, when adding a particle or group of particles to a theory, certain issues need to be addressed. The following subsections will address these issues as they pertain to the Standard Model Lagrangian.

---

[1] Some care has to be made with respect to the number of space-time derivatives that operate on a given field because derivates are tantamount to space-time translations.

2.1.1 Spin

One of the most important attributes of a particle and its quantum field relates to its spin quantum number. Before one can introduce a field or particle into a theory the spin must be known because the mathematical expressions for the fields differ significantly depending on it. Quantum spin represents the intrinsic angular momentum of a particle and has the same dimension as the action $\mathcal{S}$, which is measured in units of Plank's constant $\hbar$ (MKS). In natural units, it is dimensionless ($[\mathcal{S}] = 0$). For massive particles, one can conceptualize spin as the angular momentum about the particle's center of mass. As it turns out, massless particles like photons have spin as well, so this classical analogy can only be extended so far.

Particles known to exist in nature carry spins of 1 (vector bosons) or $1/2$ (spinor fermions). The hypothetical Higgs particle carries zero spin and if discovered would be the first *fundamental scalar boson* to be observed in nature. Table 2-1 provides a brief summary of the generalized Lagrangians and the resulting Euler-Lagrange equations that are used to describe particles of various spins, i.e., scalar, vector, and spinor fields respectively [7–10]. Also shown are the expressions for the respective fields and their dimensions in powers of energy, as well as the propagator. Spin provides a natural way to classify different types of particles, and many observables related to particle interactions have non-trivial consequences as a result of spin (e.g. the angular distribution of decay products $d\sigma/d\Omega$). As will be shown in Chapter 3, supersymmetry, which is an important theoretical extension to the Standard Model, postulates a deep relationship between particles of different spin, and this in turn has profound and far-reaching consequences.

Table 2-1. Summary of fundamental particle fields

Type	Spin	Free Field Lagrangian	Plane Wave Field Expression	Propagator
Scalar	0	$\mathcal{L} = (\partial_\mu \varphi)^\dagger (\partial^\mu \varphi) - m^2 \phi^\dagger \phi$ $\rightarrow (\partial_\mu \partial^\mu - m^2)\varphi = 0$	$\varphi(x) = \frac{1}{(2\pi)^{3/2}} \int \frac{d^3 p}{2E} \left[a(p)e^{-ipx} + b^\dagger(p)e^{ipx} \right]$ $[\varphi] = 1$	$\frac{i}{p^2 - m^2 + i\varepsilon}$
Vector	1	$\mathcal{L} = -\frac{1}{4} F_{\mu\nu} F^{\mu\nu} - m^2 A_\mu A^\mu$ $\rightarrow \left[(\partial_\alpha \partial^\alpha - m^2) g^{\mu\nu} - \partial^\mu \partial^\nu \right] A_\nu = 0$	$A_\mu(x) = \frac{1}{(2\pi)^{3/2}} \sum_\lambda \int \frac{d^3 p}{2E} \left[a_\lambda(p)\varepsilon_\mu^{(\lambda)} e^{-ipx} + a_\lambda^\dagger(p)\varepsilon_\mu^{(\lambda)*} e^{ipx} \right]$ $[A_\mu] = 1$	$\frac{i\left(\frac{p_\mu p_\nu}{m^2} - g_{\mu\nu} \right)}{p^2 - m^2 + i\varepsilon}$
Spinor	$\frac{1}{2}$	$\mathcal{L} = \bar{\psi} \left(i\gamma^\mu \partial_\mu - m \right) \psi$ $\rightarrow \left(i\gamma^\mu \partial_\mu - m \right) \psi = 0$	$\psi(x) = \frac{1}{(2\pi)^{3/2}} \sum_s \int \frac{d^3 p}{2E} \left[c_s(p)u_s(p)e^{-ipx} + d_s^\dagger(p)v_s(p)e^{ipx} \right]$ $[\psi] = \frac{3}{2}$	$\frac{i\left(\not{p} + m \right)}{p^2 - m^2 + i\varepsilon}$

2.1.2 Gauge Invariance

As described earlier, the Lagrangian formalism provides a mathematical framework that is useful for exposing the intrinsic symmetries of a theory. With some basic knowledge of complex algebra, one can easily identify a symmetry belonging to the Lagrangians for scalar and spinor fields. The transformations exposing this symmetry are shown by 2–1 and 2–2, respectively,

$$\phi \rightarrow e^{-i\alpha}\phi, \tag{2–1}$$

$$\psi \rightarrow e^{-i\alpha}\psi. \tag{2–2}$$

This is a symmetry under change of a *global phase*, also known as a *global gauge symmetry*. It is global because the field value at every space-time point is multiplied by a common phase. A more meaningful symmetry would exist if α could take on an arbitrary value at each space-time point. In other words, we require $\alpha = \alpha(x)$, which represents a *local gauge transformation*. At first glance, it appears that such a postulate would have a debilitating effect on the scalar and spinor Lagrangians from Table 2-1. It is quite obvious that they do not allow for such a transformation without permanently altering the form of the Lagrangian. This is due to the derivative terms, which would not longer be blind to α in the exponent. These derivative terms must be present in the Lagrangian to ensure Poincarè invariance, so it appears that local gauge invariance is not possible; however, one could change the definition of the derivative such that $\partial_\mu\phi$ and $\partial_\mu\psi$ are invariant under such a transformation. This can be achieved by introducing the *covariant derivative*, defined as

$$\mathcal{D}_\mu = \partial_\mu - igA_\mu, \tag{2–3}$$

where A_μ is a vector (gauge) field that transforms under a local gauge transformation as

$$A_\mu \rightarrow A_\mu + \frac{1}{g}\partial_\mu\alpha(x). \tag{2–4}$$

The prescription for imposing local gauge invariance on a quantum field theory has far reaching implications. We immediately see that all spinor and scalar fields are now coupled to a vector field via their respective covariant derivatives. When two fields are coupled, they interact with one another. Thus, when local gauge invariance is satisfied, dynamics (force exchanges) emerge as a result.

The vector fields that facilitate the dynamics are appropriately named gauge fields, and the particles that represent the quanta of the fields are known as gauge bosons or force carriers. As an example, we can think of ψ as the electron field, in which case, A_μ represents the photon field, and g would be the *coupling constant* related to the electromagnetic charge, or the strength of the electromagnetic force. The symmetry in this example is produced by a single generator α which represents the transformation properties of the $U(1)$ symmetry group.

Additional types of symmetry groups are used to introduce the weak and strong interactions to the Standard Model. The former is a product of gauge invariance under an $SU(2)$ transformation while the latter comes from gauge invariance under an $SU(3)$ transformation. There are many ways to represent $SU(N)$ symmetries in a theory. The Standard Model invokes the *adjoint* representation of these symmetry groups, which generates $N^2 - 1$ massless gauge fields or vector gauge bosons with spin = 1. This treatment implies the existence of 3 bosons to communicate the weak interaction and 8 bosons to communicate the strong interaction. Thus, instead of simply a single gauge field like A_μ in 2–4, the covariant derivative incorporates 3 more for weak interactions, denoted W_μ^a where $a = 1, 2, 3$ and an additional 8 more for strong interactions, denoted G_μ^b where $b = 1, ..., 8$. These have been experimentally verified to exist and are referred to as weak vector bosons and gluons respectively. Together, the three gauge

symmetries of the Standard Model combine to yield a Lagrangian that is gauge invariant under the transformation laws of $SU(3)_C \otimes SU(2)_L \otimes U(1)_Y$.[2]

The coupling constants that multiply the gauge fields in the covariant derivatives are dimensionless parameters. They are often denoted g', g, and g_s[3] and represent the strengths of the electromagnetic, weak, and strong forces respectively. These are free parameters of the theory in the sense that they are not theoretically constrained and can take on any values whatsoever. They have to be measured by experiment and inserted into the Standard Model Lagrangian by hand in order to make predictions. Table 2-2 summarizes the fundamental forces generated by the gauge fields of the Standard Model. As is evident, the weak bosons are observed to have non-zero masses, which breaks the gauge symmetry. This is the subject of electroweak symmetry breaking (EWSB), an interesting and necessary feature of the Standard Model, which will be discussed in Section 2.1.5.

Table 2-2. Summary of fundamental forces [11]

Force	Carrier	Symbol	Mass (GeV/c^2)	Range (m)
Electromagnetic	photon	γ	0	∞
Weak	2 charged bosons	$W^\pm$	80.4	$\sim 10^{-18}$
	1 neutral boson	Z	91.2	
Strong	gluons	g	0	$\sim 10^{-15}$

In principle, the Lagrangian could accommodate other gauge symmetries, but these would have experimental consequences, in that, additional particles and particle interactions would be observed depending on the strength of the resulting couplings.

---

[2] The subscripts C, L, Y, denote "Color", "Left", and "Hypercharge" respectively.

[3] These are also commonly denoted as α_1, α_2, and α_3, respectively.

More information on the role of gauge invariance and symmetry groups in quantum field theory can be found in Refs. [7–10].

2.1.3 Scale Dependence and Renormalizability

In relativistic quantum field theory, particles propagate through space-time in a complicated way. Consider a photon traveling from point a to point b. At every point in between a and b, there is a non-zero chance (probability) that this photon could split into a particle-antiparticle pair (e.g., an electron and positron) for an instant before subsequently re-annihilating back into a photon. This is allowed by the Heisenberg uncertainty principle. The interaction would be prescribed by a term like the one introduced by the covariant derivative acting on a spinor field in the Lagrangian, i.e., $\bar{\psi} i \gamma^\mu \mathcal{D}_\mu \psi$. Depicted by the Feynman diagram in Figure 2-1A, this phenomenon represents a *virtual* process known as *vacuum polarization*. It is virtual in the sense that the particles produced in the split would not directly be measurable before they annihilated back into a photon. Nonetheless, the integrated effects of this production along the path from a to b do have consequences in other experimental observables. For example, if we imagine that the points a and b represent the interval spanned by an electron-proton bound state (i.e., a hydrogen atom), then we can view the photon as being exchanged from one to the other (e.g. to communicate the force from the electron to the proton), in which case it is also virtual. One such consequence of the quantum loops from vacuum polarization relates to the strength of the charge of the electron as perceived by the proton (and vice versa). The particle-antiparticle pair acts as a charged dipole for the brief instant it exists, and this diminishes the strength of the electric field emanating from the electron as perceived by the proton. In reality there is not just a single photon but a constant flux of photons being exchanged back and forth from the electron to the proton, and all of these photons succumb to this quantum identity crisis while in transit. The net effect of this phenomenon is known as *charge screening*.

Conceptually, it is convenient to think of a cloud of particle-antiparticle pairs swarming the electron and proton. The more distance that separates the two charged particles, the more effective this ephemeral dipole cloud is at diminishing the respective electromagnetic fields of each particle as perceived by the other. Conversely, as the distance that separates two charged particles shortens, the effect of vacuum polarization decreases and a stronger electromagnetic field is perceived. Alternatively, as dimensions of energy and length are inversely related in relativistic quantum physics, it is equivalent to say that the coupling constant, and hence the force, strengthens as higher energies are transferred between the two particles. This phenomenon is aptly referred to as *scale dependence*, and has been verified experimentally [12].

Other observables are susceptible to quantum effects as well. The mass of a particle proves to be another example. As a charged particle propagates through space-time, it is constantly emitting and reabsorbing quanta from the respective gauge fields to which it couples. The simplest case is illustrated in Figure 2-1B, where an electron, for example, is propagating through space from left to right (straight line) while emitting and reabsorbing a photon (wavy line) along the way. Similar to the case of vacuum polarization, this process affects the predicted value of the electron's mass according to the quantum field theory calculations.

A Vacuum polarization   B Self energy
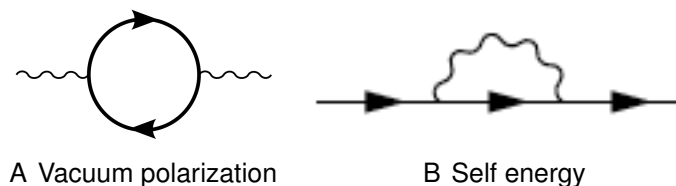
Figure 2-1. Example of Feynman diagrams representing first-order quantum loop corrections

The equations used to predict how an observable will change due to a quantum loop correction often involve integrals of the form

$$a \int_0^\infty \frac{\mathrm{d}x}{x + c}.$$ (2–5)

26

which exhibits a logarithmic divergence at the upper limit $x = \infty$. Observable quantities in nature must by definition be finite, and coupling constants and particle masses are certainly susceptible to experimental measurements. Thus, it is assumed that the infinities are not real, and only reflect our improper mathematical treatment of the problem. Techniques have been developed to reformulate the calculations in such a way that divergent integrals like the one in Eq. 2–5 can be cancelled, leaving a finite and measurable prediction for the quantum correction. Broadly speaking the employment of this procedure is known as *renormalization*. While the mathematical details of renormalization are beyond the scope of this overview, many good references exist on the subject [7, 9, 13]. It was a widely held belief that a theory that tries to describe nature should be renormalizable if it is to have any predictive power. It was demonstrated by Gerardus 't Hooft in the 1970's that all gauge invariant theories exhibit this property [14]. This result placed an even higher premium on gauge invariance. The fact that the Standard Model is gauge invariant, and hence renormalizable, is what makes it a *falsifiable* theory. It has been verified to all energy scales currently accessible by experiment.

2.1.4 Chirality

The expression for the spinor field ψ in Table 2-1 represents a Dirac fermion, which has 4 complex components. This can be interpreted as (2 spin states)$\times$(1 particle state + 1 antiparticle state) = 4 degrees of freedom. Without introducing much more notation, it is sufficient to say that these degrees of freedom can be reshuffled in such a way that the Dirac spinor field can be written as in a pair of complex fields with 2-components as

$$\psi = \begin{pmatrix} \psi_L \\ \psi_R \end{pmatrix}. \tag{2–6}$$

These two components ψ_L and ψ_R can be thought of as two distinguishable particle states (or species) which each transform under different representations of the Lorentz group, i.e., the so-called *left-* and *right-handed* representations respectively. The

27

particles ψ_L and ψ_R are said to have different *chirality*, or *handedness* to use a mundane analogy. Chirality is a rather abstract concept related to a particle's transformation properties; although, in unique circumstances (i.e., in the case that a particle is massless) chirality simplifies to a particle's spin orientation relative to its direction of motion.

The weak interaction, as it turns out, only involves the left-handed component of Dirac spinor fields. Thus, the gauge fields which communicate the weak force (e.g. W^+, W^-, and Z) only couple to ψ_L for all Standard Model fermions. In other words ψ_R does not exhibit the $SU(2)$ gauge symmetry, and is blind to the weak gauge fields. As a consequence, one has to take care to distinguish left-handed fermions from right-handed fermions. One speaks of left-handed electrons and right-handed electrons, for example, as if they are different particles. Owing to the chiral asymmetry of the weak force, this distinction is not an exaggeration, as it has special implications when the theory of supersymmetry is invoked, which will be discussed in Chapter 3.

2.1.5 Spontaneous Symmetry Breaking of the Electroweak Interaction

In Section 2.1.2, the claim was made that the Dirac Lagrangian can be made to be invariant under local gauge transformations by constructing a covariant derivative that adds gauge fields to facilitate each symmetry (e.g. as in 2–3). An implicit assumption was made that the mass term $m\bar{\psi}\psi$ would be unaltered under such a transformation via the relationships shown in 2–7 through 2–9.

$$\psi \quad \rightarrow \quad e^{-i\tau\cdot\alpha(x)}\psi, \tag{2–7}$$

$$\bar{\psi} \quad \rightarrow \quad \bar{\psi}e^{+i\tau\cdot\alpha(x)}, \tag{2–8}$$

$$\therefore m\bar{\psi}\psi \quad \rightarrow \quad m\bar{\psi}\psi. \tag{2–9}$$

However, the weak interaction is *chiral*, meaning it only involves the left-handed components of fermion fields. Thus, only ψ_L transforms as an $SU(2)$ doublet in the same

way as ψ does in 2–7, while ψ_R transforms as a singlet, i.e.,

$$\psi_R \quad \rightarrow \quad \psi_R. \tag{2–10}$$

If the mass term is written explicitly in terms of the ψ_L and ψ_R components as in 2–11, it is clear that the only way to preserve the $SU(2)$ gauge invariance is to impose $m = 0$ for all fermions. A similar lack of gauge invariance was indeed present all along for the mass terms involving the gauge boson fields, although it is unrelated to the issue of chirality.

$$
\begin{aligned}
m\bar{\psi}\psi &= m\left(\bar{\psi}_R\bar{\psi}_L\right)\begin{pmatrix}\psi_L\\\psi_R\end{pmatrix} \tag{2–11}\\
&= m\left(\bar{\psi}_R\psi_L + \bar{\psi}_L\psi_R\right). \tag{2–12}
\end{aligned}
$$

This result presents quite a quandary because the fermions, as well as the weak gauge bosons observed in nature have non-zero masses. Thus, some other mechanism must be invoked, and hence added to the Standard Model Lagrangian, in order to generate masses for these particles.

The simplest and most straightforward solution is to appeal to the Higgs mechanism. The recipe is the following:

(i) Introduce a complex scalar field to the theory and allow it to transform as an $SU(2)$ doublet (i.e., it is 2-vector in $SU(2)$ space). Furthermore, assign it a neutral and charged component, i.e.,

$$\phi = \begin{pmatrix}\phi^+\\\phi^0\end{pmatrix}. \tag{2–13}$$

The combination $\phi^\dagger\phi$ is thus manifestly invariant under an $SU(2)$ transformation.

(ii) Add a new potential interaction V to the Lagrangian which is linear and quadratic in $\phi^\dagger\phi$, i.e.,

$$V(\phi^\dagger\phi) = \mu^2\phi^\dagger\phi + \lambda(\phi^\dagger\phi)^2. \tag{2–14}$$

(iii) Require $\mu^2 < 0$ and solve for the ground state solution to obtain $\langle \phi^\dagger \phi \rangle = -\mu^2/2\lambda$. Define $v = \sqrt{-\mu^2/\lambda}$ to be the ground state energy or the *vacuum expectation value* (VEV or $\langle \phi^0 \rangle$) of the scalar field.

(iv) Perform the $SU(2)$ rotation on ϕ that will set the neutral component of the complex field to this value v. Since a direction in $SU(2)$ space has been preferred by this choice, the $SU(2)$ symmetry is said to be *spontaneously broken*, thus making ϕ a *Higgs field*. By the Goldstone theorem, the gauge fields of the broken symmetry acquire masses, which is manifested in the Lagrangian by the covariant derivative acting on the scalar field ϕ. New mass-like terms of the form $(vg)^2 W_\mu^+ W^{-\mu}$ are now introduced.

(v) The charged fermions acquire masses by directly coupling to the neutral Higgs field via the so-called *yukawa couplings*, λ_ψ, which are free parameters in the theory that have to be measured by experiment. These terms enter the Lagrangian and have the form $\lambda_\psi \bar{\psi} \phi \psi$. Neutral fermions remain massless.

(vi) The Higgs particle represents an excited state of the Higgs field. It has a mass term as well, which is defined as

$$m_H = \frac{1}{2} \lambda v^2. \tag{2--15}$$

The Higgs mechanism has yet to be proven to the be the cause of electroweak symmetry breaking. The Standard Model is not a consistent theory without it. One of the main priorities of the LHC is to demonstrate the existence of the Higgs particle, measure its mass, and thus complete the experimental confirmation of the Standard Model up to TeV energy scales. Strong theoretical and experimental evidence suggests that the Higgs mass should lie in the range of a few hundred GeV [15, 16]. If it is in the 100 GeV range, then the LHC will ultimately reveal its existence in the next few years. Many details of the spontaneous symmetry breaking and the Higgs mechanism are

omitted in favor of the concise description presented above. More details can be found elsewhere [17, 18].

2.2   The Full Particle Description

The fundamental fermions of the Standard Model consists of 3 generations of quarks and leptons, which are summarized in Tables 2-3 and 2-4. They are often arranged in terms of their transformation properties under the $SU(2) \otimes U(1)$ subgroup. The left-handed fermions form $SU(2)$ doublets:

$$\text{L-H Leptons} \quad : \quad \begin{pmatrix} \nu_e \\ e \end{pmatrix}_L, \begin{pmatrix} \nu_\mu \\ \mu \end{pmatrix}_L, \begin{pmatrix} \nu_\tau \\ \tau \end{pmatrix}_L \tag{2–16}$$

$$\text{L-H Quarks} \quad : \quad \begin{pmatrix} u \\ d \end{pmatrix}_L, \begin{pmatrix} c \\ s \end{pmatrix}_L, \begin{pmatrix} t \\ b \end{pmatrix}_L \tag{2–17}$$

The right-handed fermions form $SU(2)$ singlets:

$$\text{R-H Leptons} \quad : \quad e_R, \ \mu_R, \ \tau_R \tag{2–18}$$

$$\text{R-H Quarks} \quad : \quad u_R, \ d_R, \ c_R, \ s_R, \ t_R, \ b_R \tag{2–19}$$

Conspicuously absent amongst the right-handed leptons are neutrinos. Indeed, they have only been observed to exist as left-handed particles, participating only in the weak interaction (i.e., they are electrically neutral). Each fermion has an associated antiparticle, which is not explicit in 2–16 through 2–19.

While all fermions participate in the electroweak interaction, only quarks participate in the strong color interaction, which is mediated by gluons. The strong interactions of the Standard Model are described by the theory of Quantum Chromodynamics (QCD). In section 2.1.3 the scale-dependence of the gauge couplings was described in general terms. The implication was that the effects of *charge screening* diminish the strength of the gauge interactions at large distances. This is only true for the electromagnetic coupling. For the weak and strong couplings, the opposite effect occurs in the Standard Model, i.e., they grow in strength at farther distances. For the weak coupling, this is true

down to the TeV energy scale where electroweak symmetry breaking occurs. Below this scale the strength of the weak coupling diminishes as does the electromagnetic coupling. However, the strong force is blind to electroweak symmetry breaking, and thus continues to strengthen well below the TeV scale. This has very interesting effects on the behavior of color-charged particles. They simply cannot exist in isolation as a result of the *confinement* property of QCD. Quarks can only exist in bound states with other quarks to form color-neutral systems, known as *hadrons*. [4] Hadrons include quark-antiquark bound states (mesons) and tri-quark bound states (baryons).

The LHC will collide protons, a specific type of baryons. The energies transferred in the collisions will be sufficient to disassociate the protons into their constituent partons (quarks and gluons). However, these partons will instantly reassemble into bound states. The potential energy that is gained from the strong coupling as the partons separate during the collision will exceed the $2mc^2$ necessary to create a new pair of quarks from the vacuum. This occurs a multitude of times over until a system of bound state hadrons is formed. This system is aptly called a *jet* and it represents the physical manifestation of a quark or gluon, which has been liberated from a previous bound state.

Table 2-3. Quarks (Spin-1/2) [11]

Name	Symbol	Charge	Mass (GeV)
down	d	$-1/3$	$4.1 - 5.8 \times 10^{-3}$
up	u	$2/3$	$1.7 - 3.3 \times 10^{-3}$
strange	s	$-1/3$	$0.101^{+0.029}_{-0.021}$
charm	c	$2/3$	$1.27^{+0.07}_{-0.09}$
bottom	b	$-1/3$	$4.19^{+0.18}_{-0.06}$
top	t	$2/3$	$172^{+0.9}_{-1.3}$

---

[4] The top-quark is so massive that it decays too quickly to form a bound state. In some sense, it does not live long enough to notice that it should be in one.

Table 2-4. Leptons (Spin-1/2) [11]

Name	Symbol	Charge	Mass (MeV)
electron neutrino	ν_e	0	$< 2 \times 10^{-6}$
electron	e	-1	5.11×10^{-3}
muon neutrino	ν_μ	0	$< 2 \times 10^{-6}$
muon	μ	-1	1.05
tau neutrino	ν_τ	0	$< 2 \times 10^{-6}$
tau	τ	-1	1.77×10^3

2.3 Shortcomings

Despite the wonderful successes of the Standard Model, it is an incomplete theory for several reasons, a few of which are described below.

(i) **Gravity** — The gravitational interactions are not incorporated into the Standard Model framework. Attempts to provide a description of gravity based on quantum field theory have proven to be very challenging. The gravitational coupling constant G is not dimensionless like the couplings of the other fundamental forces. Quantum gravity is thus a non-renormalizable theory.

(ii) **Dark Matter** — Astrophysical evidence suggests that only 4% of the energy in the universe can be accounted for by the particle content of the Standard Model. Roughly 20% is believed to be from a substance known as cold dark matter (gravitationally attractive) and an even more staggering 76% is believed to be some form of a mysterious dark energy (gravitationally repulsive).

(iii) **Matter-Antimatter Asymmetry** — There is no mechanism to explain the preponderance of matter over anti-matter. In fact, the two should be produced in nearly equal amounts according to the Standard Model.

(iv) **Free Parameters** — There are 19 free parameters in the Standard Model, including the fermion masses, the gauge couplings, as well as others. The Standard Model is completely impotent at constraining these to any particular values. They have to be measured by experiments and fed into the theories by hand. Fortunately, they are all accessible by low energy experiments, except for the constant μ multiplying the quadratic term in the Higgs potential, which is expected to be revealed at the TeV energy scale.

(v) **Massive Neutrinos** — The original incarnation of the Standard Model did not accommodate massive neutrinos. The Higgs mechanism imparted masses on the electrically charged fermions, and the non-observation of the right-handed neutrino seemed to preclude the kind of mass term in the Lagrangian that appears

by conventional methods (i.e., the Dirac mass). Proposed extensions to the Standard Model can include neutrino mass terms. One example is the *see-saw mechanism* [19]

(vi) **Hierarchy and Fine Tuning** — Quantum corrections to the Higgs mass involve quadratically divergent integrals, which is an attribute of scalar particles. In order to get a sensible result, the upper limit of the integral must artificially be truncated at some value Λ, which sets the upper bound on the energy range for which the theory is valid. A truly fundamental theory should be valid at least up to the Planck mass scale M_p, as this is where gravitational interactions become important. However, in order to produce a viable Standard Model Higgs particle, the contributions from such a large value of Λ^2 must be cancelled to nearly 20 decimal places by another term in the Lagrangian (i.e., the *bare mass* term). This necessity is known as *fine-tuning*, which renders the theory unnatural. The need for this large-scale cancellation comes by virtue of the Planck scale being ~ 16 orders of magnitude larger than the electroweak scale (set by the Higgs VEV). This vast disparity in energy scales is known as the *gauge hierarchy problem*.

Thus, another theory must eventually take the place of the Standard Model and explain or accommodate many (or all) of the unexplained phenomena described above. Many theoretical extensions to the Standard Model, as well as replacements, have been tried in this pursuit, but ultimately, have been ruled out by experiment. Several theories, however, have not been experimentally testable until now. Their viability will likely be explored by the physics programs at the LHC. Supersymmetry is one such theory, which is the focus of this work and will be discussed in the next chapter.

Some of the shortcomings exhibited by the Standard Model and outlined in

Section 2.3 can actually be overcome by introducing a new relationship between bosons

and fermions. This relationship is referred to as *supersymmetry* (SUSY) and is one

of the leading candidates for a theory that can describe physics beyond the Standard

Model. Formally, supersymmetry is recognized as a property of nature that would allow

scalar and vector bosons to transform into fermions, and fermions to transform into

scalars. Each particle in the Standard Model is hypothesized to have a so-called *su-

perpartner* (sparticle) which maintains the same attributes as the original particle (e.g.,

mass, couplings) but differs by half-integer with respect to the spin-quantum number.

Such a symmetry, if discovered, would have profound consequences.

3.1   The Minimal Supersymmetric Standard Model

The Minimal Supersymmetric Standard Model (MSSM) represents the most efficient

way of extending the Standard Model to include supersymmetric transformations.

3.1.1   Notation

To denote sparticle states symbolically, the convention is to place a tilde over the

original particle symbol, i.e.,

$$\phi \rightarrow \tilde{\phi}, \tag{3--1}$$

$$\psi \rightarrow \tilde{\psi}. \tag{3--2}$$

The names of the superpartners of the Standard Model fermions are prepended

by an "s". Quarks become *squarks*. Leptons become *sleptons*. The names of the

superpartners to the scalar and vector bosons are appended with "ino". Thus, a

supersymmetry transformation of the scalar Higgs boson yields *higgsinos* and

transformations of the vector gauge bosons yield *gauginos*.

3.1.2 Particle Content of the MSSM

The chiral structure of the Standard Model particles carries over to the supersymmetric extension. Because the left- and right-handed components of fermions are considered to be unique particle states with unique transformation properties, it is necessary that they each obtain their own respective superpartners, i.e.,

$$\psi_L \rightarrow \tilde{\phi}_L,$$
$$\psi_R \rightarrow \tilde{\phi}_R. \tag{3--3}$$

The subscripts carried by the scalar sfermions in 3–3 do not imply that they have a *handedness* like spin-$1/2$ particles do. Instead, they are simply meant to denote the respective gauge transformation properties of their superpartners. It is natural to arrange the fermions and their scalar superpartners into *chiral supermultiplets*. This arrangement preserves the distinction between the left- and right-handed particles and allows one to easily integrate the fermions' superpartners into the Lagrangian. Gauge bosons and their fermion superpartners (gauginos) combine to form *gauge supermultiplets*.

Table 3-1 summarizes the Standard Model particles and their respective superpartners. The grouping of particles into supermultiplets indicates their common gauge transformation properties. Rows with common entries in the spin-0 and spin-$1/2$ columns form chiral supermultiplets, while rows with common entries in the spin-$1/2$ and spin-1 columns form gauge supermultiplets. The gauge bosons associated with the electroweak interaction $SU(2)_L \otimes U(1)_Y$ mix after electroweak symmetry breaking to give mass eigenstates Z^0 and γ instead of the gauge eigenstates of W^0 and B^0. The same phenomenon occurs with respect to the gauginos and higgsinos, which yield neutralinos and charginos (Section 3.2.4) as mass eigenstates. The MSSM requires the existence of two Standard Model Higgs $SU(2)$ doublets in order to impart masses to up-type fermions and down-type fermions respectively. Each doublet contains two complex

scalar fields, thus combining to yield 8 degrees of freedom. Three degrees of freedom are used to give masses to the $W^\pm$ and Z bosons. The remaining 5 become Higgs bosons, two of which are electromagnetically charged.

Table 3-1. Summary of particles and superpartners in the MSSM [20]

Name	spin-0	spin-$1/2$	spin-1
squarks, quarks	$(\tilde{u}_L \ \tilde{d}_L)$	$(u_L \ d_L)$	-
	$\tilde{u}_R$	u_R	-
	$\tilde{d}_R$	d_R	-
sleptons, leptons	$(\tilde{\nu}_L \ \tilde{e}_L)$	$(\nu_L \ e_L)$	-
	$\tilde{e}_R$	e_R	-
Higgs, higgsinos	$(H_u^+ \ H_u^0)$	$(\tilde{H}_u^+ \ \tilde{H}_u^0)$	-
	$(H_d^0 \ H_u^-)$	$(\tilde{H}_d^0 \ \tilde{H}_d^-)$	-
gluino, gluon	-	$\tilde{g}$	g
winos, W bosons	-	$\tilde{W}^\pm \ \tilde{W}^0$	$W^\pm \ W^0$
bino, B boson	-	$\tilde{B}^0$	B^0

3.2   Implications of a Supersymmetric Universe

If supersymmetry is realized in nature then the implications are numerous. The MSSM is able to compensate in many areas where the Standard Model proves to be inadequate. The following subsections will outline a few of the interesting consequences of supersymmetry.

3.2.1   Taming the Quantum Corrections to the Higgs Mass

One of the most compelling theoretical justifications for supersymmetry can be found by examining the effects that sparticles would have on quantum corrections to the scalar Higgs mass. As was described earlier, a problem exists which is unique to scalar particles with non-zero VEV's, i.e. the first-order quantum loop correction to their masses has quadratic sensitivity to the energy-scale cut-off, Λ. Because fermions couple directly to the Higgs boson via the yukawa interaction, they too suffer indirectly

from this problem. At first-order, the correction to the Higgs mass takes the form

$$\Delta m_H^2 = \sum_f \quad \lambda_f \quad \lambda_f = \sum_f -\frac{|\lambda_f|^2}{8\pi^2}\Lambda^2 + \mathcal{O}(\ln\Lambda) \qquad (3\text{--}4)$$

 The Feynman diagram represents an integral that accounts for the contribution from all fermions which couple to the Higgs boson. The parameter λ_f represents the Yukawa coupling for each fermion. Thus, this correction is mostly sensitive to the highest mass scale in the Standard Model, which is set by the top-quark, where $\lambda_t \approx 1$. It is fairly obvious from Eq. 3–4, that Λ, which represents the upper limit of the momentum integral, cannot be of order M_P and still preserve the $\Delta m_H^2 = (100 \text{ GeV})^2$ relationship necessary to provide the measured masses to the Standard Model particles. However, if supersymmetry is a property of the universe, then Eq. 3–4 is incomplete, and there is another type of Feynman diagram that is involved in the calculation — one that is due to the scalar superpartners of the respective fermions. Thus, the correction is modified, i.e.,

$$\Delta m_H^2 = \sum_f \quad \lambda_f \quad \lambda_f \quad + \sum_{\tilde{f}} \quad \lambda_{\tilde{f}}$$

$$= \frac{\Lambda^2}{8\pi^2}\left(\sum_{\tilde{f}}\lambda_{\tilde{f}} - \sum_f |\lambda_f|^2\right) + \mathcal{O}(\ln\Lambda). \qquad (3\text{--}5)$$

 The expression given in Eq. 3–5 suggests that the term proportional to Λ^2 can be vanquished if $\lambda_{\tilde{f}} = |\lambda_f|^2$ for each fermion f. If supersymmetry exists then this relationship not only can occur, but is unavoidable [20]. It is simply a statement that the yukawa couplings are identical between superpartners. This is guaranteed to be true, as the only distinction between superpartners is the spin-quantum number. The

fact that the spins are different by a half-integer amount leads to the cancellation. The integrals that arise from the respective Feynman diagrams carry different algebraic signs, owing to the different spin-statistics, and are thus antagonistic.

By taming the quadratically divergent corrections to the Higgs mass, supersymmetry makes the Standard Model a more viable theory. This particular manifestation of the hierarchy problem is conquered.

3.2.2 R-Parity

A rather accidental consequence of the Standard Model are the conserved quantities known as *baryon number* and *lepton number*. Baryon number is defined simply as $B = \frac{1}{3}(n_q - n_{\bar{q}})$ where n_q and $n_{\bar{q}}$ denote the number of quarks and anti-quarks respectively. Lepton number is defined as $L = n_\ell - n_{\bar{\ell}}$, where where n_ℓ and $n_{\bar{\ell}}$ denote the number of leptons and anti-leptons respectively. These quantum numbers pertain to all fermions and are conserved in all Standard Model interactions.[1] The conservation of B and L, for example, explains why proton-decay is not observed in nature.

In the context of the MSSM, it is both convenient and enticing (although not mandatory) to enforce this symmetry by postulating a conserved quantum number called *R-parity*, defined as

$$P_R = (-1)^{3(B-L)+2s} \tag{3–6}$$

Here, s refers to spin quantum number, and ensures that particles within the same supermultiplet have different R-parities. Standard Model particles are thus endowed with even R-parity ($P_R = +1$) while squarks, sleptons, gauginos, and higgsinos are endowed with odd R-parity ($P_R = -1$). If R-parity proves to be a conserved quantum number in

---

[1] Some rare exceptions exist with respect to non-conservation of B due to *chiral anomalies*.

nature (which is both theoretically and experimentally well-motivated), then the following must be true [20]:

- The sparticle with the lowest mass, often called the *lightest supersymmetric particle* or LSP, is stable and cannot decay. If the LSP does not carry an electromagnetic charge, then it only couples weakly to ordinary matter and would thus be difficult to detect. In this case the LSP would prove to be a very promising dark-matter candidate.

- Sparticles must be produced in pairs in order to conserve P_R.

- Each sparticle can decay to an odd number of lighter sparticles. Subsequent sparticle decays will occur until a stable LSP is produced.

Apart from offering a viable and alluring dark matter candidate, the conservation of R-parity has other important phenomenological consequences. These relate to search strategies for experimental evidence of supersymmetry at colliders. A detailed discussion on this topic will be deferred until Section 3.4.

3.2.3 Gauge Coupling Unification

The gauge couplings of the Standard Model are known to scale with the energy transfer of the interaction (see Section 2.1.3). As the energy scale increases, calculations indicate that the couplings come tantalizingly close to crossing at the same value, but unambiguously do not. With additional sparticle states offered by supersymmetry, many natural scenarios exist whereby the gauge couplings unite at a common value near the so-called GUT[2] scale of $\mathcal{O}(10^{16}$ GeV). Sparticles contribute to loop diagrams like the one shown in Figure 2-1A in such a way as to accomplish this unification. This effect is shown graphically in Figure 3-1 [20], where the inverses of the three Standard Model gauge couplings are plotted against the energy scale. This apparent unification at the GUT scale could be evidence of a more fundamental theory, one in which, the electromagnetic, weak, and strong forces merge into a common interaction.

---

[2] Grand Unified Theory.
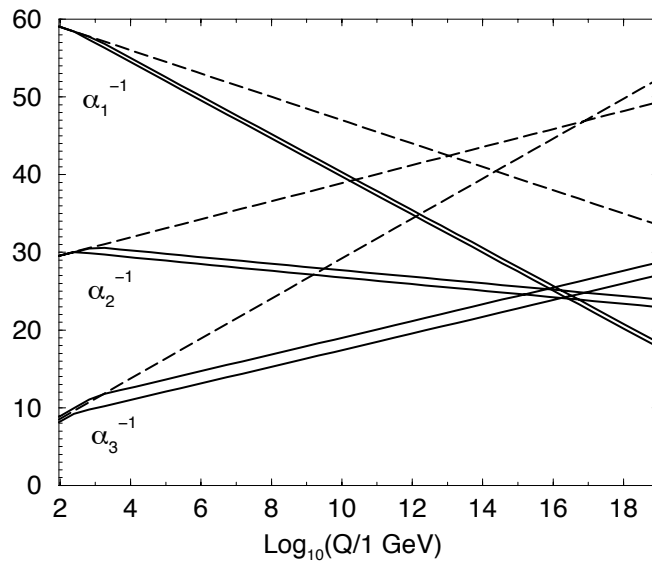
Figure 3-1. Evolution of the Standard Model gauge couplings as a function of energy
scale without (dashed lines) and with (solid lines) Supersymmetry [20]

3.2.4   Sparticle Masses

If the MSSM exists in the form that has been described thus far, then it should have

been discovered decades ago. Extending the Standard Model to include supersymmetry

has the very direct implication that there should be an identical copy of each Standard

Model particle, which carries exactly the same properties with exception to spin. Thus,

spin-0 versions of the electron, muon, and tau should have been produced copiously

in the colliders of decades past. Such sparticles would have been easily detected and

are thus ruled out. To date, no supersymmetric particles have been discovered by any

experimental means. Therefore, if supersymmetry does exist, then the superpartners

are more massive than the energies probed by previous colliders like LEP and Tevatron

(i.e., $\gtrsim 100$ GeV). This can only occur if supersymmetry exists as a broken symmetry.

The breaking of supersymmetry to accommodate heavier sparticle masses is

achieved by adding an additional component to the Lagrangian which gives sparticles

extra mass contributions. It is a *soft* symmetry breaking in the sense that these terms

can still preserve the nice features offered by supersymmetry that were discussed in

Sections 3.2.1, 3.2.2, and 3.2.3. The mechanism by which soft SUSY breaking occurs is the focus of a great body of theoretical work, which is nicely summarized in Refs [20, 21]. While many of the details are beyond the scope here, it is worth mentioning that in its most generic form, soft SUSY breaking introduces 110 new parameters to the theory, none of which have counterparts in the Standard Model. These parameters take the form of 30 masses plus 41 phases plus 39 mixing angles [22].

The addition of soft SUSY breaking terms combined with the electroweak symmetry breaking already introduced into the Standard Model allows for the sparticles of the MSSM to mix. The particular details of the mixing is often model-dependent. The gauge eigenstates of fermion superpartners of the third generation (i.e., $\tilde{t}_L$, $\tilde{t}_R$, $\tilde{b}_L$, $\tilde{b}_R$, $\tilde{\tau}_L$, $\tilde{\tau}_R$) are particularly prone to mixing due to their larger yukawa couplings. Additionally, the neutral higgsinos (H_u^0 and H_d^0) and the neutral electroweak gauginos ($\tilde{B}^0$ and $\tilde{W}^0$) mix to form four mass eigenstates called *neutralinos*. These are denoted χ_i^0, where $i = \{1,2,3,4\}$. The charged higgsinos (H_u^+ and H_d^-) and the winos ($\tilde{W}^\pm$) mix to form two mass eigenstates called *charginos*. These are denoted $\chi_i^\pm$ where $i = \{1,2\}$. A summary of the mass eigenstates of the MSSM is given in Table 3-2.

There is strong evidence to suggest that if supersymmetry exists, and is indeed broken, the masses of the sparticles have to be less than roughly a TeV. This can be inferred from the second order correction to the Higgs mass, which features a term proportional to $\ln \Lambda$. From dimensional analysis this term actually has to have the form

$$\Delta m_H^2 \propto m^2 \ln(\frac{\Lambda}{m}), \tag{3--7}$$

where m represents the respective particle masses. Thus, in order to provide this very important service of keeping the Higgs mass constrained to the experimentally and theoretically favored value, the superpartners cannot be much heavier than a TeV. Indeed, if they do have masses at the TeV scale, then they will in general be produced in great numbers over the lifetime of the LHC.

Table 3-2. Summary of the hypothesized, but still undetected particles of in the MSSM [20]

Name	Spin	R-Parity (P_R)	Gauge Eigenstates	Mass Eigenstates
Higgs bosons	0	+1	$H_u^0\ H_d^0\ H_u^+\ H_d^-$	$h^0\ H^0\ A^0\ H^\pm$
	0	−1	$\tilde{u}_L\ \tilde{u}_R\ \tilde{d}_L\ \tilde{d}_R$	same
squarks	0	−1	$\tilde{s}_L\ \tilde{s}_R\ \tilde{c}_L\ \tilde{c}_R$	same
	0	−1	$\tilde{t}_L\ \tilde{t}_R\ \tilde{b}_L\ \tilde{b}_R$	$\tilde{t}_1\ \tilde{t}_2\ \tilde{b}_1\ \tilde{b}_2$
	0	−1	$\tilde{e}_L\ \tilde{e}_R\ \tilde{\nu}_e$	same
sleptons	0	−1	$\tilde{\mu}_L\ \tilde{\mu}_R\ \tilde{\nu}_\mu$	same
	0	−1	$\tilde{\tau}_L\ \tilde{\tau}_R\ \tilde{\nu}_L\ \tilde{\nu}_\tau$	$\tilde{\nu}_1\ \tilde{\nu}_R\ \tilde{\nu}_\tau$
neutralinos	1/2	−1	$\tilde{B}^0\ \tilde{W}^0\ \tilde{H}_u^0\ \tilde{H}_d^0$	$\tilde{\chi}_1^0\ \tilde{\chi}_2^0\ \tilde{\chi}_3^0\ \tilde{\chi}_4^0$
charginos	1/2	−1	$\tilde{W}^\pm\ \tilde{H}_u^+\ \tilde{H}_d^-$	$\tilde{\chi}_1^\pm\ \tilde{\chi}_2^\pm$
gluino	1/2	−1	$\tilde{g}$	same
gravitino	1/2	−1	$\tilde{G}$	same

3.3 The Minimal Supergravity Model

In the case that supersymmetry is promoted from a global symmetry to a local gauge symmetry, then successive supersymmetry transformations can be shown to generate space-time translations [20, 21]. This allows the theory to make contact with General Relativity and hence include the gravitational interaction. The theory that emerges from this global-to-local symmetry promotion is known as *Supergravity*. As with any local gauge interaction, messenger particles must be introduced to communicate the force. In this case, it is a single spin-2 particle called the *graviton*, which has a spin-3/2 superpartner called the *gravitino*. These are both listed at the bottom of table 3-1. If supersymmetry were unbroken, then the gravitino would be exactly massless; however, the inclusion of soft SUSY breaking terms to the Lagrangian endows endows it with a non-zero mass. Depending on the exact mechanism of soft SUSY breaking, the gravitino can be as heavy as the other superpartners in the MSSM or significantly lighter, in which case it would be the LSP.

The 110 free parameters introduced by the most generic soft SUSY breaking mechanism leaves the MSSM rather impotent as a predictive model. However, a framework exists that reduces this vast parameter space to a much more tractable subspace. A large reduction can already be achieved by making rather modest assumptions about parameters which yield flavor-changing interactions. In this regard, strict experimental constraints can be used to eliminate several terms from the soft SUSY breaking component of the Lagrangian. These experimental measurements relate to mixings of the neutral K, D, and B meson systems respectively, as well as the decay rate of $\mu \rightarrow \gamma e$. By imposing these constraints, one finds that the subset of parameters is reduced to

- 3 gaugino masses M_1, M_2, M_3, which relate to the bino, wino, and gluino respectively.

- 5 squark and slepton mass-squared parameters $m_{\tilde{Q}}^2$, $m_{\tilde{L}}^2$, $m_{\tilde{u}}^2$, $m_{\tilde{d}}^2$, $m_{\tilde{e}}^2$, which relate to the left squarks, left sleptons, right up-type squarks, right down-type squarks, and right charged sleptons respectively.

- 3 trilinear couplings A_0^u, A_0^d, A_0^e which couple the left and right up-type squarks, the left and right down-type squarks, and the left and right charged sleptons to their respective Higgs fields. These parameters have dimensions of energy.

- 4 parameters from the Higgs potential $m_{H_u}^2$, $m_{H_d}^2$, $\tan(\beta)$, and $\text{sign}(\mu)$ which represent the mass-squared terms of the up- and down-type Higgs field, the ratio of the two Higgs VEVs ($\frac{v_u}{v_d}$), and the algebraic sign of the μ coefficient from Eq. 2–14

This reduction is referred to as the constrained MSSM (cMSSM) and leaves 15 parameters, which is much more manageable. Still, there are more simplifications that can be made. All of the mass-related parameters and couplings listed above scale with the energy transfer, so it is natural to impose some boundary conditions on them—at the Planck or GUT scale, for example. One such set of boundary conditions imposes the

following relationships:

$$M_1 = M_2 = M_3 \quad = \quad \mathbf{m}_{1/2} \tag{3–8}$$

$$m_{\tilde{Q}}^2 = m_{\tilde{L}}^2 = m_{\tilde{u}}^2 = m_{\tilde{d}}^2 = m_{\tilde{e}}^2 \quad = \quad m_{H_u}^2 = m_{H_d}^2 = \mathbf{m}_0 \tag{3–9}$$

$$A_0^u = A_0^d = A_0^e \quad = \quad \mathbf{A}_0 \tag{3–10}$$

In this scheme, the model is completely determined by 5 parameters $\{\mathbf{m}_{1/2}, \mathbf{m}_0, \mathbf{A}_0,$ $\tan(\beta), \text{sign}(\mu)\}$. From these boundary conditions, one can employ the so-called renormalization group equations (RGE) to determine how these 5 GUT-scale input parameters will yield the fifteen TeV-scale output parameters which are of particular interest to experimentalists searching for supersymmetry at modern-day colliders. The framework which imposes this set of boundary conditions is known as *minimal supergravity* or mSUGRA. While other boundary conditions exist, yielding other types of models, the mSUGRA scenario yields a rich, albeit constrained, parameter space which provides a diverse and manageable training ground for experimentalists to study the phenomenological consequences of supersymmetry.

In a supersymmetry scenario with mSUGRA-inspired boundary conditions, the mass parameters of the respective gauginos at TeV energy scales is to a good approximation described by

$$M_3 : M_2 : M_2 \approx 6 : 2 : 1. \tag{3–11}$$

Thus, the gluino is usually predicted to be a few times heavier than the neutralinos and charginos. This result can be mostly attributed to stronger effects of the QCD coupling when compared to the electroweak couplings at the TeV scale. For the same reason, squarks are generally expected to be heavier than sleptons. Owing to the interactions induced by the weak coupling, left superpartners are expected to be heavier than right superpartners [20]. This is pertinent to the first and second generations. The left and right gauge eigenstates of the third generation undergo a non-trivial amount of mixing.

In many scenarios, this leaves one of the two mass eigenstates to be lighter than those in the first and second generations, while leaving the other mass eigenstate significantly heavier. The lightest slepton is likely to be the $\tilde{\tau}_1$, while the lightest squark is expected to be either the $\tilde{t}_1$ or the $\tilde{b}_1$. The lightest of the 5 Higgs particles is expected to be the h^0 with a mass under roughly 150 GeV [20], and the other Higgs particles could be significantly heavier.

3.4   Hadron Collider Phenomenology of the mSUGRA Scenario

If supersymmetry exists in a form that is at least approximately described by mSUGRA, and the superpartners are below a few TeV, then there is a strong likelihood that several, if not many, of them will be exposed and discovered by the experiments operating at LHC. The following sections will discuss some of the general experimental signatures of supersymmetry in the hadron collider environment. This is meant to motivate the strategy adopted in Chapter 6 which describes one of the first searches for supersymmetry performed with high-energy collision data at the LHC. Some of the motivating factors are inspired by various assumptions made in the construction of the mSUGRA model, while others are quite model independent.

3.4.1   Strong Production

The LHC is a proton-proton collider, but the actual collisions do not involve the protons as whole, as they are composite particles. Rather, the collisions actually involve the constituent partons which comprise the protons. These are quarks and gluons. The proton is a bound state of two up-quarks and one down quark ($p = uud$). These are referred to as *valence quarks*. In the classical description of scattering, which involves two incoming particles and two outgoing particles, the valence quarks would be the only participants in a scattering process of two protons. However, in the quantum field description, the situation is much more complicated. The gluons which bind the valence quarks together can also serve as one or both of the incoming particles. There is a certain probability determined by the theory of QCD, that two colliding protons

will actually scatter gluons and not valence quarks. Even more bizarre is the notion

that non-valence quarks, i.e, the virtual quarks that emerge from the QCD analog of

Figure 2-1A, can also participate as initial states in the scattering process. This reality

leads to the concept of a *parton distribution function* or *pdf*. In other words, the total

momentum carried by the proton can be thought of as being distributed amongst a

mixture of valence quarks + virtual quarks + gluons. The amount of momentum (on

average) carried by each constituent is a very difficult quantity to calculate and is

energy-scale dependent. At energies of $\mathcal{O}(10 \text{ TeV})$, which are relevant for the LHC, the

gluon component is expected to dominate over the valence quarks. The contribution

from virtual quarks is the smallest, but still plays a significant role.

Because the LHC is a hadron collider, the initial states are guaranteed to involve

colored particles, i.e., particles that participate in the strong interactions governed by the

theory of QCD. This fact not only strongly influences the initial states but also the final

states. In the simplest and most likely case with two incoming particles and two outgoing

particles, the most dominant production mechanism of supersymmetric particle states

are shown by the Feynman diagrams in Figure 3-2. Not all of these diagrams contribute

equally to the production cross-section. Depending on the mass hierarchy of the gluino

with respect to the squarks, some diagrams will dominate over others. If one assumes

that the squark masses are roughly degenerate, then the following three scenarios

should be considered:

- $m_{\tilde{g}} > m_{\tilde{q}}$: In this case diagrams which include the production of two squarks, either via annihilation of the initial states into a gluon or by the exchange of a virtual squark, will dominate. These include 3-2C, 3-2J, and 3-2K. Diagram 3-2D produces two final-state squarks, but requires the exchange of a gluino which is taken to be heavy in this scenario. Processes involving the exchange of heavy particles are extremely suppressed.

- $m_{\tilde{g}} < m_{\tilde{q}}$: In this case diagrams which include the production of two gluinos, either via annihilation of the initial states into a gluon or by the exchange of a virtual gluino, will dominate. These include 3-2B, 3-2H, and 3-2J. Diagram 3-2A

yields two final-state gluinos but requires the exchange of a virtual squark, which is assumed to be heavy in this scenario and is therefore suppressed.

- $m_{\tilde{g}} \sim m_{\tilde{q}}$: In this case all diagrams in Figure 3-2 will have non-trivial contributions. Particularly, contributions from diagrams with a squark and a gluino in the final state will be enhanced, as in 3-2E and 3-2F.

| A $(q\bar{q} \to \tilde{g}\tilde{g})$ | B $(q\bar{q} \to \tilde{g}\tilde{g})$ | C $(q\bar{q} \to \tilde{q}\tilde{q}^*)$ | D $(qq \to \tilde{q}\tilde{q})$ |

E $(qg \to \tilde{q}\tilde{g})$ F $(qg \to \tilde{q}\tilde{g})$ G $(qg \to \tilde{q}\tilde{g})$

H $(gg \to \tilde{g}\tilde{g})$ I $(gg \to \tilde{g}\tilde{g})$ J $(gg \to \tilde{q}\tilde{q}^*)$ K $(gg \to \tilde{q}\tilde{q}^*)$
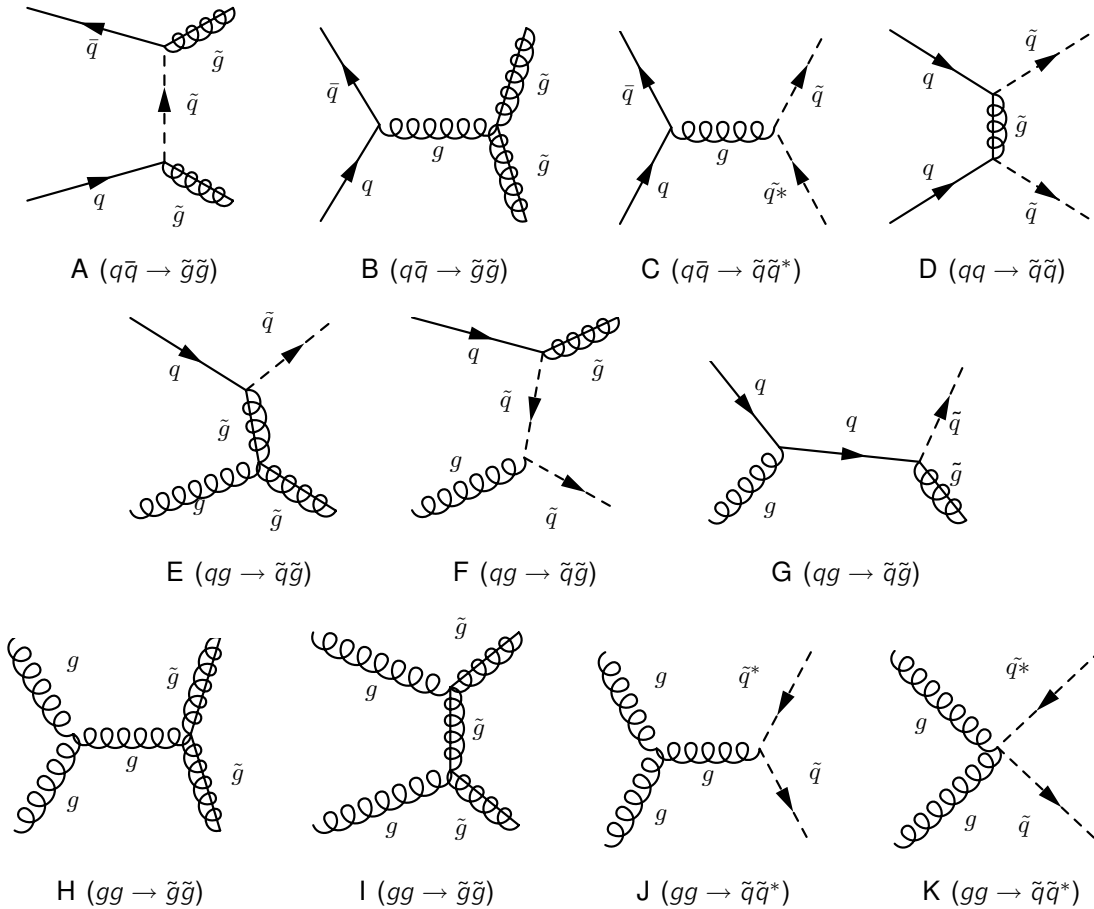
Figure 3-2. A sample of strong production mechanisms of squarks and gluinos

The conclusions drawn above are valid if one assumes that in either scenario, the masses are within the range accessible by the collider. In the case that the squarks and gluinos are too heavy to be produced, then the greater strength of the strong QCD coupling will be irrelevant, and the incoming partons will be forced to directly produce lighter superpartners via the electroweak interaction. This will involve diagrams like the ones in Figure 3-3, which directly yield neutralinos and charginos. The role of these

diagrams may be negligible or significant depending on the mass spectrum of the colored superpartners.
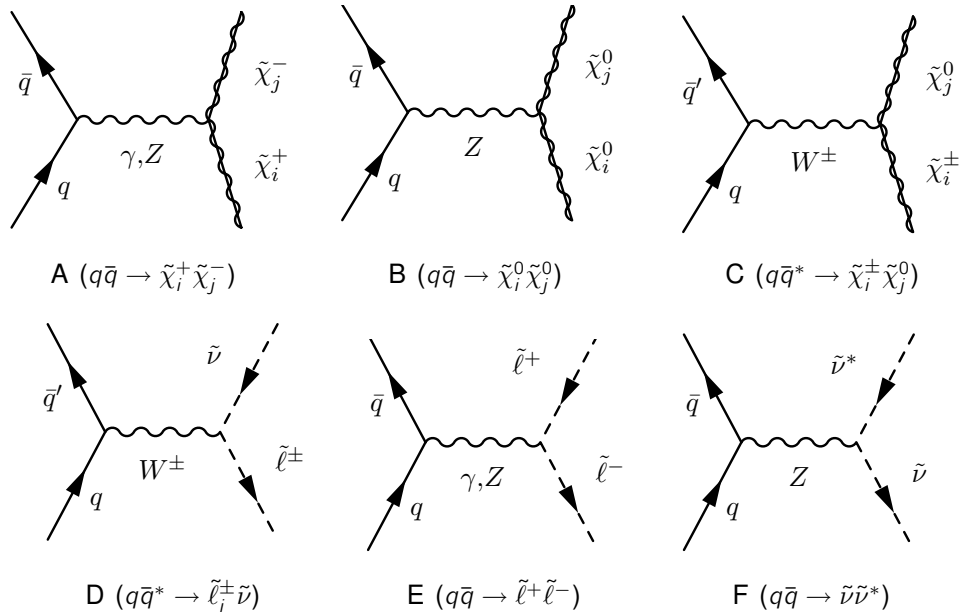
Figure 3-3. A sample of electroweak production mechanisms of charginos, neutralinos, and sleptons

From a phenomenological perspective the differences between strong and electroweak SUSY production are significant. Unlike the latter, the former involves heavy colored particles, which must decay to Standard Model colored particles (i.e., quarks). Each quark will hadronize and become a jet. Furthermore, the multiplicity of jets produced in the event will be largely dependent on whether or not gluinos or produced. If a gluino is produced, it will decay to a quark and squark (i.e., $\tilde{g} \rightarrow q\tilde{q}^*$). The squark, which will likely be off-shell, will also decay to a quark and gaugino (i.e., $\tilde{q} \rightarrow q\chi$). This is illustrated by the diagram in Figure 3-4. In the case that squarks are lighter than gluinos, then the production and subsequent cascade decay will begin with the squark in Figure 3-4 and will only yield one jet before decaying to a gaugino. Because superpartners must be produced in pairs (in R-parity conserving scenarios), the following will in general be true:

- $\tilde{g}\tilde{g}$ production will lead to at least $2 + 2 = 4$ hadronic jets.

- $\tilde{g}\tilde{q}$ production will lead to at least $2 + 1 = 3$ hadronic jets.

- $\tilde{q}\tilde{q}$ production will lead to at least $1 + 1 = 2$ hadronic jets.

In reality there may be more jets that arise either from final state gluon radiation (FSR) of the outgoing partons or initial state gluon radiation (ISR) of the incoming partons. Thus, in the hadron collider environment searches for SUSY typically rely on the signature of multiple high-energy jets. In order to characterize the total amount of hadronic jet activity in a collision event independent of the jet multiplicity, it is common to construct a variable that sums the scalar transverse momenta of all of the jets. Typically, this variable is denoted as H_T, and can provide a useful discriminant between events that feature colored production and those that do not.
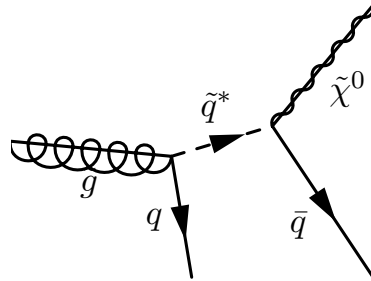
Figure 3-4. Diagram of gluino and squark decay

3.4.2 Missing Energy

One of the most important consequences of mSUGRA-inspired models is that they provide a viable dark-matter candidate which is referred to as the LSP. In most cases the LSP is the lightest neutralino (χ_1^0), which is an electromagnetically neutral and weakly interacting particle. As was discussed in Sec. 3.2.2, if R-Parity is a perfectly conserved quantum number, then every collision event which produces superpartners (in pairs) will inevitably yield cascade decays that end in the production of a pair of LSPs. These LSPs act like massive neutrinos and will be invisible to a detector.

Despite the fact that LSPs cannot interact directly with the detector and be measured, their presence can be inferred indirectly by the resulting momentum imbalance that they leave. In the case that two incoming partons with momenta denoted $\vec{p}_1^{\,i}$, $\vec{p}_2^{\,i}$ collide inelastically and produce two superpartners, which subsequently undergo cascade decays to n final state objects such as jets, leptons, photons, and two LSPs with momenta denoted $\vec{p}_1^{\,f}$, ..., $\vec{p}_n^{\,f}$, then the conservation of momentum yields Eqs. 3–12, 3–13 and 3–14.

$$p_{x,1}^i + p_{x,2}^i = \sum_{m=1}^{n} p_{x,m}^f \tag{3–12}$$

$$p_{y,1}^i + p_{y,2}^i = \sum_{m=1}^{n} p_{y,m}^f \tag{3–13}$$

$$p_{z,1}^i + p_{z,2}^i = \sum_{m=1}^{n} p_{z,m}^f \tag{3–14}$$

The $x-$ and $y-$components of the initial partons are equal to zero for a collider, as the beams are traveling exclusively in the z direction. Thus, the total initial and final momentum transverse to the beam direction is zero. Consequently, Eqs. 3–12 and 3–13 can be combined and rewritten as shown in Eq. 3–15.

$$\vec{p}_{T,1}^{\,i} + \vec{p}_{T,2}^{\,i} = 0 = \sum_{m=1}^{n} \vec{p}_{T,m}^{\,f} \tag{3–15}$$

If one assumes that $n-2$ final state particles are visible to the detector and are well-measured, then a constraint can be made on the total transverse momentum of the two LSPs which escape undetected. Without loss of generality, the two LSPs can be denoted by the indices n and $n-1$ respectively. This constraint yields an important quantity used for SUSY searches known as the *missing transverse momentum*, denoted symbolically as $\vec{\not{p}}_T$. In this particular example, the $\vec{\not{p}}_T$ would be calculated as

$$\vec{\not{p}}_T = \vec{p}_{T,n-1}^{\,f} + \vec{p}_{T,n}^{\,f} = -\sum_{m=1}^{n-2} \vec{p}_{T,m}^{\,f}. \tag{3–16}$$

In the case that all of the final state objects are visible and well-measured, then $\not{p}_T \approx 0$ (i.e, a non-SUSY event)[3] . The only particles from the Standard Model that can be produced in colliders and contribute to a non-zero $\not{p}_T$ are neutrinos, in which case $\not{p}_T > 0$. Thus, the missing momentum signature is not exclusive to SUSY and background from the Standard Model does exist, and this will be discussed in more detail later in Chapter 6.

For historical reasons the missing transverse momentum is often confusingly referred to as the *missing transverse energy*. This is likely due to the fact that the visible final state objects are usually detected by calorimeters, which measure energies of particles (see Sections 5.2.3 and 5.2.4). In the limit that the final state objects are relativistic (which is always the case at the LHC), the masses can usually be ignored when discussing kinematical properties as the Einstein energy-momentum equation reduces to Eq. 3–17.

$$\lim_{p \gg m} E = \lim_{p \gg m} \sqrt{p^2 + m^2} = p \tag{3–17}$$

Thus, the momentum measurements implied in Eqs. 3–12, 3–13, and 3–14 are replaced by energy measurements in practice, and $\not{p}_T$ is replaced by $\not{E}_T$, even though they both represent the same observable. From here on the latter will be used to conform to the convention used most often in the literature.

The total initial momentum in the z direction (along the beams) is unknown at hadron colliders, and will be different for each collision, owing to the *pdf*'s described in Section 3.4.1. At the instant of the collision, the colliding parton could be carrying any fraction of the proton's total momentum, in principle. Thus, while the relationship in Eq. 3–14 is true, the initial conditions are unknown, and consequently no obvious constraints can be placed on the final state objects. For this reason, transverse event

---

[3] For convenience the magnitude of $\vec{\not{p}}_T$ will be denoted by $\not{p}_T$.

variables are often employed at hadron colliders. The missing transverse energy is one such, very important, observable.

3.4.3 Same-Sign Lepton Pairs

While events featuring SUSY production will most likely begin with colored particles (squarks or gluons) and always end with LSPs (assuming R-Parity conservation), numerous possibilities exist for what happens in between. Clearly, a gluino must always decay to a quark-squark pair (off-shell if necessary). The handedness of the quark will influence the decay of the squark. The strong force does not prefer a particular configuration, so 50% of the time the quark (squark) will be right-handed (left), assuming it is the product of a gluino decay. The left-squark couples to winos, binos, and higgsinos, while the right-squark only couples to higgsinos and binos. Given that the charginos and neutralinos constitute model-dependent superpositions of wino, bino, and higgsino eigenstates, it is not predetermined which decay channels will be accessible to left- and right-squarks, respectively; however, some loose generalizations can be made. In mSUGRA models the LSP is predominantly a bino eigenstate, with little contribution from the wino and higgsino eigenstates. The charginos and heavier neutralinos tend to have a smaller bino component. Thus, if right-squarks are produced, either directly or through gluino decay, they will decay to their quark superpartner and immediately to the LSP. This phenomenon would constitute a *jets and missing energy* signature. In the case that the left-squark is produced, intermediate decays to charginos and heavier neutralinos are accessible in order to end with an LSP. These intermediate decays will inevitably yield Standard Model leptons, which would constitute a *leptons, jets, and missing energy* signature.

The production of leptons is a key signature at hadron colliders for two reasons: 1) they indicate that an electroweak process occurred, which is not favored by interactions that begin with colored particles (i.e., strong interactions are favored) and 2) leptons are typically easier to unambiguously detect, and their final-state attributes can be

well-measured. Once one decides to focus on leptonic signatures of SUSY production, a natural question arises. How can SUSY produce leptons in a configuration that is not easily producible by interactions involving particles exclusive to the Standard Model? A strikingly unique configuration relates to the production of a pair of leptons (di-leptons) with each lepton carrying the same electromagnetic charge [20, 23–27]. An example of such an event is shown in Figure 3-5. This process involves the production of a gluino and left-squark, which each give rise to a cascade decay of Standard Model particles. The three quarks ($\bar{q}$, q', q'') will each be detected as jets. The two leptons ($\ell^+\ell^+$) can be from the same family or from different families and will have the same electromagnetic charge. These will be detected in isolation from other objects in the decay[4]. The neutrinos ($\nu\nu$) as well as the LSPs ($\tilde{\chi}_1^0\tilde{\chi}_1^0$) will contribute to a significant amount of missing energy. Figure 3-5 is one simple example of a SUSY event which yields same-sign di-leptons. There are many more configurations which result in a similar event signature or topology.
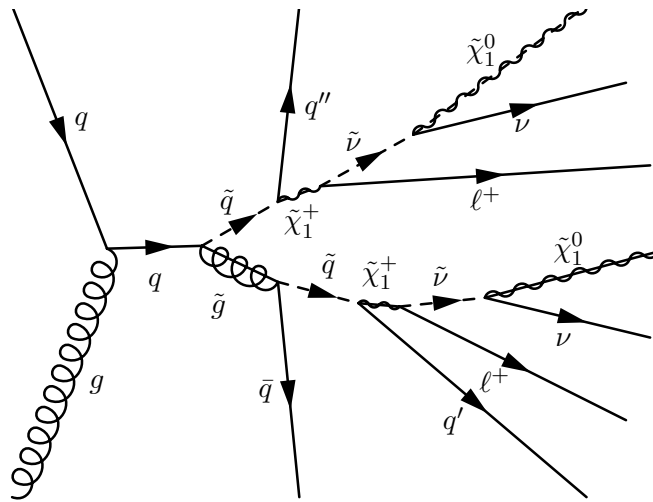
Figure 3-5. Example of same-sign di-lepton production in supersymmetry

---

[4] Determining whether or not a lepton is isolated is a crucial aspect of event reconstruction and is thus the focus of a great amount of work by experimentalists. This will be discussed in greater detail in Chapter 6

As will be shown later in Chapter 6, the production of same-sign di-leptons is greatly suppressed in the Standard Model, thus making the *same-sign di-leptons, jets, and missing energy* signature one of the most promising avenues for detecting supersymmetry. While this work focuses on this signature in the context of R-Parity conserving models of supersymmetry, same-sign di-leptons can also be featured in a variety of alternative theories of new physics beyond the Standard Model, such as Universal Extra-Dimensions [28], heavy Majorana neutrinos [29], and grand unified theory in warped dimensions [30].

3.5   Current Experimental Limits on Supersymmetry

While the parameter space for the MSSM is vast, not all possible values of the parameters are viable. As was discussed in Sec. 3.3, strong theoretical motivation and compelling experimental evidence justify many of the simplifying assumptions that were used to formulate the mSUGRA model, which is fully defined with the specification of 5 parameters ($\mathbf{m}_{1/2}$, $\mathbf{m}_0$, $\mathbf{A}_0$, $\tan(\beta)$, $\text{sign}(\mu)$). Further reduction of the parameter space has indeed been achieved by a variety of experimental results from the past few decades. A thorough review of the constraints on supersymmetry is provided in Ref. [11]. A brief summary of these will be given in the following sections, with a focus on models which conserve R-Parity and feature gaugino and scalar mass unification at the GUT scale (e.g., mSUGRA).

3.5.1   Constraints from Astrophysical Evidence of Dark Matter

Analysis of the Cosmic Microwave Background (CMB) data from the Wilkinson Microwave Anisotropy Probe (WMAP) shows that the density of baryonic matter in the universe is $\Omega_b h^2 = 0.0227 \pm 0.0006$, while the total density of matter in the universe is $\Omega_m h^2 = 0.133 \pm 0.006$ [11], where h is the Hubble constant that characterizes the expansion of the universe. The matter density excess, i.e. $\Omega_{DM} h^2 = (\Omega_m - \Omega_b) h^2 = 0.110 \pm 0.006$ is generally attributed to a cold dark matter substance. Constraints can thus be placed on the parameter space such that the relic abundance of the

LSP accounts for the observed dark matter, i.e., $\Omega_\chi \approx \Omega_{DM}$. The interplay of the mSUGRA parameters and Ω_χ is quite involved but some generalizations can be made. The cross-section for two thermal LSPs to annihilate (e.g., $\chi_1^0 \chi_1^0 \to f\bar{f}$) depends on the couplings and masses of the exchanged and final-state particles, and is inversely proportional to the LSP relic density Ω_χ [31]. Typically, the annihilation will involve the exchange of a Z boson, a Higgs boson, or a sfermion and will result in a fermion-antifermion pair. More final states become available as the mass of the LSP increases (e.g, pair production of Z and W bosons or top quarks). Each point in the mSUGRA parameter space yields a distinct value for Ω_χ. While there is some dependence on the values of other parameters, in order to get Ω_χ in the right neighborhood, the values of $\mathbf{m}_0$ and $\mathbf{m}_{1/2}$ are restricted to very narrow ranges. A detailed review and analysis of the viable regions can be found elsewhere [32].

3.5.2 Constraints from Indirect Low-Energy Measurements

Evidence of the existence of superpartners could be observed indirectly through loop contributions to various observables. One such example is the decay of the B-meson to a pair of oppositely charged leptons. Such decays are only possible in the Standard Model through second-order weak interactions, and are thus heavily suppressed. However, the quantum corrections that would come from the presence of superpartners could result in a detectable enhancement in the respective branching ratios for the $B_s^0 \to \mu^+\mu^-$ and $B_s^0 \to e^+e^-$ (or likewise for B^0). Precise measurements of these branching ratios were carried out at the CDF and D0 experiments at the Tevatron collider and also at various B-factory experiments [11]. While none of the experiments had the sensitivity to confirm the Standard Model prediction, strict lower limits on the branching ratios of $\mathcal{O}(10^{-8})$ were placed, and a portion of the previously allowed SUSY parameter space was excluded as a result.

Another measurement which has the potential to make contact with virtual SUSY particles via loop corrections is that of the muon magnetic moment (a_μ). This quantity

can be calculated to very high precision in the Standard Model. It can likewise be measured to very high precision by studying the precession of muons as they circulate around a storage ring under a constant magnetic field. The E821 experiment at Brookhaven National Laboratory (BNL) recently published an interesting result which suggests a 3.2σ discrepancy between the predicted and observed value of a_μ [33]. While this is not conclusive, it does accommodate a variety of SUSY models which predict an additional contribution to a_μ. Superpartners with masses in the range of $100 - 500$ GeV could potentially account for the deviation. The correction is also proportional to $\tan(\beta)$ [11].

3.5.3 Constraints from Direct Experimental Searches

The most powerful limits set by direct searches for supersymmetric particles were achieved by the experiments of the LEP (Large Electron Position) collider and the Tevatron $p\bar{p}$ collider, respectively. At LEP, where the center of mass energy was $\sqrt{s} = 209$ GeV, the dominant production mechanism occurs by electroweak processes. Table 3-3 summarizes the limits set for various species of sparticles. For sleptons the parameters of μ and $\tan(\beta)$ are set to -200 GeV and 1.5 respectively. Chargino masses are sensitive to M_2, μ, and $\tan(\beta)$. The limits on the lightest chargino are presented in 3-3 and are robust against a scan over these parameters, except for large values of M_2 ($\gtrsim 1$ TeV) where the mass difference between $\chi_1^\pm$ and χ_1^0 is very small [11]. Neutralino masses are sensitive to M_1 in addition to the parameters relevant for the charginos. In many models the lightest neutralino is electrically neutral, which implies direct searches are not really feasible. However, indirect limits can be placed on the mass of the LSP based on slepton, chargino, and Higgs searches. Many limits listed in Table 3-3 rely on the assumption of sfermion and gaugino mass unification at the GUT scale. In many cases, the limits can be tightened if further assumptions are made about model parameters. The results for $\tilde{\tau}_{L,R}$ and $\tilde{t}_1$ assume the worst case scenario for L-R mixing.

Table 3-3. Limits on SUSY particles from the LEP experiments (ALEPH, OPAL, DELPHI, L3) [11]

Particle	Mass Limit (GeV)	Comment
$\tilde{e}_{L,R}$	$\gtrsim 100$	Limit valid for $M_{\tilde{\chi}_1^0} < 85$ GeV
$\tilde{\mu}_{L,R}$	$\gtrsim 95$	Limit valid for $\Delta M(\tilde{\mu}_R, \tilde{\chi}_1^0) > 5$ GeV
$\tilde{\tau}_{L,R}$	$\gtrsim 86$	Limit valid for $\Delta M(\tilde{\tau}_R, \tilde{\chi}_1^0) > 7$ GeV
$\tilde{\chi}_1^\pm$	$\gtrsim 103$	Limit valid for $M_{\tilde{\nu}} > 200$ GeV
$\tilde{\chi}_1^0$	$\gtrsim 47$	Limit valid for a wide range of $\tan(\beta)$
$\tilde{t}_1$	$\gtrsim 96$	Limit valid for $\Delta M(\tilde{t}_1, \Delta M(\tilde{\chi}_1^0, c)) > 5$ GeV)

At the Tevatron collider, where the center-of-mass energy is $\sqrt{s} = 1.96$ TeV, production of colored particles is expected to dominate because the initial particles are colored. Table 3-4 summarizes the limits that were achieved by the CDF and D∅ experiments at the Tevatron. Most limits are presented for an mSUGRA scenario where $\tan(\beta) = 3$, $A_0 = 0$, and $\mu < 0$, but were also found to be valid for a wide range of parameter values. Searches involving associated chargino-neutralino production (e.g. $qq' \to \tilde{\chi}_1^\pm \tilde{\chi}_2^0$ through s-channel $W^\pm$ exchange) were also performed. These searches exploited the same-sign di-lepton signature in order to reduce backgrounds and set exclusion limits [34, 35].

Table 3-4. Limits on SUSY particles from the Tevatron experiments (CDF, D∅) [11]

Particle	Mass Limit (GeV)	Comment
$\tilde{q}_{L,R}$	$\gtrsim 379$	Limit valid for first and second generation squarks over a large scan of the parameter space
$\tilde{t}_1$	$\gtrsim 180$	Limit valid for $40 \lesssim M_{\chi_1^0} \lesssim 95$ GeV
$\tilde{b}_1$	$\gtrsim 240$	Limit valid for $M_{\chi_1^0} < 80$ GeV
$\tilde{g}$	$\gtrsim 308$	Limit valid for a large scan of the parameter space
$\tilde{\chi}_1^\pm$	$\gtrsim 164$	Limit valid for $\mathbf{m}_0 = 60$ GeV, $\mu > 0$

In order to compare the sensitivities of various searches across different experiments, a convention has been established to present search limits as exclusion contours in the $\mathbf{m}_0$ - $\mathbf{m}_{1/2}$ plane of the mSUGRA parameter space. A choice of $\tan(\beta) = 3$, $A_0 = 0$, and

$\mu < 0$ was made rather arbitrarily. Figure 3-6 shows the excluded region (red shading) from a DØ search for squarks and gluinos [36] along with the limits set by the direct chargino searches from the LEP experiments (blue and gray shading). The solid red line delimits the excluded region set by the analysis and the dashed blue line reveals the expected exclusion limit. The dotted black lines enclosing the exclusion limit represent the theoretical uncertainties.
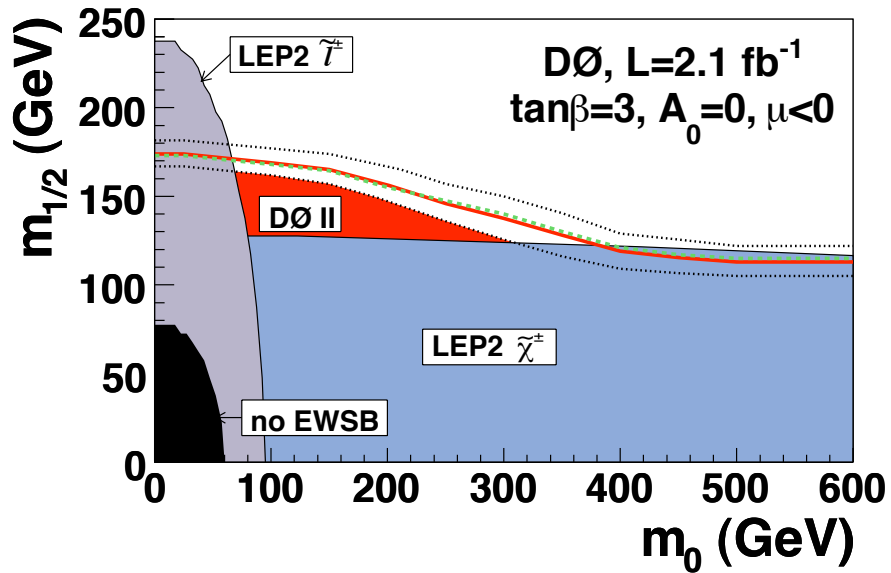
Figure 3-6. Exclusion limits for squarks and gluinos from the DØ experiment presented on the $m_0 - m_{1/2}$ plane for $\tan(\beta) = 3$, $A_0 = 0$, and $\mu < 0$ [36].

The experiments operating at the LHC are expected to extend the exclusion limits well beyond those in Figure 3-6 in the worst case scenario, or confirm the existence of supersymmetry in the best case scenario. For the latter case, the naturally low rate of Standard Model backgrounds to the same-sign di-lepton signature may enable it to provide the most compelling evidence. This will be discussed in more detail in Chapter 6.

CHAPTER 4
THE LARGE HADRON COLLIDER

4.1 Design

The LHC is a superconducting hadron accelerator consisting of two rings (one for each beam). The tunnel which hosts the LHC spans 26.7 km in circumference and straddles the Franco-Swiss border in the region near Lake Geneva and the Jura Mountains. Construction of the tunnel began on behalf of the Large Electron Position (LEP) collider at CERN in 1984 and was completed in 1989. LEP preceded the LHC, operating from 1991 to 2000. In fact, the LHC project was approved in 1994 by the CERN council while LEP was still in the early stages of fulfilling its potential.

Budget concerns required the LHC to exploit the existing LEP tunnel. This constraint came with implications, as the geometry of the preexisting tunnel (i.e., the proportions of straight and curved sections) is actually best suited for circulating electrons and positrons, which experience significant energy losses due to synchrotron radiation while under the influence of magnetic fields. Protons, for example, do not suffer such dramatic losses and could take better advantage of a more circular ring [37]. The tunnel geometry combined with the existing superconducting magnet technologies ultimately imposed an upper bound on the center-of-mass energies achievable by the LHC at $\sqrt{s} = 14$ TeV. This limit would still be roughly 7 times higher than the energies achieved by the world's most powerful accelerator at the time, the Tevatron of Fermilab.

One of the most important advantages that the LHC has over its predecessors is not only the collision energy, but also the instantaneous luminosity, which determines the rate at which high-energy collision events will be produced. The simple formula for the event rate is given in Eq. 4–1.

$$n_{events} = L \cdot \sigma(pp \rightarrow X) \tag{4–1}$$

where L is the instantaneous luminosity and the cross-section $\sigma(pp \to X)$ is determined by the Lagrangian governing the dynamics of X and does not depend on the beam parameters, aside from the value of $\sqrt{s}$. It is clear that if X is rare (i.e., has small cross-section), then the importance of attaining high instantaneous luminosity is paramount. The common expression for the instantaneous luminosity for a Gaussian beam distribution is given by [37]:

$$L = \frac{N_b^2 n_b f_{rev} \gamma}{4\pi \epsilon_n \beta^*} \cdot \frac{1}{\sqrt{1 + (\frac{\theta_c \sigma_z}{2\sigma^*})^2}}. \tag{4–2}$$

A description of some of these and other beam related parameters as well as their nominal and commissioned values is given in Table 4-1. It is worth noting that the instantaneous luminosity achieved by the LHC if these parameters take on their nominal values is $L_{peak} = 10^{34} cm^{-2} s^{-1}$, which is nearly a factor of seventy greater than that obtained by the Tevatron. It was partially this high-luminosity ambition that motivated the choice of dual proton beams for the LHC instead of proton-antiproton beams, as is the case for the Tevatron. Production, capture, and circulation of antimatter always presents a greater challenge for experimentalists than working with ordinary, stable matter particles like protons and electrons. However, circulating particle-antiparticle beams does provide the added advantage of only needing a single ring. The two beams can share the same magnetic field and hence the same phase space while in orbit.

It should be noted that the LHC also circulates heavy ion beams (Pb) during various stages of operation. Details concerning the heavy ion physics program are beyond the scope of this work, but can be found elsewhere [37].

The LHC tunnel lies underground at depths varying from 50 m to 175 m (under the Jura Mountains) and hosts several experiments, which will be summarized in Sec. 4.2. A schematic layout of the CERN accelerator complex can be found in Figure 4-1. As one can readily observe, there is a sequence of smaller accelerators which are used to feed proton beams into the LHC, with each successive one imparting more energy than

Table 4-1. Summary of LHC beam parameters

Parameter	Description	Units	Nominal Value	Commissioned Value (2010)
N_b	protons per bunch		1.15×10^{11}	1.15×10^{11}
n_b	bunches per beam		2808	368
T_{bs}	bunch spacing	ns	25	150
f_{rev}	orbit frequency	kHz	11.245	11.245
γ	relativistic boost		7461	3730
ϵ_n	transverse emittance		3.75	2.1
β^*	beta function at IP	m	0.55	3.5
θ_c	crossing angle	μrad	285	200
σ_z	RMS bunch length in z-direction	cm	7.55	9
L_{peak}	peak instantaneous luminosity	$cm^{-2}s^{-1}$	10^{34}	2.05×10^{32}
$\sqrt{s}$	c.o.m. energy	TeV	14	7

the prior. Protons are harvested from di-hydrogen atoms. Once isolated, the harvested

protons are injected into the PS Booster (PSB) with energies near 50 MeV (via the

Linac2). The PSB accelerates the protons until they achieve an energy of 1.4 GeV

(roughly half the speed of light) whereby they are fed to the Proton Synchrotron (PS)

until they are accelerated to 25 GeV (approximately 98% the speed of light). From the

PS they are sent to the Super Proton Synchrotron (SPS) which is their last destination

before being injected into the LHC at 450 GeV. This transition from 50 MeV to 450

GeV takes just under 5 minutes under normal circumstances. The design of the LHC

projected a 20 minute period for the RF cavities in the LHC to take the protons from

450 GeV to 7 TeV; however, owing to unexpected difficulties encountered during the

commissioning stages of the LHC in 2008-2009, this nominal design energy has not yet

proven to be feasible. Instead, the terminal energy for the protons thus far achieved is

3.5 TeV. This yields a collision energy of $\sqrt{s} = 7$ TeV, which proved to be the state of

operation for the 2010 LHC runs from which this work is based. More details on the LHC

operation in 2009-2010 will be discussed in Sec. 4.3

It is important to note that protons do not arrive to the LHC individually. Rather,

they are synchronized and arrive in what are called "bunches". From Table 4-1 it is clear

that bunches comprise up to 115 billion protons under nominal conditions. Bunches

Figure 4-1. CERN's accelerator complex

can be separated in space by as little as $\sim$ 7 m and separated in time by as little as 25 ns. Steering of the proton bunches is performed in the arcs of the LHC by $1,232$ powerful superconducting dipole magnets. For 7 TeV beams circulating the 27 km ring, a magnetic field of 8.33 Tesla is required. The strength of the required magnetic field scales linearly with the energy of the beams. Thus, the energy limit is strongly coupled to the magnet technology. Focusing of the beams in the transverse plane is performed by a lattice formation of 392 quadrupole magnets which are located in various sectors around the ring. There are many other types of magnet systems employed throughout the LHC (e.g. sextupoles, octupoles) which also help to control the beams.

It is crucial that the LHC beam pipes hosting the proton beams are completely evacuated. Any residual gas particles may cause elastic or inelastic collisions with the circulating protons. Not only does this affect the lifetime of the beam, but such collisions create a so-called "machine-induced background" for the experiments if they happen to occur upstream or downstream of the respective detectors. The main vacuum system is engineered to reduce the pressure of the LHC beam pipes to a level of 10^{-13} atm .

4.2 Experiments

The collisions produced by the LHC are studied by six distinct particle detectors. A brief summary of each experiment is described below:

- **CMS**
  The Compact Muon Solenoid (CMS) is a general purpose particle detector which is designed to operate at high luminosity (L=10^{34}cm^{-2}s^{-1}). Its main feature is 3.8 Tesla superconducting, solenoidal magnet which aids in the identification of various charged particle species. The physics program of the CMS detector is diverse, covering precision Standard Model measurements as well as offering an excellent sensitivity to various scenarios for the Higgs mass and models of new physics, like supersymmetry. Over 3,000 scientists from nearly 200 institutes across the world collaborate on the CMS experiment. It is a vast scientific endeavor. More details on the CMS detector will be discussed in Chapter 5 and can also be found elsewhere [38]. This results shown in Chapter 6 are based on data recorded by the CMS experiment.

- **ATLAS**

A Toroidal Lhc ApparatuS (ATLAS) is also a general purpose particle detector which is designed to operate at high luminosities. ATLAS and CMS are competing experiments and have similar particle detection attributes, but have completely different designs with respect to the magnetic field employed, and the materials used to build the tracking detectors and calorimeters. One may wonder why valuable resources (e.g., manpower and money) is devoted to building two separate machines which are meant to perform the same tasks. It is important that any potential discovery or signal exclusion results reported by one experiment can be corroborated by another. These dueling experiments serve this exact purpose. This provides consistency and redundancy to any ground-breaking discoveries which may be waiting for us at the LHC. The ATLAS collaboration is similar in size to the CMS collaboration. More details on the ATLAS experiment can be found elsewhere [39].

- **ALICE**
  A Large Ion Collider Experiment (ALICE) will study the heavy-ion collisions produced by the LHC. These collisions are expected to produce an exotic state of matter, the so-called quark-gluon plasma, which is theorized to have existed during the initial stages after the Big Bang. Among other things the studies of quark-gluon plasma may shed light on properties of confinement in the theory of strong interactions (QCD). The luminosity which is delivered to ALICE by the LHC is significantly less than that which will be delivered to the high luminosity experiments. ALICE will receive L$\sim 10^{27}$cm^{-2}s^{-1} [37]. The complete technical design report for the ALICE experiment can be found elsewhere [40].

- **LHCb**
  The Large Hadron Collider beauty (LHCb) experiment will study the physics of b-quarks in an attempt to understand why the universe is composed predominantly of matter with very little anti-matter. The LHCb design is peculiar in that it is asymmetric with respect to the transverse plane. It consists of only one forward spectrometer which will catch the debris of proton-proton collisions along the beam line in only one direction. Because such little energy is needed to produce b-quarks in such collisions, they are produced with significant momentum in the z-direction (along the beams) and therefore travel very near to the beam line. Thus, only a small solid angle of coverage is necessary to capture the full decay of any B-mesons one wishes to study. By design the LHCb experiment expects luminosities which are about two orders of magnitude less than CMS and ATLAS [37]. More details of the LHCb experiment can be found elsewhere [41].

- **LHCf**
  The Large Hadron Collider forward experiment (LHCf) consists of two detectors of relatively small size located ± 140 m from IP1 (i.e., the ATLAS interaction point) and will study very forward neutral particles emerging from proton-proton collisions occurring at IP1. The main physics goal is to validate and calibrate the hadron interaction models which are used in the study of very energetic cosmic-rays.

The LHCf collaboration is much smaller in size than the other LHC experiments, consisting of roughly 20 scientists from about 10 institutions. The details of the LHCf project can be found elsewhere [42].

- **TOTEM**
  The TOTal Elastic and diffraction cross-section Measurement (TOTEM) experiment will also study the forward debris of proton collisions in the regions surrounding IP5 (i.e., the CMS interaction point). Among other goals, the TOTEM experiment will measure the size of protons and provide an accurate measurement of the LHC's luminosity. More details about the physics program of TOTEM can be found elsewhere [43].

4.3   Performance in 2009-2010 and Projections for 2011-2012

The Large Hadron Collider, like many accelerators before it, serves as its own prototype. As a consequence many lessons had to be learned during the design and commissioning stages. Many unforeseen obstacles were encountered and the LHC suffered various setbacks which ultimately delayed the initial start-up of proton-proton collisions by several years. After much anticipation, the LHC began to circulate a single non-colliding proton beam at injection energies (450 GeV) on September 10, 2008. This was a monumental achievement and marked the beginning of what was thought to be the LHC-era of new physics discoveries. This excitement was short-lived as only nine days later on September 19 a devastating engineering flaw was exposed while ramping up a section of dipole magnets to currents high enough to steer 5.5 TeV beams. In short, a faulty electrical connection caused an electrical arc that punctured the helium vessel, which subsequently released several tons of liquid helium into the tunnel. The huge pressure forces associated with this release caused severe structural damage to magnet system and the ring in the surrounding area [44].

The LHC would suffer a year long delay to not only repair the damage, but to also thoroughly test and improve the electrical connections throughout the rest of the accelerator so that this incident would not be repeated. It was determined that when the LHC starts up again, it would operate for an extended period with a reduced beam

energy of 3.5 TeV (instead of 7 TeV) in order to give the LHC operators experience with running the machine safely [45].

In late 2009 after several months of repairs and hardware commissioning, the LHC began to inject proton beams into the rings again, starting with injection energies and gradually working up to higher magnetic fields to steer higher energy beams. On November 30, 2009 history was made as the LHC replaced FermiLab's Tevatron as the highest energy particle accelerator in the world by circulating protons at an energy of 1.18 TeV (beating the previous record of 0.98 TeV) [46]. Shortly after, the LHC began to steer the beams into each other at the interaction points along the ring, and the particle detectors were observing collisions at a record c.o.m. energy of 2.36 TeV. Following a brief shutdown period, on March 19, 2010 the LHC began circulating proton beams at the record energy of 3.5 TeV and on March 30 began colliding them. The LHC physics program was now underway.

The intention was to carefully increase the instantaneous luminosity over a period of several months. Gradually, the number of protons per bunch would increase and the number of bunches injected per beam would increase. Other parameters related to the beam optics would begin to approach their nominal values as well. From April to early June of 2010, only a few bunches were injected per fill. Starting in late June through the end of July, the LHC increased the number of bunches injected to 13. Then in August, it was up to 25 to 50 bunches. In the period from mid-September to late October, fills would contain anywhere from 50 to 368 bunches, in some cases with bunch spacings of 150 ns. The final proton-proton fill for 2010 came on November 4, 2010. In the subsequent weeks the LHC transitioned to a brief lead-ion run.

Figure 4-2 shows the instantaneous luminosity integrated over time (also called the integrated luminosity) delivered by the LHC (red) and recorded by the CMS detector (blue) as a function of time. The integrated luminosity $\int L \, dt$ has units of inverse length-squared and is a useful measure of how much data is produced or collected.

68

For a process of interest with a known cross-section σ, one simply has to take the product of $\int L \, dt \cdot \sigma$ to determine the expected number of events produced in the collected data. This is simply the time-integral of Eqn. 4–1. In 2010 the LHC delivered roughly 47 pb^{-1} of data to the CMS experiment, meaning a process with $\sigma = 1$ pb could be expected to be produced 47 times on average in a data set of this size. Figure 4-2 also demonstrates the efficient operations of the CMS experiment as there was little dead time while the LHC was producing good collision data. Perhaps, the most important observation is the exponential rise in data produced as the LHC was gradually increasing the instantaneous luminosity. Despite constant operation of the LHC in the period spanning April to November, nearly half of all of the data was produced in the last week of running. This highlights the importance of running the accelerator at the nominal instantaneous luminosity.
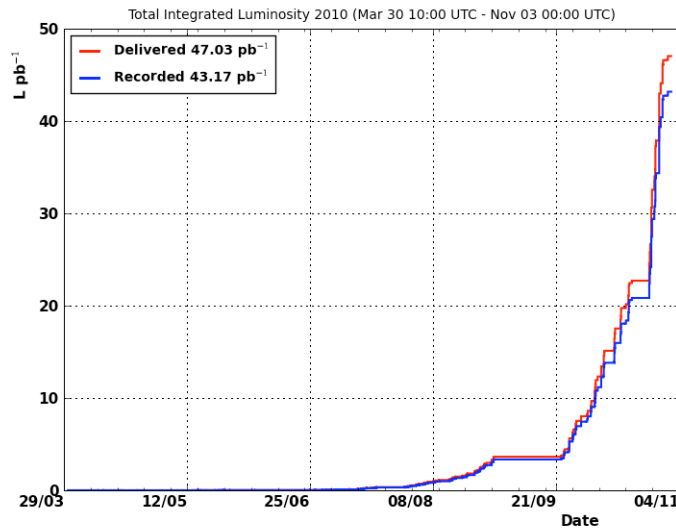
Figure 4-2. Integrated luminosity for 2010 [47]

Several scenarios were considered for the next phase of LHC operations which would begin in March of 2011. Among other less important issues, the energies of the beams and the total duration of the next run were topics to be addressed at the annual LHC Performance Workshop in Chamonix, France [48]. Increasing the beam energies

69

to 4 TeV was thought to be feasible, but ultimately it was decided to maintain the beams at their currently commissioned and well-understood energy of 3.5 TeV. It was known that a long shutdown period would be required to upgrade the machines to handle the design beam energies of 7 TeV. The question remained as to when this shutdown period would occur, as it is strongly coupled to the end, and hence duration, of the next physics run. While the experimental community was eager to analyze the future data produced at $\sqrt{s} = 14$ TeV, there was much more demand to have some discovery power with the data to be produced during the next run of the LHC. Therefore, the CERN council decided to begin the next run in March of 2011 and carry it through to the end of 2012 in the hopes that the accelerator would be able to deliver a total of 5 to 10 fb^{-1} of data. This much data would allow for the experiments to exclude the existence of various incarnations of the Standard Model Higgs' boson or see nearly conclusive evidence of its existence. As a result the next phase of the LHC operation is informally being referred to as the *Higgs Run*.

CHAPTER 5
THE CMS EXPERIMENT

The Compact Muon Solenoid (CMS) is a multi-purpose particle detector designed to operate in the high luminosity environment provided by the LHC. Located roughly 100 meters underground at Interaction Point 5 (IP5) of the LHC tunnel, the CMS detector boasts high-performance tracking, calorimetry, and particle identification which is needed to accommodate the ambitious physics goals of the LHC.

5.1   CMS Coordinate System

The CMS detector has adopted a coordinate system that is well-suited for a cylindrical apparatus operating in a hadron collider environment. The positive x-axis points towards the center of the LHC ring, while the positive y-axis points toward the sky. The z-axis lies along the beam pipe with the positive direction toward the Jura Mountains. The azimuthal angle ϕ is measured from the positive x-axis. The zenith angle θ is measured from the positive z-axis. The pseudorapidity is defined as $\eta = -\ln(\tan(\frac{\theta}{2}))$. The difference in pseudorapidity between two particles ($\Delta\eta$) represents a longitudinally invariant quantity.

As a convention different regions of $|\eta|$ within the CMS detector are often referenced. The most central region of the detector is often called the "barrel". Usually, this region spans $|\eta| \lesssim 1.1$. The region roughly defined over $1.1 \lesssim |\eta| \lesssim 3.0$ is often referred to as the "endcap", and the region beyond $|\eta| \gtrsim 3.0$ is referred to as "forward". The values of $|\eta|$ delineating these regions are taken to be qualitative, in general; however, in the context of particular sub-detectors, the geometry offers more precise boundaries in $|\eta|$ to separate these regions.

5.2   Design and Performance

The CMS detector was constructed completely above ground and then lowered piece-wise into the underground cavern designed to host the apparatus. Fully assembled,

the apparatus spans 21 meters in the z-dimension with a cylindrical radius of 15 meters and weighs nearly $12,500$ tons.

The general design of the CMS detector can be described as follows. The detector as a whole is cylindrical in shape and is composed of several sub-detectors. Starting from the nominal interaction point and moving outward in radius, the detector consists of a silicon tracking detector (Tracker) followed by an electromagnetic calorimeter (ECAL) and then a hadron calorimeter (HCAL). The superconducting magnet lies in between the main barrel HCAL sub-detector and an outer-barrel HCAL sub-detector. Beyond the magnet lies an extensive muon system. Figure 5-1 shows a full view of the schematic design of the CMS detector with the magnet and various sub-detectors labeled. Figure 5-2 shows the cross-section of the CMS detector in the r-z plane. The magnet and the individual sub-detectors will be discussed in more detail in the following sections.

It is worth discussing the monumental challenge involved in synchronizing the various sub-detectors. The LHC is designed to provide high-energy collisions every 25 ns. The particles which emerge from the collisions are relativistic in general and have speeds comparable to the speed of light $c = 2.98{\cdot}10^8$ m/s. Some simple arithmetic leads one to the startling conclusion that the debris from collision X will still be propagating through various components of the CMS detector while collision $X + 1$ is occurring. To be precise, the debris of collision X will be located at a radial distance of $(2.98 \cdot 10^8$ m/s$)\cdot(25 \cdot 10^{-9}$ s$) \approx 7.5$ m, which is still well-inside of CMS. Given that the CMS detector has a cylindrical radius of 15 m, the debris from collision X will just be leaving the periphery of CMS as collision $X + 2$ is occurring. Thus, detector synchronization is of paramount importance to ensure consistent event reconstruction.

In the sections that follow, the general design and function of the various CMS sub-detectors will be described. The role of triggering is inextricably tied to many of

the design aspects of the sub-detectors (apart from the Tracker); however, most of the discussion on the CMS trigger system will be deferred until later in section 5.2.6.

5.2.1 Superconducting Magnet

For many particle detectors of this kind, the configuration of the magnetic field greatly influences the overall design and attributes of the apparatus. CMS is no exception, as the superconducting solenoid imposes a cylindrical geometry on the detector which must be accommodated by the other sub-components. A strong magnetic field is needed to bend energetic charged particles for momentum measurements and electromagnetic charge assignments within the inner tracking volume (interior to the magnet) and within the muon system (exterior to the magnet). The bore of the magnet which hosts the quadruply layered coil windings must be large enough to host the the inner tracking system and calorimetry in its interior. This places a direct demand on the cylindrical radius of the solenoid and consequently a direct demand on the volume of space (or instrumentation) which will be permeated with magnetic fields. Magnetic fields store potential energy in an amount that scales with the volume and the square of the magnetic field. As a result the CMS solenoid stores an enormous amount of energy, roughly 2.6 GJ at full current.

Magnetic field lines form closed loops. Thus, the flux delivered by coils through the interior of the solenoid must be returned and is done so through a massive iron yoke composed of five wheels and two endcaps. This iron yoke also houses the muon systems, both in the barrel and endcaps. A muon therefore experiences counteracting deflections as it transitions from the interior of the solenoid to the exterior.

5.2.2 Tracking System

At design luminosity the LHC is expected to deliver ~ 20 collisions per bunch crossing (i.e., per 25 ns), which implies a number of charged particles of order 1000 will emerge from the interaction region. The inner tracking system is the first sub-detector these particles will encounter. To handle the huge flux of particles, the tracking system

73

Superconducting Solenoid

Silicon Tracker

Pixel Detector

Very-forward Calorimeter

Preshower

Hadronic Calorimeter

Electromagnetic Calorimeter

Muon Detectors

Compact Muon Solenoid
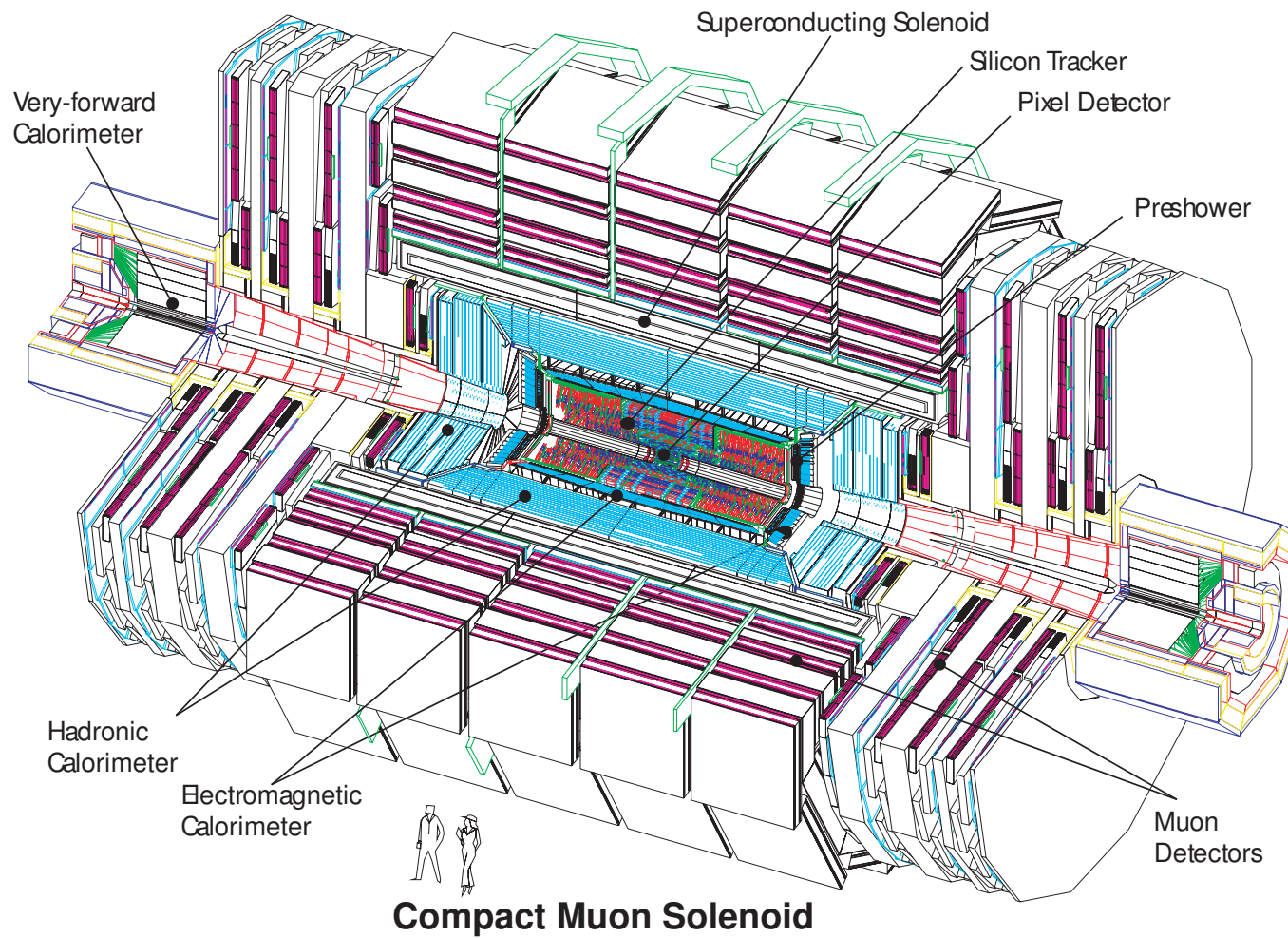
Figure 5-1. CMS detector (full view)
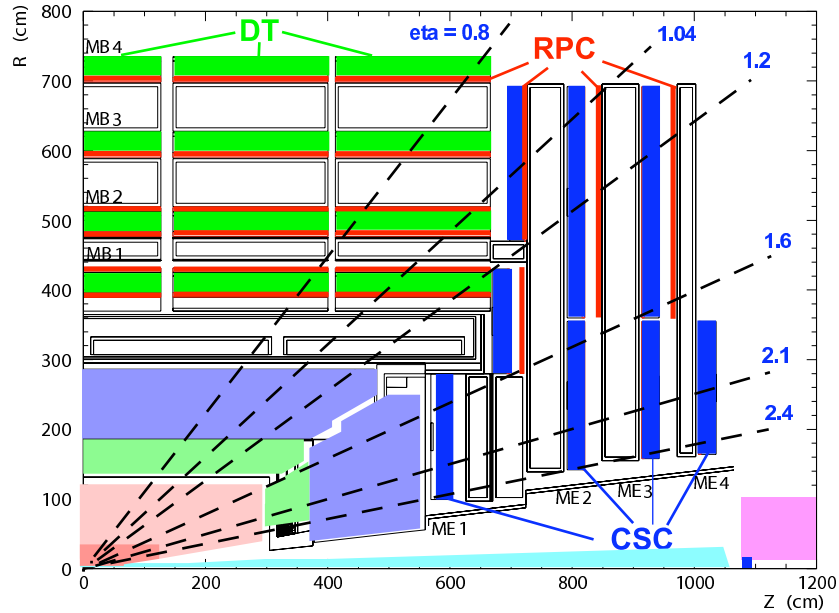
Figure 5-2. CMS detector (r-z profile)

must be radiation-hard and highly granular with a fast response. Thus, the choice of silicon for the active material is well-motivated to meet the strict demands imposed by LHC.

The inner tracking system consists of two main components. The innermost component is a silicon pixel detector, which consists of three active layers and spans a radius of 4.4 cm $< r < 10.2$ cm in the barrel region. Two disks comprise the endcaps of the pixel detector. Behind the pixel detector lies a silicon strip detector, which is the second component of the inner tracking system and occupies the region up to $r = 1.1$ m in the barrel. The endcaps of the silicon strip detector consist of 12 disks in total, yielding a tracking acceptance in pseudorapidity up to $|\eta| < 2.5$. To accommodate the huge influx of particles, the tracking system is required to be dense with numerous read-out channels to distinguish the interactions from the multitude of particles. A high-density tracking volume comes with several undesirable consequences. They consume a lot of power and thus require sophisticated and efficient coolings systems on-board, and they increase the likelihood of a wide variety of destructive particle

75

interactions (e.g. nuclear interactions, bremsstrahlung, photon conversions, and multiple particle scattering). These unwanted interactions can compromise the accurate measurement of various particle attributes by the ECAL, HCAL and Muon system which are located behind the tracking system. There is a delicate balance between having enough material to make the intended measurements of charged particles and not adding too much material to cause unwanted interactions; the CMS tracking system exemplifies such balance, providing high-precision tracking and vertex measurements at the cost of $0.4X_0$-$1.8X_0$ (radiation lengths) depending on the pseudorapidity.

The pixel detector provides 3 distinct measurements of position in space as a charge particle traverses it, while the strip detector offers from 9 to 14 additional measurements depending on the particle's pseudorapidity. The solenoid provides a homogeneous magnetic field of 3.8 Tesla which permeates the tracker volume, allowing for precision measurements of charged particles' momenta and electromagnetic charge. Aside from momentum measurements, the CMS tracking system also allows for the reconstruction of various other observables. Perhaps most important is the reconstruction of the event primary vertex (PV). Using the information from several reconstructed charged tracks, the location of the primary collision in 3-dimensional space can be measured with high precision. With high luminosity conditions, multiple primary vertices are expected from pile-up (PU). Thus, it is vital to be able to match charged tracks accurately to these respective vertices for a consistent event reconstruction. Also important is the ability to reconstruct secondary vertices (SV) from short-lived, heavy-flavor decays (e.g., B and D mesons). These are essential for b-jet identification (b-tagging) and tau-lepton reconstruction. Related to secondary vertex reconstruction is the measurement of the transverse impact parameter d_0, which is useful to discriminate muons and electrons of resonance decays (e.g. W and Z-bosons) from those of heavy-flavor meson decays.

Figure 5-3 shows a geometric representation of the transverse impact parameter d_0 and how it can be calculated. In this diagram we assume that there exists some relativistic short-lived, heavy-flavor meson, denoted a, which travels a finite distance V_T in the transverse plane and then subsequently decays to particles b and c. For simplicity, we assume object b is a muon and object c represents the rest of the decay products (typically a muon-neutrino and a group of hadrons). The tracks from the decay products are used to reconstruct a secondary vertex. Two observables are needed to reconstruct the transverse impact parameter: 1) the x-y position of the secondary vertex with respect to the primary vertex and 2) the unit vector along the transverse momentum of the muon. It is left to take the cross-product of the two vectors and project along the z-axis:

$$d_0 = (\hat{P}_T \times \vec{V}) \cdot \hat{z} = \frac{V_x \cdot P_y - V_y \cdot P_x}{|P_T|} \tag{5–1}$$

where we are assuming the primary vertex is located at $(0, 0)$ for simplicity. While the reconstruction of a secondary vertex was assumed for this example, it is not explicitly required in order to calculate d_0 for a given charged track. When the momentum of a charged particle is reconstructed by the tracker, the vertex from which it originated is easily calculated from the track fit. The error on the secondary vertex, which includes multiple tracks, will in general be smaller than the error on the vertex of a single track. Nonetheless, the vertex precision for single tracks is still good enough to measure d_0 with good precision for a wide range of track p_T.

The CMS tracker exhibits excellent resolution of key observables such as p_T and d_0. Table 5-1 shows their resolutions for a few different muon p_T scales [38]. The spread in values reflects the η dependence on the resolutions, which is not explicitly shown. To demonstrate that the muon d_0 resolution is more than good enough to identify heavy-flavor decays, we can appeal to a simple example. Again, referring to the diagram in Figure 5-3, we take particle a to be a typical B or D meson. These have masses
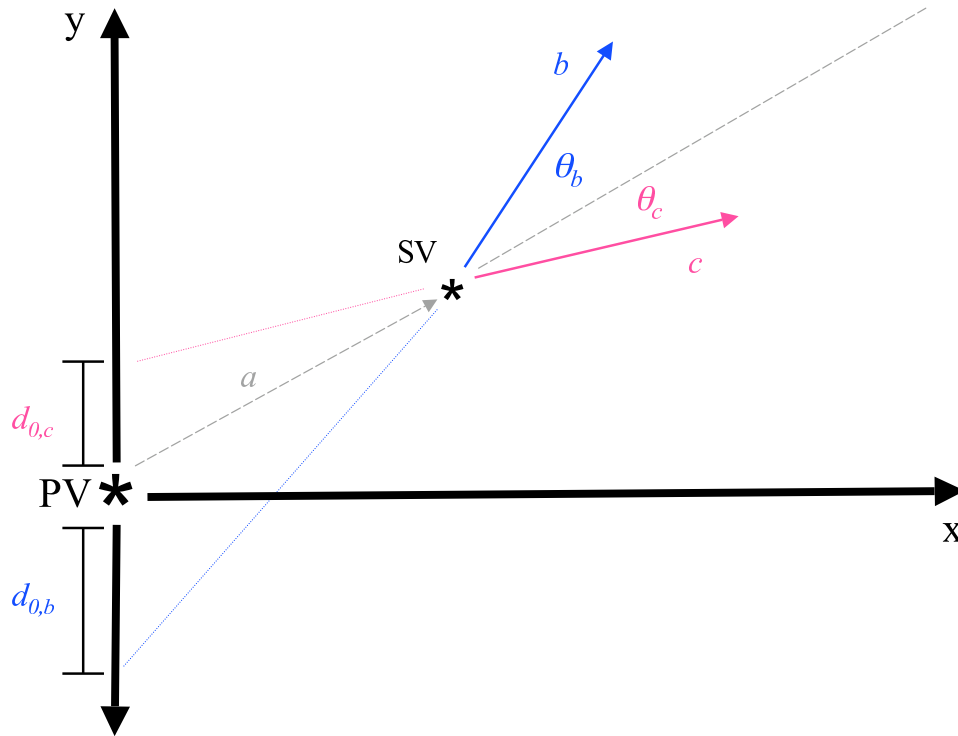
Figure 5-3. Pictorial representation of transverse impact parameter d_0

on the order of 5 GeV and lifetimes on the order of 10^{-12} s. The mean distance V traveled by a relativistic particle as measured in the lab frame is $V = \gamma v \tau$, where γ is the relativistic boost also given by the ratio of energy to mass (E/m), v is the velocity of the particle which is very nearly the speed of light c, and τ is the mean life time. Roughly $1/e \sim 37\%$ of particles with these values of γ, v, and τ will travel this distance V before decaying as it is a Poisson process. Light decay products of relativistic particles typically form a decay angle of $\theta \sim 1/2\gamma$ with respect to the direction of the parent particle in the lab frame. If we assume particle a to have an energy of 50 GeV (not uncommon), then $\gamma = E/m = 50/5 = 10$ and $d_0 = V \cdot sin(\theta) = \gamma c \tau sin(\frac{1}{2\gamma}) \approx 1.5$ mm. In principle, particle a can take on any value of $|\eta|$ within the tracking acceptance. For the extreme case where

$|\eta| = 2.4$, then $V_T = V/cosh(\eta) \approx 0.27$ mm, which is a factor of 10 greater than the d_0 resolution for muons in the range of $p_T > 10$ GeV. Finally, it is worth noting that the scale of the impact parameter depends mostly on the characteristic lifetime of the decaying particle, as the dependence on the energy cancels as γ grows high enough to merit the small-angle approximation of the $\sin$ function.

Table 5-1. P_T and d_0 resolution for muons

p_T (GeV)	$\sigma(\delta p_T)$%	$\sigma(\delta d_0)$ (μm)
1	$0.7 - 2.0$	$90 - 200$
10	$0.7 - 2.0$	$20 - 30$
100	$1.5 - 7.0$	$10 - 12$

5.2.3   Electromagnetic Calorimeter

The CMS Electromagnetic Calorimeter (ECAL) is a homogeneous detector composed of lead-tungstate (PbWO4) crystals coupled to Avalanche Photodiodes (APDs) in the barrel and Vacuum Photodiodes (VPDs) in the endcap. The barrel contains $61,200$ distinct crystals which cover the range up to $|\eta| < 1.479$, while each endcap consists of $7,324$ crystals which span the range of $1.479 < |\eta| < 3.0$. Like the inner tracking system the ECAL is designed to be radiation-tolerant, exhibiting high granularity and a fast timing response. The design was greatly motivated by the intense operating conditions of the LHC and the strict performance requirements necessary to pursue the discovery of the Higgs boson decay into two energetic photons ($H \rightarrow \gamma\gamma$). An excellent energy and timing resolution is especially necessary for the latter pursuit.

Two figures of merit which are often used to characterize the material in electromagnetic calorimeters are the radiation length X_0 and the Molière radius r_M. The radiation length represents the mean path length that a high energy electron(or positron) must travel in order to release $\approx 63\%$ of its energy through bremsstrahlung radiation. For high energy photons, this quantity also represents the mean distance necessary to travel in order to release $7/9$ of its energy via e^+e^- pair-production. The Molière radius represents the radius of a cylinder which would contain $\approx 90\%$ of the electromagnetic shower induced

by an energetic electron or photon in the dimension transverse to the particle's motion. For the lead-tungstate crystals in the ECAL these values are $X_0 = 0.89$ cm and $r_M = 2.2$ cm . The dimensions of the crystals are tailored with these values in mind, as the front (back) surface area is 2.2×2.2 cm (2.6×2.6 cm) and the longitudinal depth is about 23 cm, which offers roughly 25 radiation lengths of material. The probability for the ECAL to completely contain the electromagnetic shower induced by an impinging photon or electron is effectively 100%.

The front of the ECAL barrel (EB) lies just beyond the inner tracking system, beginning at a radius of 1.29 meters, while the ECAL endcaps (EE) are located just over 3 meters away from the nominal interaction point. Positioned in front of the endcaps is the ECAL Preshower system (ES), which is a sampling calorimeter composed of a radiation-inducing layer of lead followed by an energy-collecting layer of silicon strips. The main function of the preshower detector is to help the ECAL resolve the photon pairs coming from $\pi^0 \rightarrow \gamma\gamma$, which is an abundant background process to important searches like $H \rightarrow \gamma\gamma$. In the former process the two photons are likely to be very near one another, owing to the $\sim 1/\gamma$ opening angle, and would potentially be reconstructed as a single photon in the ECAL endcap. However, these photons impinge upon the preshower detector first, which offers a much higher granularity than the ECAL endcap. The resulting electromagnetic showers from the di-photon system is seen as two distinct showers with the help of the preshower, instead of one. This additional photon discrimination power is available over the pseudorapidity range of $1.653 < |\eta| < 2.6$. The preshower provides 3 radiation lengths of material over this range, effectively guaranteeing that electrons and photons will begin to shower before reaching the endcaps.

The energy resolution of the ECAL sub-detector was studied in 2004 with LHC test beam data. The beams consisted of electrons with energies ranging from 20 to 250 GeV.

The general expression for a calorimeter's energy resolution can be written as:

$$\left(\frac{\sigma}{E}\right)^2 = \left(\frac{S}{\sqrt{E}}\right)^2 + \left(\frac{N}{E}\right)^2 + C^2 \tag{5–2}$$

where S represents a stochastic term (e.g., fluctuations in photostatistics, lateral shower containment, energy radiated in the preshower), N represents a noise term (e.g., electronics, digitization, pile-up), and C represents a constant term (e.g. non-uniformity of light collection, inter-calibration errors, energy leakage from back of crystals). The test beam results suggested the following values for these terms in Eq. 5–2: $S = 2.8\%$, $N = 0.12\%$, and $C = 0.3\%$ [38]. It will take time to to collect enough data to measure the energy resolution using collision particles. However, with the first 250 nb^{-1} of pp collision data at $\sqrt{s} = 7$ TeV, the resolution of the neutral pion mass was measured to be just under 10%. The energy scale which is typically represented by $|E_{measured} - E_{true}|/E_{true}$ could also be estimated with this early data and was found to be about 1% and 3% for the barrel and endcap respectively [49]. These measurements demonstrate the rather impressive capabilities of the ECAL sub-detector during the early commissioning phase of the experiment.

When the LHC began colliding protons in 2009 and 2010, an unexpected rate of anomalous high energy signals was observed in the ECAL barrel sub-detector. These signals did not reflect the conventional electromagnetic showers from impinging electrons and photons. Rather, they appeared to be spurious energy deposits from direct ionization of the silicon residing in the APDs. ECAL experts suspect that the phenomenon can be attributed to back showering in the hadron calorimeter or neutron decays. Fortunately, the topological and timing signatures of these anomalous signals can be distinguished from the intended collision-induced signals, and algorithms are in place to reject these deposits during event reconstruction.

5.2.4 Hadron Calorimeter

Located primarily behind the inner tracking system and ECAL, the CMS hadron calorimeter (HCAL) is designed to measure the energies from neutral and charged hadrons, which provide the foundation for quark and gluon-jet reconstruction and the calculation of the missing transverse energy ($\not{E}_T$). The HCAL sub-detector consists of four components. These are referred to as the HCAL barrel (HB), endcap (HE), forward (HF), and outer (HO). Together, they cover a pseudorapidity range up to $|\eta| < 5.0$, making the CMS detector almost perfectly hermetic.

When energetic hadrons impinge upon a dense material, they initiate pion (π^+,π^-,π^0) cascades through nuclear interactions with the medium. Because π^0's are likely to be produced in roughly equal proportions with respect to the charged pions, and these particles decay almost instantaneously into two photons, there is a substantial electromagnetic shower that develops, accompanying the hadronic shower carried out by the charged pions. This is unlike the situation for electrons and photons which impact the ECAL and only initiate electromagnetic showers. The two types of showers have very different characteristics owing to the underlying physics. Hadronic showers are carried out over much longer distances and involve interactions with the nucleons in the medium which result in some undetectable energy losses (i.e., energy that does not result in scintillation light). This phenomenon results in an intrinsic difference in the way a calorimeter would perceive an energy signal from an electron versus a charged pion, if the two were to impact the detector with identical incident energies. This ratio of the energy response of hadrons with respect to electrons is often denoted h/e, and its deviation from unity causes significant obstacles for performing energy measurements in the field of calorimetry.

While the radiation length X_0 is used to characterize the scale of electromagnetic cascades in calorimeters, the interaction length λ_I is used to describe the scale of hadronic showers. The interaction length represents the mean distance a relativistic

82

hadron must travel through a material in order to release roughly 63% of its energy via nuclear interactions. For the brass-steel absorber used for the HB and HE, $X_0 \approx 1.5$ cm and $\lambda_I \approx 16$ cm. The latter is roughly $18\times$ larger than the radiation length needed for electrons and photons in the ECAL. Aside from justifying the placement of the HCAL behind the ECAL, the scale of λ_I imposes some severe design, and more importantly, performance constraints on the HCAL and the CMS detector as a whole.

From the design perspective hadron calorimeters almost always are chosen to perform measurements by sampling the hadron induced showers because it is simply too expensive to fully instrument the dozen interaction lengths (several meters) needed to completely contain the shower energy with a homogeneous, active material (as is done in the ECAL). Moreover, once one is resigned to employing a sampling calorimeter for the task of measuring hadrons, the issue of cost is somewhat alleviated, but the issue of space is still an enormous concern. In CMS the HB is constrained to fit in between the ECAL barrel and the inner surface of the magnet. This area spans 1.77 m to 2.95 m in radius, and only affords the HB with about $5.8(10.6)$ interaction lengths at $\eta = 0(1.3)$. Thus, in rare cases where a single hadron is endowed with an unusually large energy from the collision event, the hadronic shower induced in the HB may not be contained and may carry on into the magnet and beyond. This uncontained energy would not be accounted for and this would cause a potentially high, but spurious, missing energy signal as well as a badly mis-reconstructed jet. Fortunately, the CMS geometry allowed for a safeguard to be employed in order to mitigate this effect. Located just on the exterior of the magnet, the HO component of the HCAL is meant to reinforce the HB by exploiting the additional absorber offered by the solenoid coil and appending it with additional sampling material, thus combining to yield 11.8 interaction lengths in total. The HO is often referred to as a *"tail catcher"*, which reflects its role in containing the hadronic showers induced by rare energetic particles. For collisions occurring at $\sqrt{s} = 7$ TeV, the probability that the HO will be needed for shower containment is much lower

than for the $\sqrt{s} = 14$ TeV collision scenario initially envisioned for the LHC; nonetheless, the HO will serve its purpose more as the LHC eventually approaches design energies.

The HB, HE, and HO sub-detectors share similar design qualities. They are all sampling calorimeters which employ an admixture of steel and brass absorber material to induce hadronic and electromagnetic showers. The photons generated from these showers are sampled at various longitudinal depths by several layers of plastic scintillator tiles. Embedded in these tiles are wavelength shifting (WS) fibers, which collect scintillation light and stream it to Hybrid Photodiodes (HPDs). The functional unit of this brass and scintillator construction is an HCAL *tower*. Towers define the granularity of the sub-detector. The HB geometry accommodates 72 towers in the ϕ dimension ($5°$ granularity) and 32 towers in the η dimension (0.087 granularity), which spans $|\eta| < 1.3$. The boundary towers on the η periphery of HB are shared with HE in what is referred to as the HB/HE transition region. The HB towers are mounted just behind the ECAL barrel sub-detector, and each one couples or maps to a 5×5 matrix of ECAL crystals lying directly in front of it with respect to the nominal interaction point. This union of ECAL crystals with an HCAL tower is referred to as a standard *calorimeter tower* or *calotower* for short. In the endcap a similar union is made, and in the forward region, calotowers consists of solely the towers from the HF sub-detector, as the ECAL does not extend that far in pseudorapidity.

The HE sub-detector covers the pseudorapidity region from $1.3 < |\eta| < 3.0$ and provides about 10 interaction lengths (including the contribution from ECAL). There are 72 calotowers in the ϕ dimension and 26 in the η dimension, if one includes the two η-rings shared with HB in the transition region. This yields a $\phi \times \eta$ granularity of $5° \times 0.087$ for $|\eta| < 1.6$ and approximately $5° \times 0.17$ for $|\eta| > 1.6$.

Unlike the HB, HB, HO components of HCAL, the HF detector has a very different design, which is motivated by its very vulnerable positioning at $3.0 < |\eta| < 5.0$ where the particle flux from collisions will be extremely intense. The HF detector will suffer

more radiation dosage than any other main sub-detector on CMS. Furthermore, the HF detector is required to sustain functionality and maintain a high level of performance to withstand approximately 10 years of nominal LHC operations. Ultimately, it was decided to instrument the HF detector with a passive steel absorber to induce nuclear and electromagnetic showers, and embedded this medium with quartz fibers to detect the resulting Chrenkov radiation from the secondaries.

The HF effectively consists of two longitudinal segments. Half of the quartz fibers span the entire longitudinal dimension, while the other half begin at a distance 22 cm from the front of the HF and span the rest of the depth. These two collections of fibers are referred to as "long" and "short" fibers respectively, and they are read-out separately from each other (not combined) via photomultiplier tubes (PMTs). Using the two sets of quartz fibers, showers from electrons and photons can be distinguished from showers induced by hadrons. Electrons and photons will release most of their energies within a few radiation lengths (i.e., much less than 22 cm). Thus the majority of the Chrenkov light emitted from these electromagnetic showers will be confined to the long fibers. Hadrons on the other hand release their energies over a longer distance on the scale of a few interaction lengths. Thus, signals from hadrons will be collected almost uniformly over long and short fibers. The HF detector is located roughly 11.2 meters from the interaction point and contains 36 calotowers in the ϕ dimension and 26 calotowers in the η dimension, yielding a $\phi \times \eta$ granularity of $10° \times 0.17$ for $|\eta| < 4.72$ and approximately $20° \times 0.30$ for $|\eta| > 4.72$.

The HF detector also performs luminosity monitoring of the LHC. Employing a technique known as "zero-counting", the average number of towers which report zero energy signal per bunch-crossing can be counted in the HF and this number can be related to the average number of interactions, and hence the instantaneous luminosity can be inferred. More details of this and other methods for luminosity monitoring in the HF can be found elsewhere [38].

The energy resolution for hadron calorimeters is generally worse compared to electromagnetic calorimeters. Due to their sampling nature, they are especially prone to fluctuations in the photostatistics. This contributes a significant stochastic term to the expression for the resolution (see Eq. 5–2). There is also a non-trivial constant term that originates primarily from the non-unity of the h/e ratio. As implied by the discussion on calotowers, the measurement of hadron energies up to $|\eta| < 3.0$ relies on a combined measurement of the ECAL(homogeneous) and HCAL(sampling) sub-detectors. A significant fraction of hadrons will inevitably begin to shower while traversing the ECAL, which provides just over one interaction length of material. For these cases, the hadronic component of the showers will carry on well into the HCAL, but the majority of the initial electromagnetic component may very well be contained to the ECAL, which has a different h/e ratio. Thus, there is a complicated marriage between the energy measurements registered by the ECAL and HCAL to reconstruct the incident hadron's true energy. This union affects the total energy resolution for hadrons in a non-trivial way. Some sophisticated techniques were employed to correct for the differing h/e ratios using test beam data, which were able to bring the energy resolution for HB and EB combined system down to the following value [50]:

$$\left(\frac{\sigma}{E}\right)^2 \sim \left(\frac{84.7\%}{\sqrt{E}}\right)^2 + \left(7.4\%\right)^2 \tag{5–3}$$

The HE sub-detector has a similar scale of energy resolution with the stochastic term giving the dominant contribution, while the HF has a stochastic and constant term of $280\%(198\%)$ and $11\%(8\%)$ respectively for the hadronic (electromagnetic) showers [51].

A significant effort is in place on CMS to measure the HCAL mean energy response of charged pions with collision data. This measurement was performed with the first 10 nb^{-1} of minimum-bias collision data collected at $\sqrt{s} = 7$ TeV. The subset of charged

pions which begin their hadronic showers in the HCAL can be identified with a fairly simple selection. One just requires an isolated charged track with $p_T > 5$ GeV as measured by the Tracker, combined with a minimum-ionizing particle (MIP) signature in the ECAL. Using these pion candidates, the HCAL mean response can be evaluated over the pseudorapidity range covered by the Tracker ($|\eta| \lesssim 2.4$). In the HB the response (E_{HCAL}/p_{Track}) varies from 60% at $p_T = 5$ GeV to about 80% at $p_T > 12$ GeV. In the HE, the response takes on values of 50% at $p_T = 5$ GeV, about 75% at $p_T = 12$ GeV and about 92% and $p_T > 20$ GeV. It is important to extract the mean pion response function for the calorimeters, which varies with respect to p_T and $|\eta|$, as it is needed in order to improve the reconstructed jet and $\not{E}_T$ energy scales.

Some sources of anomalous noise in the HCAL have been identified either during the CRAFT (Cosmic Run At Four Tesla) exercise of 2008 and 2009 or the 2010 collision runs. They have been studied thoroughly by experts. Two main classes of anomalous signals are worth mentioning as they have reasonably high rates of occurrence. The first class is the so-called HPD and RBX (Readout-BoX) noise which exists in the HB, HE, and HO sub-detectors. An HPD contains 18 readout channels and there are 4 HPDs per RBX. An HPD can experience what is called *ion-feedback* which occurs when a photoelectron liberates ions from the silicon diode, which subsequently accelerate across the high-voltage (HV) gap and bombard the photocathode, thus freeing more photoelectrons. This causes a single readout channel on average to report a spurious signal and can occur at a rate of ~ 20 Hz. An HPD can also experience a sizable discharge due to effects from the HV interplay with the CMS magnetic field. This can lead to up to 18 channels reporting false energy signals and occurs at a rate of ~ 1 Hz. The most catastrophic case occurs when all of the constituent channels of an RBX register a signal. The exact cause of this phenomenon is unknown, but it can affect all 72 channels and can occur at about ~ 0.5 Hz. The probability of these noise events to overlap with collisions is quite low, but they produce signals that could mimic those of

new or exotic physics processes (e.g., $\not{E}_T$, mono-jets). Thus, special filters have been developed to identify these events by their timing and topological signatures and they can consequently be rejected.

The second class of noise exists in the HF sub-detector and is referred to as "PMT hits". This phenomenon occurs when Chrenkov light is produced by particle interactions that occur in the window material of the PMTs (instead of the absorber in front) [51]. Fortunately, the signals that come from such effects can be identified and rejected via topological, timing, and pulse shape filters.

5.2.5 Muon System

There is a reason why the CMS detector features "Muon" as its middle name. Since the earliest design phases it was always envisioned that robust muon identification and high precision momentum measurements would be two of the key deliverables of the LHC candidate experiment which was later going to be known as the Compact Muon Solenoid. In part this desire was motivated by the discovery potential of the Higgs boson via the decay $H \to ZZ^{(*)} \to \ell^+\ell^+\ell^-\ell^-$, where all four decay products are muons. Owing to their MIP nature, muons are extremely clean objects and easily navigate through the material of the inner tracking system, calorimeters, and magnet without succumbing to the drastic radiative energy losses or nuclear interactions as do other detectable particles (e.g., electrons, photons, pions). They exit these systems with virtually the same momenta as they had when they were born from the primary collision. Thus, the placement of an additional tracking sub-detector outside of these other systems allows for muon identification and another measurement of the momentum which is completely independent of the inner tracking system.

The Muon System consists of three types of gaseous tracking detectors. In the barrel region ($|\eta| < 1.2$) where the muon rate is expected to be low and the returning magnetic field is weak, drift tube chambers (DT) are employed. In the endcaps ($0.9 < |\eta| < 2.4$) where the muon rate increases and the magnetic field is stronger, Cathode

Strip Chambers (CSC) are installed. A third system of Resistive Plate Chambers (RPC) is also present in the barrel and endcaps up to $|\eta| < 1.6$ and provides complementary and redundant tracking and timing measurements to aid the CSC's and DT's in muon reconstruction and triggering.

The drift tube system consists of four chambers which form concentric cylindrical shells around the magnet in the barrel (denoted MB1, MB2, MB3, and MB4). They are interspersed in between the various layers comprising the iron yoke which returns the magnetic field of the solenoid. These chambers span the z-dimension in the form of 5 wheels, which are provided by the frame of the iron yoke. Each wheel is divided into 12 sectors spanning the azimuthal dimension. The functional unit of the drift tube chamber is what is referred to as a *superlayer*. The innermost 3 chambers contain 3 superlayers each while the outermost chamber contains only 2. A superlayer is further granulated into 4 layers of radially staggered, but otherwise parallel, drift cells, which have the design depicted in Figure 5-4. An anode wire installed in the geometric center of the tube is charged to a very high electric potential (HV) of $+3.6$ kV. Cathode strips which line the interior of the I-beams are charged to a high negative electric potential of -1.2 kV. Electrode strips span the top and bottom interior layers and are charged a potential of $+1.8$ kV. The net effect of this anode-electrode-cathode configuration is a powerful electric field which emanates from the anode, is steered by the electrodes, and terminates at the cathodes.

The drift cell performs a spatial measurement via the following mechanism: A charged particle (e.g. a muon) traverses the gaseous volume within the cell and ionizes the gas atoms along its trajectory. The liberated electrons begin to drift to the positively charged anode at a constant drift velocity determined by the gas pressure and the net electric field. As these electrons get close to the anode they begin to accelerate due to the increasing electric field (proportional to $\sim 1/r$). This acceleration endows the electrons with enough kinetic energy to kick out electrons from neighboring gas atoms,

which then begin to accelerate towards the anode themselves, giving rise to a *run away* charge accretion or *charge avalanche* which is localized on the anode. This amplification effect is often referred to as a *gas gain* and can be as high as 10^5. The passage of time between the traversing particle and the arrival of the liberated electrons to the anode constitutes the drift time. With the drift time measured and the drift velocity known, the location of the incident charged particle transverse to the anode can be reconstructed. The drift tube technology relies on the residual magnetic field from the solenoid being weak and mostly uniform. If the drifting electrons experience a magnetically induced Lorentz force, their trajectories may take on helical patterns (instead of directly along electric field lines), which can alter their drift times in a non-trivial way.

For a typical chamber the first and third superlayers will contain drift cells with wires that are aligned with the beam line and thus provide azimuthal measurements (ϕ). The middle superlayer contains drift cells with wires that lie orthogonal to the beam and thus provide measurements of the z position. The forth chamber only contains two superlayers and therefore only provides a ϕ measurement. In total the DT's comprise 250 chambers.
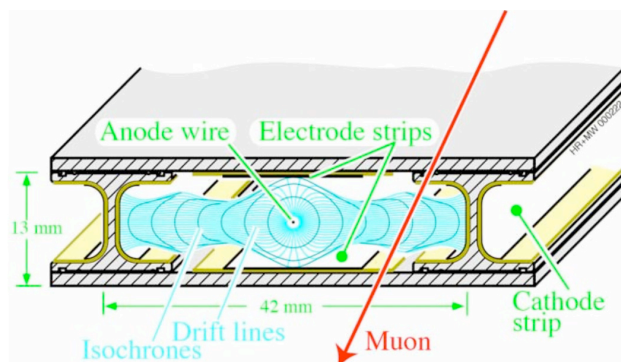
Figure 5-4. Schematic design of drift tube cell [52]

The drift tube anode wires are stainless-steel with gold plating and have a diameter of 50 μm. The cathode lining the drift cell interior edges is made of aluminum tape which is 50 μm thick and 11.5 mm wide. The tubes have a geometrical cross-section of

13×42 mm^2. The gas filling the cells is a $85\%/15\%$ admixture of Ar/CO$_2$, which yields an electron drift velocity up to about 5.4 cm/μs (saturated value). Drift times range from a few to ~ 400 ns depending on the location of the initial ionization. Each wire is designed to provide a spatial resolution of about 250 μm. When combining the measurements over several superlayers, the global design resolution in the $r - \phi$ plane is on the order of 100 μm.

The endcap muon system is instrumented with Cathode Strip Chambers, which are modeled after the *multi-wire proportional chamber* particle detection technology first engineered by Charpak [53]. Each endcap features 4 stations spanning the z-direction. Station 1 is composed of 3 rings stacked in the radial direction while stations 2 through 4 contain 2 rings by design. A given station and ring is denoted as $MB \pm S/R$ where the $\pm$ denotes the plus or minus-side endcap with respect to the z-axis, S denotes the station number, and R denotes the ring. The implementation of $ME \pm 4/2$ has not actually been completed as of 2011 and plans are in place to install it in the next few years.

The functional unit in the endcap muon system is the chamber, which is trapezoidal in shape as is depicted in Figure 5-5. A chamber consists of 6 anode wire planes which are orthogonally interspersed among 7 cathode panels. The anodes span the azimuth dimension and measure the radial coordinate while the strips span radially and measure the azimuthal coordinate. The anode-cathode system is maintained at an HV of 3.6 kV. The 7 panels provide 6 gas gaps which contain a gas mixture composed of 50% CO$_2$, 40% Ar, and 10% CF$_4$. This gas mixture, combined with the HV condition, provides a gas gain of roughly 7×10^4.

The process by which the CSC's perform a spatial measurement is the following: A charged particle (e.g. a muon) traverses a gas gap within a chamber, ionizing gas atoms along its trajectory. The HV maintained between the anode wire and the cathode strips creates a strong electric field which imposes a drift velocity on the liberated electrons towards the anode (similar to the mechanism in the drift cell). As the drifting electrons

get close to the anode they begin to experience a large acceleration which allows them to impart enough energy to knock out electrons from neighboring gas atoms. These freed electrons join suit and proceed to knock out other electrons and the *run away* process (or *avalanche*) occurs in a manner similar to that of the drift cells. The charge that accumulates on the anode induces a differential charge distribution across the group of nearby cathode strips. This distribution of charge will reflect the location on the anode where the avalanche occurred. By synthesizing this information, one can simultaneously deduce the 2-dimensional $r - \phi$ spatial position that was traversed by the incident charged particle.

Depending on the ring and station position of the chamber, it may span either $10°$ or $20°$ in ϕ. The largest chambers are located at $ME \pm 2/2$ and $ME \pm 3/2$ and cover an area of 3.4×1.5 m^2. The multiplicity of chambers as a function of station and ring is given in Table 5-2. Muons in the pseudorapidity range of $1.2 < |\eta| < 2.4$ will cross, and hence be measured (ideally), by 3 to 4 stations, while muons in the range of $0.9 < |\eta| < 1.2$ will be measured both by the DT's and at least one of the CSC's.

The CSC's performance and calibration fortunately do not rely on precise control of the temperature and pressure of the gas. Unlike the DT's, the CSCs do not base their measurements on drift times, which can suffer ill-effects from unstable gas pressures or strong magnetic fields. The pseudorapidity region covered by the CSC's guarantees that they will not only see a higher rate of collision muons, which justifies their faster response times when compared to drift cells, but they will also endure a stronger and non-uniform magnetic field. In fact, $ME \pm 1/1$ has a slightly different design to cope with its unique placement close to the beam line and interaction point, where the magnetic field is nearly full strength. The anode wires, for example, are not perfectly azimuthal, but tilted at an angle of $\approx 29°$ to compensate for the magnetic deflection that drift electrons will experience as they travel towards them.
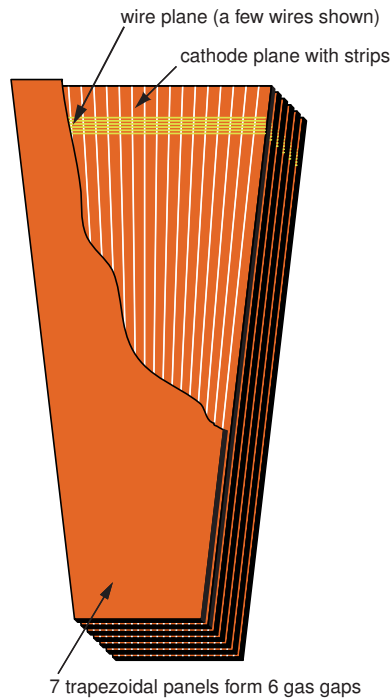
Figure 5-5. Schematic design of a cathode strip chamber [38]

Table 5-2. Chamber multiplicity per station and ring

	Ring 1	Ring 2	Ring 3
Station 1	72	72	72
Station 2	36	72	-
Station 3	36	72	-
Station 4	36	(72)	-

The Resistive Plate Chambers (RPC) are parallel-plate gaseous detectors, which provide complimentary spatial and timing measurements to the DT and CSC subsystems. The RPC's are instrumented in the barrel and endcap region up to $|\eta| < 1.6$. Initially, it was intended the RPC's would cover the region up to $|\eta| < 2.1$, but budget concerns compelled the collaboration to delay this full implementation until a later time.

The functional unit of an RPC is the double-gap module. A chamber will either contain two or three of these. In the barrel, these are aligned sequentially along the beam direction. The individual gaps are stacked such that a charged particle from the interaction point would traverse both gaps in the double-gap module. There is some

staggering to minimize the dead regions. Each of the single gaps in a double gap module is bounded by two planes of graphite, which are charged to high voltage. The interior of the graphite planes is lined with a 2 mm thick bakelite layer, which is highly resistive. Up to 96 copper readout strips lie in the region between the two graphite planes which line the common border of the single gaps of the double gap structure. The single gap has a thickness of 2 mm and is filled with an admixture of gases of the following composition: 96.2% $C_2H_2F_4$, 3.5% C_4H_{10}, and 0.3% SF_6. These gases play a crucial role in the operation of the RPC's.

An RPC detects the passage of a charged particle via the following mechanism: A charge particle penetrates the gas gaps causing ionization along its trajectory. Because this is a parallel plate capacitor configuration, the electric field which results from the applied HV, is strong and uniform over the volume of the gap. Thus, the electrons which are liberated during the ionization process begin to immediately accelerate towards the +HV side of the gap (away from the strips). This is unlike the case of the drift tubes, where the electrons experience a casual drift until they get to within a few wire radii of the anode wire, owing to the $1/r$ dependence on the electric field. The CMS RPC's operate in *avalanche mode*, which means the electrons from the initial ionization will liberate some amount of additional electrons en route to the resistive plates, but not enough electrons to cause dielectric breakdown and ignite a spark across the gap. Several factors allow for the avalanche to be controlled and localized. For one, the gas mixture in the gap not only provides candidate atoms for ionization, but it also contains negative charge carriers and is absorbent to photons in the UV range. The negative charge carriers pick up some of the liberated electrons in the avalanche, and the photons, which are emitted during the discharge process as the electrons reach the plate, are absorbed by the gas. Otherwise, these photons could initiate some ionization elsewhere in the RPC's. The high resistivity of the plates makes it difficult for the HV source to quickly compensate for the charge that has accumulated as a result of the

avalanche. This causes a drop in the electric field local to the avalanche, which induces a current on the read-out strips.

A charged particle crossing the plane of an RPC will induce signals in a neighborhood of strips. These strips get clustered together, and the path traversed by the incident particle is inferred by calculating the centroid of the area covered by the strips. This produces a spatial resolution of about 10 mm; however, the noteworthy feature of the RPC is its timing resolution, which is on the order of ~ 3 ns.

The RPC's in the barrel form 6 coaxial cylinders spread across the four DT stations. The first and second stations are instrumented with RPC's on both the interior and exterior, while the third and fourth stations are instrumented only on the interior. The read-out strips in the barrel chambers run parallel to the beam axis and are about 2.5 in length. Each endcap is equipped with three RPC stations (spanning longitudinally) and two to three rings (spanning radially). The first RPC station is instrumented on the exterior of $ME \pm 1/2$ and $ME \pm 2/3$, while the second station is installed interior to $ME \pm 2/1$ and $ME \pm 2/2$, and the third station is installed exterior to $ME \pm 3/1$ and $ME \pm 3/2$. The double gaps of the endcap RPC's have a trapezoidal geometry.

The two main roles of the RPC system are to aid in muon triggering and to accurately assign the bunch crossing number. As was discussed in the beginning of this chapter, particles from multiple bunch-crossings, and hence primary collisions, are propagating through different parts of the CMS detector at any given moment in time. It is crucial that the signatures from these particles are appropriately assigned to the correct collisions. For the case of muons, this is ensured to a great extent by the RPC's.

5.2.6 Trigger System

The LHC can cross bunches at a frequency of 40 MHz. Separated by 25 ns in time, each bunch crossing, which can in principle yield up to 20 proton-proton collisions,

offers the CMS detector an opportunity to read-out and record data[1] . If all of the

zero-suppressed data from the millions of electronic channels in the detector were

to be read out for a single bunch-crossing (with 20 collisions), it would yield about 1

Mbyte. By multiplying this figure by the bunch crossing frequency, one could easily

conclude that it is not only impractical, but technologically prohibitive, to stream and

store such vast amounts of data at such high rates. Furthermore, the vast majority of

these collisions will involve relatively mundane and uninteresting physics processes,

such as minimum-bias QCD (e.g., light quark-antiquark production). The production

of top-quarks, which is an interesting process, will occur on the order of a few Hz, for

example. Exotic and hypothetical physics processes could occur even more rarely. Thus,

a dedicated trigger system is required to filter the collision events as they occur before

valuable resources are consumed to write them to tape for extensive analysis by the

collaboration. The trigger system constitutes the beginning of CMS event selection.

There are two stages of triggering, and hence two stages of event rate reduction,

on CMS. The first stage is called the *Level-1 Trigger* (L1), which is composed of

customized hardware and electronics for quick and efficient on-site processing of

the digitized data that is reported from various sub-detectors. The second stage is

called the *High-Level Trigger* (HLT), which consists of a filter farm of about a thousand

commercial processors. The L1 is hardware-based, while the HLT is software-oriented.

The combined L1+HLT system is designed to reduce the event rate via the following

sequence: LHC (40 MHz) $\rightarrow$ L1 (100 kHz) $\rightarrow$ HLT (300 Hz) $\rightarrow$ storage. Thus, the rate is

ultimately reduced by roughly 5 orders of magnitude.

The L1 trigger system makes accept/reject decisions per bunch-crossing based on

very coarse data. The coarseness of the data is due to the 3.2μs time scale over which

---

[1] In reality, not every bucket is filled with a proton bunch. Even at nominal luminosity, $2,808$ of $3,564$ buckets will be filled.

the L1 has to process and judge an event. The high-resolution version of the data is buffered in the onboard front-end electronics of the sub-detectors until the L1 "accepts" the event, at which point, the finer data is then transferred downstream to the HLT, where more sophisticated and refined event analysis can take place.

Three main components or tiers constitute the L1 trigger system: local, regional, and global. The local component builds what are called *trigger primitives*, which can be understood as the quanta of the entire trigger system. Trigger primitives are crude blocks of data, which reflect very basic quantities reported from the calorimeter systems (e.g., energy deposited in the calotowers) and the muon system (e.g., track segments, hit patterns). The regional tier of the L1 trigger system performs a synthesis of the information provided by the trigger primitives and ranks them according to some predetermined criteria. Ranking can be based on the quality of the measurement represented by the trigger primitive. Also, some trigger primitives can be judged to have more upside or potential to reflect interesting physics than others. The global tier of the L1 receives the ranked information and executes some quick algorithms to determine if the event should be accepted at this stage and propagated to the HLT. If the L1 accepts the event, then the higher resolution detector data is read out and sent to the HLT filter farm for a more thorough scrutiny.

Aside from the content of the trigger primitive information, the global L1 decision can be contingent on the status of the sub-detectors and the Data Acquisition System (DAQ). The LHC will deliver about 128 bunch crossings in the 3.2μs of time it takes the L1 to render its decision. This latency has a few consequences. In order to prevent buffer overflows, a few *trigger rules* are imposed. No more than $1 : 2 : 3 : 4$ events from the L1 trigger can be accepted per $75 : 625 : 2500 : 6000$ ns. This results in a small dead time ($\approx 1\%$) where the LHC is delivering luminosity (and hence collisions) but the CMS detector cannot record the data. More details related to the L1 triggers for the calorimeter and muon systems can be found in Ref. [38]

The HLT operates with a latency of 0.02 to 1 seconds and is only meant to perform a more refined analysis on the L1-seeded objects. The L1 trigger will provide the HLT with muon, electron, photon, and jet candidates, as well as a few other coarsely calculated quantities (e.g., $\not{E}_T$, H_T). To assess the attributes of some of these objects, data from the inner tracking system needs to be unpacked. It is a time consuming process to read out the data from the millions of channels in the Tracker, which is why the current CMS L1 trigger is blind to what occurs in the Tracker. Even with the extra time afforded to the HLT, only regional track reconstruction can be performed in the vicinity of the L1 objects. Aside from this exception, the full event reconstruction-level information is performed and is available to the filtering algorithms which run at the HLT. The details of CMS event reconstruction will be discussed in the subsequent section.

The performance of the CMS trigger system is not solely evaluated by its rate reduction. Like any event selection filter, the trigger system will lose (or fail to accept) events which it is meant to accept. The frequency with which an event selection filter succeeds in accepting an event when it is supposed to is known as the signal efficiency. Ideally, for a robust filter, the signal efficiency should be almost always 100%; however, in the case of triggers this is not in general true (depending on the definition of the signal). For example, a muon with a true value of $p_T = 10$ GeV may be actually construed by the L1 trigger as a muon candidate with $p_T = 6$ GeV due to the coarseness of the data. If the L1 trigger filter only accepts events with a muon candidate of $p_T > 8$ GeV, then this event will be rejected, and an inefficiency would result. At the HLT where the data is finer and the filtering algorithms can afford to be more complicated, there could be any number of causes for events be mistakenly rejected (e.g., event mis-reconstruction, software bug, etc.). Thus, a significant amount of effort is involved to understand, commission, and validate the trigger filters. This can be done to a certain extent with the help of simulation, but to be done rigorously necessitates the analysis of real collision data.

5.3 Event Reconstruction and Data Analysis

Once an event has been accepted by the HLT, the detector data corresponding to the event is then written to tape in raw form, promptly reconstructed at CERN, and then distributed to various sites for analysis. This process involves a number of intermediate steps as well as a substantial number of resources, which will be described in the subsequent subsections.

5.3.1 The CMS Software

The CMS Software (CMSSW) is a modular, object-oriented framework which allows users and physics groups to do the following, among many other things:

- Design and apply filtering algorithms for the HLT

- Simulate, reconstruct, analyze, and visualize events

- Apply calibration and alignment corrections to the data recorded by the detector

- Perform various tasks related to Data Quality Monitoring (DQM)

Many of the utilities within CMSSW are provided by the ROOT data analysis framework. Developed by computer scientists at CERN, ROOT is an object-oriented collection of libraries and classes which contain much of the functionality needed to handle, manipulate, and analyze large amounts of data [54]. Experiments across the world employ ROOT for this purpose. Data from CMS is stored in ROOT files, and the information contained in these files is formatted in accordance with the CMS Event Data Model (EDM). The foundation of the EDM is the *event*, which is a C++ container class used to store all raw and reconstructed data related to a particular bunch-crossing (or collision). Within CMSSW each event container is sequentially filled with various objects, which represent the information recorded by the detector.

As alluded to earlier, data can exists in several forms within the EDM format. The most fundamental form is the raw data (RAW), which mainly consists of the digitizations of the front-end electronic signals registered by the millions of channels in the various CMS sub-detectors. The RAW data is not usable for analysis. It has to be *unpacked*

and *reconstructed* first, which is another way of saying *reformatted* and *synthesized*. The CMS event reconstruction consists of hundreds of algorithms which are developed and executed in several stages within the CMSSW environment. In simplest terms, the unpacked data undergoes local detector reconstruction, which is followed by physics object reconstruction and finally high-level reconstruction. The local reconstruction algorithms are executed first and these produce C++ objects which contain information about lower level objects, such as the single and collective position measurements in the tracking and muons systems, as well as energy clusters in the ECAL and HCAL. These lower level objects are often referred to as reconstructed hits or *RecHits* for short, and they serve as inputs to the physics object reconstruction algorithms where they are synthesized into collections of tracks, muons, electrons, photons, and jets. The RecHits and physics objects combine to provide building blocks for even higher level reconstructed objects, which include vertexing, b-tagging, τ identification, particle flow, and the calculation of $\not{E}_T$-related quantities, to name a few. For the majority of the 2010 collision runs, the time required to process an event through the full reconstruction chain ranged from 1 to 2 seconds on average, but can be a factor of 10 higher in rare cases [55].

In general, a standard EDM ROOT file will contain any or all of the following levels of data:

- **RAW level**: Contains raw detector information from the front-end electronics.

- **RECO level**: Contains detailed information about the reconstructed physics objects (e.g., jets, electrons, photons, muons) as well as the constituent information which is use to build these objects (e.g., tracks, rechits, calotowers). Contains more than sufficient information for analysis, and is bulky as a result, consuming ≈ 350 kB/event. It is not optimal for frequent analysis.

- **AOD level**: The Analysis Object Data contains only the subset of RECO level information which is essential for analysis. The event size is smaller ≈ 100 kB/event, which enhances the processing rate, and conserves much less disk space.

Even though the CMS trigger system reduces the recorded event rate to a manageable 300 events per second, the LHC will run for years. It produced proton collisions for over 800 hours during 2010. Thus, vast amounts of data storage resources are needed to accommodate the billions of recorded collision events for analysis. To this end, it is essential that the data files are kept as lean as possible, without compromising the users' analysis goals. This is what the AOD is meant to do.

5.3.2 Grid Computing

At nominal operating conditions the LHC will produce approximately 13 million Gigabytes of data per year [56]. The worldwide LHC Computing Grid (WLCG) is an extensive global collaboration established to manage this vast amount of data that will be produced by the LHC. The Grid is an enormous entity, spanning dozens of countries, composed of over a hundred computing centers, contributing hundreds of thousands of processors. Unlike the experiments of previous generations, most of the data analysis will not actually take place on-site where the experiments are located at CERN. It will be done remotely at various universities and laboratories around the world by means of the Grid.

The distribution of data across the grid is done in a few stages and involves a hierarchy of computing centers. Different levels in this hierarchy are called *tiers*, which reflect the amount of CPU and storage resources an institution is able to provide. The roles of the various tiers as they relate to the CMS experiment, can be summarized as follows:

Tier-0 (CERN):

- Receives RAW data from the CMS Online Data Acquisition and Trigger System

- Segregates RAW data into what are called Primary Datasets (PD) based on which type of trigger filters accepted the event (e.g., Muon PD, Electron PD, $\not{E}_T$ PD)

- Archives one copy of each RAW PD to tape

- Distributes a second copy of the RAW PD to a Tier-1 center

- Executes prompt calibration algorithms, which extract the calibration and alignment constants necessary to perform reconstruction on the data

- Executes prompt reconstruction of RAW data yielding RECO versions of PDs.

- Distributes RECO version of PDs to the Tier-1 center containing the second copy of the RAW version

- Extracts AOD version of PDs from RECO version and distributes AOD to all Tier-1 centers

Tier-1 (7 national laboratories)

- Receives a subset of RAW, RECO, and AOD data from Tier-0

- Performs scheduled re-reconstruction and skimming of PDs

- Distributes RECO and AOD versions of PDs to Tier-2 centers

- Stores Monte-Carlo–simulated datasets produced by Tier-2 centers

Tier-2 (dozens of universities):

- Stores RECO and AOD versions of full PDs and skimmed PDs

- Provides GRID-based analysis for users across the entire collaboration

- Produces, stores, and distributes Monte-Carlo–simulated data

A typical CMS-based analysis on the Grid would begin with a user writing a CMSSW executable analysis program or algorithm on his or her personal computer. The user would then connect to the Grid via a shared network from a Tier-0, Tier-1, or Tier-2 institution. The Grid would receive the user's executable program as well as some parameters relevant to the desired PD to be analyzed. After locating the PD at a few Tier-2 centers, for example, and assessing the available resources (CPU, storage, etc), the Grid would create jobs that will execute the algorithms in a parallel fashion over the data. The user can monitor the actions of the Grid as well as the progress of his or her jobs. When the jobs are finished, the user executes some retrieval commands and the outputs of the algorithms (typically ROOT files containing histograms) are delivered. With the combined resources of the Grid, a collision event can occur at the LHC, be

recorded by the CMS detector, and be distributed to the various Tier-1 and Tier-2 sites in AOD format for users to analyze in the period of roughly 48 hours. For high-priority, low-latency analysis work, resources do exist on-site at CERN (Tier-0), but the majority of analysis is conducted over the Grid.

5.3.3 Monte Carlo Simulation

The role of simulation in collider physics experiments cannot be overstated. It is essential to every aspect of operation on CMS, including detector design and calibration, trigger emulation, machine-induced and cosmic-ray background studies, and reconstruction performance, to name a few. Perhaps, the most valuable service offered by Monte Carlo simulations at this stage of the experiment is the high-statistics training ground it provides for physicists to explore and optimize search strategies for varieties of new physics models. With the help of simulation, the expected background and signal yields, and hence discovery potential, of a new physics search (e.g. supersymmetry via same-sign di-leptons) can be evaluated. If a particular search strategy is not feasible according to Monte Carlo simulations (e.g. backgrounds are too high), then it is very unlikely to be feasible with real data. The inverse of this statement is not guaranteed to be true, however, and this fact motivates a significant amount of effort related to so-called *data-driven* analysis methods (i.e., not Monte-Carlo–based). The discussion on data-driven methods will be deferred until Chapter 6.

The production of a Monte-Carlo–simulated event is factorized into a few stages. The first stage is performed by an *event generator* such as MadGraph [57] or Pythia [58]. These simulate the particle collisions that the LHC will copiously produce in real life. Despite taking place over sub-femtosecond time intervals, an LHC collision event has a rather complicated genesis and evolution, which the event generator must try to replicate correctly. The sequence of important processes is summarized succinctly in Ref. [58] and will only be briefly paraphrased here. In short, protons from the two LHC beams approach each other from opposite directions carrying the beam momentum. Protons

have substructure, i.e. quarks and gluons, and the behavior and characteristics of these need to be accurately simulated. This is done by parton distributions functions (*pdf*'s) which model the momentum phase space available to each species of parton. The interaction begins as one parton from each proton begins a branching sequence (e.g., $g \rightarrow gg$ or $q \rightarrow qg$) which rapidly breeds many more partons. Typically one parton from each of these showers is involved in a hard-scattering process that results in a number of outgoing partons (often two). The details of this hard-scattering process determine the outcome of the event. The creation of a short-lived resonance boson (e.g. Z^0 or $W^{\pm}$) may occur, which subsequently decays to leptons or other partons. The most likely interaction (i.e. highest cross-section) is a mundane QCD process where the incoming partons simply exchange a gluon, which results in a modest momentum transfer. While this is the most common, any interaction prescribed by the Standard Model will have some probability of occurrence for a given event.

Many generators stop once the outcome of the hard-scatter is simulated, and simply provide a list of the few particles which result along with their respective 4-momenta, etc. The evolution of the event is nonetheless still incomplete at this stage. Any outgoing partons from the hard-scatter could also undergo a branching sequence similar to the incoming partons. This is known as final state radiation (FSR). Some types of large-angle (hard) FSR can be calculated by the event generator; however, the soft, collinear FSR is more difficult to treat analytically and has to be modeled by parton shower programs (e.g., Pythia). Furthermore, the laws of QCD only allow for color-neutral final states (confinement), so each color-charged parton (i.e., individual quark and gluon) produced in the hard-scatter must be undergo a fragmentation and hadronization process. Some of the resulting groups of hadrons may be extremely short-lived and will decay immediately upon creation, and some could have lifetimes that allow them to traverse measurable distances in the laboratory frame before decaying (e.g. D and B mesons) or even interact with the detector (e.g. $\pi^{\pm}$, K_L^0, and $K^{\pm}$). All of

this has to be probabilistically simulated according to fragmentation and hadronization models, which are not well-known from first principles, but are often parameterized with data.

The final number of distinct particles involved in the hard scattering event from genesis to hadronization can be well over a thousand. Thus, there is an immense amount of detailed calculations and bookkeeping required for event generation and parton showering. The industry is rife with activity in order to better simulate hard collisions and better account for quantum effects. Some generators can account for quantum spin correlations, and some can feature events with up to 6 outgoing partons before hadronization (instead of 2), while others specialize in non-leading order contributions to the matrix element (scattering amplitude) for various processes. As a result, CMS employs a variety of event generators to accommodate its Monte Carlo needs.

While the creation of outgoing intermediate and final state particles resulting from the LHC collisions is under the purview of event generators, a different framework must take these particles and propagate them through the CMS detector, simulating interactions with the various mediums along the way. The is done by the GEANT4 simulation toolkit [59]. The entire CMS detector's geometry, it's material composition (active and passive), as well as its magnetic field map is implemented in the GEANT4 program. This allows for users to simulate how particles will behave while traversing the detector and how the detector will consequently perform measurements of such particles. GEANT4 attempts to model all known physics processes that are involved in the passage of particles through matter permeated by an intense magnetic field (e.g., ionization losses, bremsstrahlung, nuclear interactions, multiple particle scattering, electromagnetic/hadronic showering, photon conversions, etc.). The program simulates these processes for each generated particle and produces a simulated hit in the detector (SimHit) which is then used to simulate a front-end electronics signal (electronics noise

is emulated on top). The collection of the latter constitutes a simulated version of RAW data. This simulated RAW data is then processed by the reconstruction algorithms just as real RAW data would be.

All of these factorized steps from event generation to detector simulation and reconstruction occur within the CMSSW environment. The end result is the production of an EDM ROOT file which contains hundreds of simulated events with nearly the same file content as that of real collision data. An important difference between real data and simulated data is that with the latter, the user has access to the *Monte Carlo Truth* information, which allows him or her to identify certain signatures in the detector and attribute them to certain particles. This affords one the ability to perform a variety of reconstruction-level and trigger-level efficiency studies as well as assess the performance of various event selection requirements at the analysis level.

The utility of GEANT4 is limited by its per-event processing rate. It is quite CPU-intensive to faithfully simulate how each particle will interact with each cubic micron of detector material that it encounters along its way. To fully simulate a soft QCD interaction event (e.g. $\hat{p}_T > 15$ GeV), GEANT4 requires about 90 seconds of CPU time, with variations that are sensitive to the particle multiplicity of the event. Recall, that the LHC can manufacture a real QCD event every few nanoseconds at nominal operating conditions. Thus, parallel processing is a necessity for mass production of simulated data. Fortunately, such processing is easily facilitated by the Grid, and specifically the resources of the CMS Tier-2 centers.

Despite the advantages that the Grid provides, in order to simulate just 1 pb^{-1} worth of soft QCD data it would require over 800 million events, as the cross-section is over 8×10^8 pb at leading order for $\hat{p}_T > 15$ GeV. Considering that users generally want their Monte Carlo statistics to be commensurate with the integrated luminosity of real data they are analyzing, one immediately sees the limitations from employing a program like GEANT4 to simulate the detector's response. In 2010 the LHC delivered over 40 pb^{-1}

of data. This is expected to increase by roughly two orders of magnitude by the end of 2012. It is simply impossible to simulate that much QCD data with GEANT4, although processes with much smaller cross-sections (e.g. high-$\hat{p}_T$ QCD or electroweak) will not in general be limited by the large processing time.

An alternative to GEANT4 is the CMS Fast Simulation software (FastSim), which offers a parameterized treatment of the physics interactions that occur as particles propagate through matter. Depending on the type of collision event being simulated, FastSim can produce the event several hundred times faster than GEANT4 can, and with comparable accuracy for most of the observables users wish to study [60] . With the help of FastSim, high-statistics samples can be produced for any number of processes. One important use-case, which will be encountered in Chapter 6, is the mass production of simulated data for a multitude of new physics models within a vast parameter space (e.g. mSUGRA). These types of parameter space scans are useful in order to calculate statistical exclusion limits for new physics searches.

CHAPTER 6
THE SEARCH FOR SUPERSYMMETRY AT THE LHC WITH THE SAME-SIGN DI-LEPTONS, JETS, AND $\not{E}_T$ SIGNATURE

6.1 Introduction

The analysis described herein constitutes one of three major components of the first effort to identify supersymmetry at the LHC with the same-sign di-leptons, jets, and $\not{E}_T$ signature using the CMS detector. The main feature of this analysis that distinguishes it from the other components is the focus on final states with soft leptons (i.e., small transverse momenta or low-p_T), including the di-muon ($\mu\mu$), di-electron (ee), and electron-muon ($e\mu$) channels. The other two components focus on final-states with hard leptons (high-p_T) and final states with hadronically decaying tau-leptons (also called hadronic τ's), respectively. These three components have been synthesized into a common result, which is based on an integrated luminosity of 35 pb^{-1} and can be found elsewhere [61]. The following discussion will be restricted only to the component related to soft leptons.

Pairs of same-sign, prompt leptons (not arising from jets) are very rare in the Standard Model, Synchrotron but appear very naturally in many new physics scenarios [20, 23–25, 28–30]. This makes searches for new physics with same-sign di-lepton pairs very attractive. The *minimal* SUSY-inspired (but not limited to SUSY) prerequisites for the appearance of same-sign di-leptons, and the corresponding experimental consequences, are as follows:

- By default, we assume that the lightest supersymmetric particle (LSP) is stable (or semi-stable) and weakly interacting (e.g., $\tilde{\chi}_1^0$). From the phenomenological point of view, the LSP sets a new and hitherto unknown mass scale, m_C. The expectation of such an LSP makes $\not{E}_T$ a natural part of the experimental signature.

- Next, we assume that the prime production mechanism is via QCD processes, i.e. via production of gluinos and squarks, whose masses become the second mass scale m_A. This leads to large cross sections and thus detection in the early data a possibility. The experimental consequences are such that one should expect jets (in a cascade from a colored object to the LSP), which become a second ingredient in the analysis.

- Finally, we should assume a charged Electroweak (EWK) particle coupling to quarks and squarks and having a mass residing between the squarks and the LSP. In the context of SUSY, this particle would be a chargino. Such a mass hierarchy opens the possibility for a cascade decay chain which includes a single lepton (e.g., $\tilde{q} \to \tilde{\chi}^+ q \to l^+ \nu \tilde{\chi}_1^0 q$) and, consequently, allows for two same-sign leptons per event. The obvious phenomenological implication of inserting a chargino between squarks/gluinos and the LSP is that we have introduced yet another, third mass scale, m_B, with the overall order $m_A > m_B > m_C$.

- Note that the EWK production does not naturally lead to exclusive same-sign di-leptons; they would appear only as a part of tri- or quad-lepton final states, which are better searched for in dedicated analyses looking exclusively for 3 or more leptons. It is also worth mentioning that, should gluinos be very heavy, the dominant production mechanism would be via squark-antisquark pairs, which, as in the case of the EWK production, does not lead to exclusive same-sign di-leptons.

An example of a process giving the desired signature of two same-sign leptons with jets and $\not{E}_T$ was shown in Figure 3-5. Figure 6.1 shows the total next-to-leading order (NLO) and leading order (LO) cross-sections calculated with the Prospino [62] software for gluino-gluino, squark-squark and squark-gluino productions in pp collisions at $\sqrt{s} = 7$ TeV as a function of the gluino-squark mass ($M_{\tilde{g}} = M_{\tilde{q}}$ for $\tilde{q}\tilde{g}$ production).

The three mass scales inherent to the same-sign di-lepton signature define the experimental energy scales for hadronic activity, lepton momenta, and missing transverse energy in the final state.

- Jets appear in the first step of the two-step process: $\tilde{q} \to \tilde{\chi}^\pm q$ or $\tilde{g} \to \tilde{\chi}^\pm q\bar{q}$. Consequently, the number of hard jets per decay chain is one or two, while the mass splitting, Δm_{AB}, defines the total amount of the energy available to jets.

- Given that the chargino mass must be above 100 GeV and that squark/gluino masses above $400 - 500$ GeV would not be produced at the LHC with the data collected thus far, charginos appearing in the first cascade must likely have a very modest boost. Consequently, the p_T of leptons appearing in the second decay are good indicators of the second mass splitting Δm_{BC}.

- The magnitude of the $\not{E}_T$ will have some dependence on both mass splittings, but never becomes small as long as there is a large mass difference, Δm_{AC}, between squarks/gluinos and the LSP.
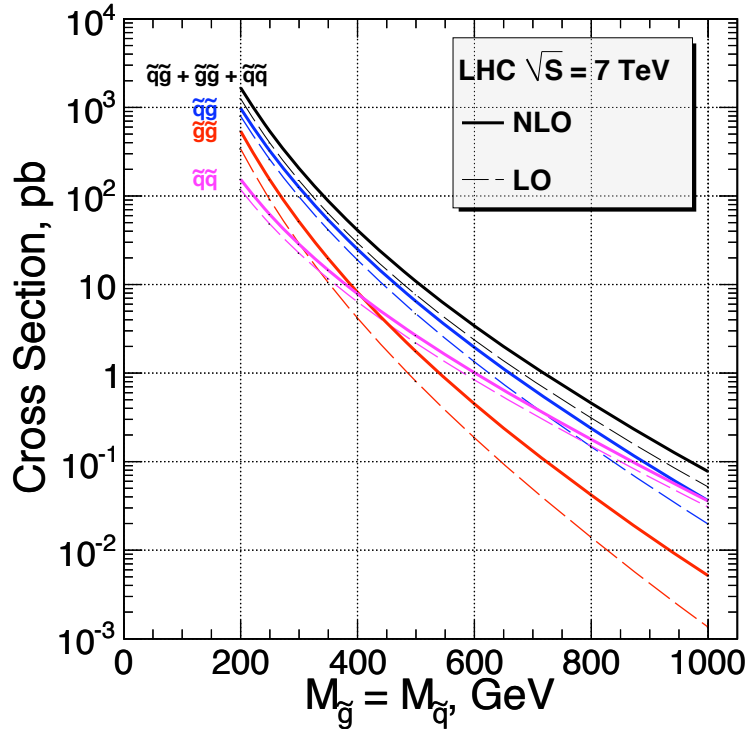
Figure 6-1. The total NLO (solid) and LO (dashed) cross-sections for gluino-gluino ($\tilde{g}\tilde{g}$), squark-squark ($\tilde{q}\tilde{q}$) and squark-gluino ($\tilde{q}\tilde{g}$) productions vs gluino or squark masses at the LHC ($\sqrt{s} = 7$ TeV).

6.2   Monte Carlo Simulated Data

For this analysis an assortment of simulated Standard Model Monte Carlo

data samples are used to study the performance of event selection criteria and to

validate background prediction methods. These samples rely on either Pythia [58]

or MadGraph [57] for event generation and GEANT4 [59] for simulation of the CMS

detector. To model the signal, a reference point from the mSUGRA parameter space is

used with parameters: $\mathbf{m}_{1/2}$= 160 GeV, $\mathbf{m}_0$= 200 GeV, $\tan(\beta) = 10$, $\mathbf{A}_0 = -400$ GeV,

$\mu > 0$. This model is commonly referred to as LM0 and features low-mass squarks and

gluinos. As a result of these low masses, the production cross-section is relatively high

(~ 57 pb), allowing for the possibility of discovery with the first 35 pb^{-1} of data, should

it exist. While it is beyond the exclusion reaches of the LEP and Tevatron searches,

it has recently been excluded at 95% CL by searches with the ATLAS [63] and CMS

detectors [64, 65], which were performed concurrently with this one. Despite this, LM0 still provides a useful model of the generic signal topology (i.e., same-sign di-leptons, jets, and missing energy), which can help to inspire several of the event selection criteria. All of the relevant backgrounds as well as LM0 are represented and detailed in Table 6-1. Leading order cross-sections are combined with k-factors, where the latter are available. All events from these samples are reconstructed with version 3.5.6 of the CMS SoftWare (CMSSW).

Table 6-1. Summary of simulated Standard Model backgrounds and signal samples

Process	Generator	σ (LO) (pb)	k-factor	Equivalent $\int L \, \mathrm{d}t$ (pb^{-1})
$b\bar{b} : H_T \in [100, 250]$ GeV	MadGraph	23820	-	21.4
$b\bar{b} : H_T \in [250, 500]$ GeV	MadGraph	7002	-	148.3
$b\bar{b} : H_T \in [500, 1000]$ GeV	MadGraph	172	-	6.14×10^3
$b\bar{b} : H_T \in [1000, \infty]$ GeV	MadGraph	2.4	-	1.22×10^5
QCD : $H_T \in [100, 250]$ GeV	MadGraph	7.0×10^6	-	1.5
QCD : $H_T \in [250, 500]$ GeV	MadGraph	1.71×5	-	28.7
QCD : $H_T \in [500, 1000]$ GeV	MadGraph	5200	-	805
QCD : $H_T \in [1000, \infty]$ GeV	MadGraph	83	-	2.00×10^3
$t\bar{t}$	MadGraph	95	1.66	9.35×10^3
single-t (s-channel)	MadGraph	4.21	-	9.79×10^4
single-t (t-channel)	MadGraph	64.6	-	8.18×10^3
single-t (tW-Channel)	MadGraph	10.6	-	4.40×10^4
γ+jets	MadGraph	173	-	6.28×10^3
W+jets	MadGraph	24200	1.2	322
Drell-Yan $\to \ell^+\ell^- : m_Z \in [50, 120]$ GeV	MadGraph	2400	1.17	356
Drell-Yan $\to \ell^+\ell^- : m_Z \in [20, 50]$ GeV	Pythia	4998	(NLO)	523
Drell-Yan $\to \ell^+\ell^- : m_Z \in [10, 20]$ GeV	Pythia	10371	(NLO)	278
W^+W^+	Pythia	0.188	-	5.3×10^4
W^-W^-	Pythia	0.064	-	2.9×10^5
$2 \times (qq' \to W^\pm)$	Pythia	0.203	-	2.2×10^5
ZZ	Pythia	4.3	1.37	2.0×10^4
$W^\pm Z$	Pythia	10.5	1.74	6.3×10^3
$W^\pm W^\pm$	Pythia	28	1.53	2.9×10^3
SUSY Model Point LM0	Pythia	38.9	1.48	3.6×10^3

6.3 Trigger Strategy

As the instantaneous luminosity delivered by the LHC increased over the 2010 data taking period, the CMS trigger menus were forced to evolve accordingly. For a search relying on high-H_T and low-P_T leptons, the trigger strategy becomes quite complicated, as trigger thresholds were frequently raised to accommodate the increasing collision rates. As a consequence, various trigger paths were explored for each channel in this analysis. Ultimately, the H_T-based trigger paths provided the best sensitivity, and so they are used here. Some complications arise from the fact that definition for H_T used online by the high-level trigger (HLT) is not the same definition used offline in the analysis. This is due to the limited and coarse information that is available to the HLT for such calculations. These complications simply force one to impose an event selection requirement on the H_T observable offline that is well above the one that is used online. This is done in order to ensure that the probability for an event with an offline value of H_T to satisfy the online H_T selection requirement will be greater than 95%. This probability is often referred to as the trigger efficiency, and is meant to be close to 100% in ideal cases. The H_T trigger efficiency can be measured by appealing to other orthogonal triggers. This measurement will be discussed in Section 6.7.2.5.

Table 6-2. Summary of trigger strategy

Run Range	$\int L\, dt$ (pb^{-1})	Trigger Requirement
140160-147116	7.4	Online $H_T > 100$ GeV
147196-148058	9.5	Online $H_T > 140$ GeV
148822-149294	17.8	Online $H_T > 150$ GeV

6.4 Physics Objects and Discriminating Observables

The main physics objects employed by this analysis are muons, electrons, jets, and missing transverse energy. All of them are reconstructed using standard techniques on CMS [38].

Muons are required to be reconstructed using two algorithms [66]. One algorithm, called the Tracker Muon reconstruction algorithm, matches tracks in the silicon detector

with measured hits in the muon system. Another algorithm, known as the Global Muon reconstruction algorithm, performs a simultaneous global track fit using measurements from both the silicon detector and the muon system. Tracks belonging to the muon candidate must have a minimum number of 11 hits in the silicon tracker, at least 1 hit in the muon system, and have a high-quality global track fit with a normalized χ^2 value of less than 10. The calorimeter signal which lies in the trajectory of the muon candidate must be consistent with that of a minimum ionizing particle.

Electrons are reconstructed beginning with an energy cluster located in the ECAL. The cluster is then matched to hits in the silicon detector. Owing to the high possibility for other objects (e.g., photons, jets) to mimic the characteristic signatures of electron candidates, a collection of dedicated electron identification variables are employed to further establish the existence of a true electron. These variables have been optimized using $W \rightarrow e\nu$ events, and can take on a variety of values in order to allow the user to choose the desired balance between reconstruction efficiency and purity of electrons [67]. For this analysis the identification criteria are chosen at a value that ensures that approximately 80% of true electrons are reconstructed, while the mis-reconstruction of other objects as electrons are greatly diminished. This identification criteria is often referred to as VBTF80.[1]

Muons are able to be reconstructed and well-measured down to $p_T > 5$ GeV, while electrons must be selected with a higher transverse momentum of $p_T > 10$ GeV. Both muons and electrons are measured up to a pseudorapidity of $|\eta| > 2.4$, and are required to originate from the primary collision vertex. In order to select leptons from so-called *prompt* electroweak decays (e.g., from $W^\pm$, Z, χ^0, $\chi^\pm$ particles) and not from hadronic decays or jets, a very important discriminating variable is employed, known as *relative isolation*, which is often abbreviated as RelIso . The RelIso observable is calculated by

---

[1] Vector-Boson Task Force working point 80%.

first forming a cone in $\eta - \phi$ space of radius $R = \sqrt{\Delta\eta^2 + \Delta\phi^2} = 0.3$ centered around the lepton candidate. Then the sum of the transverse components of all the tracks, ECAL transverse energy deposits, and HCAL transverse energy deposits, which lie in this cone, is divided by the transverse momentum of the lepton[2] . Figure 6.4 provides a pictorial representation of how RelIso is constructed. Algebraically, the expression for RelIso is given in Eq. 6–1. For this analysis, a requirement of RelIso < 0.15 is imposed on all leptons. A requirement is also made on the transverse impact parameter (Figure 5-3) of leptons as measured from the beamspot at a value of $d_0 < 0.2$ mm. This helps to ensure that the leptons do not come from decays of long-lived, heavy-flavor mesons.

$$\text{RelIso} = \frac{\sum_i p_{T,i}^{\text{Track}} + \sum_i E_{T,i}^{\text{ECAL}} + \sum_i E_{T,i}^{\text{HCAL}}}{p_T^\ell} \tag{6–1}$$

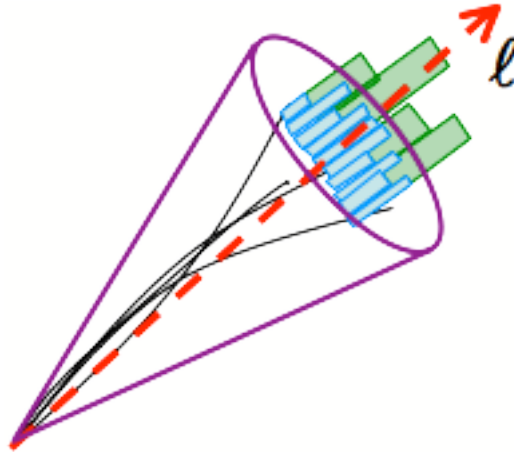Figure 6-2. Pictorial representation of how the RelIso variable is calculated.

---

[2] A small cone of radius $R = \sqrt{\Delta\eta^2 + \Delta\phi^2} = 0.01$ surrounding a muon candidate is removed from the isolation sum, in order to prohibit the muon's own p_T and energy deposit from contributing. For electrons, a more complicated geometrical shape is removed in order to prohibit contributions from bremsstrahlung.

Jets and $\not{E}_T$ are reconstructed based on the particle-flow technique [68, 69].
The anti-K$_T$ algorithm is used for clustering hadronic jets with a distance parameter
of $R = 0.5$ [70]. Jets are required to pass standard quality requirements in order to
reduce the effect of falsely reconstructed jets from calorimeter noise or other spurious
signals [71]. Jet energies are calibrated to compensate for the nonlinearity of the
calorimeter response [72]. Selected jets must have $p_T > 30$ GeV and be within $|\eta| < 2.5$.
The H_T observable is used to characterize the total amount of hadronic jet activity in the
event. It consists of the scalar sum of transverse momenta from all selected jets in the
event. At least two jets must be used in the calculation of H_T.

6.5 Event Selection

After satisfying the trigger requirements, the event is checked to ensure that a
good primary vertex is reconstructed with $|\Delta Z| < 15.0$ cm, $N_{dof} > 3$ and $d_0 < 2.0$ cm.
Further event selection is done in three stages: *pre-selection*, *baseline selection*, and
final selection. Each subsequent stage imposes stricter requirements than the previous
stage. The pre-selection requirements are meant to provide a relatively high-statistics
sample that can be used for direct comparisons with Monte Carlo simulated data.
The baseline selection is used as a control region for predicting a sub-dominant, but
important, background from QCD multi-jet production. The final selection represents all
of the selection requirements that are used for the counting experiment (i.e., the signal
search). The details of these selection stages are provided in Table 6-3.

Additional leptons are also allowed to be present in the event. In the case that
there are multiple pairs of same-sign leptons in the event, priority is assigned by $\mu\mu$, $e\mu$,
and lastly ee. If there are multiple pairs within the same channel, then the pair with the
highest scalar sum of p_T is chosen.

Tables 6-4, 6-5 and 6-6 show the event yields as the event selection requirements
are applied in succession, starting from preselection, for various simulated Standard
Model processes, the LM0 signal model, and data. Distributions of the H_T, RelIso

Table 6-3. Description of event selection requirements

Selection Level	Requirement	Description
Pre-selection	$N_{\mathrm{jets}} \geq 2$	Colored production
	$H_T > 100$ GeV	Minimal hadronic activity necessary
		for meaningful Monte Carlo comparisons
	$N_\mu \geq 2$ or $N_e \geq 2$	Di-lepton (or multi-lepton) event
	or $N_\mu + N_e \geq 2$	
	$q_{\ell_1} = q_{\ell_2}$	Same-sign electromagnetic charge
	$M_{\ell_1,\ell_2} > 5$ GeV	Invariant mass above
		characteristic heavy-flavor decay
	$M_{\ell_i^+,\ell_j^-} \notin [76, 106]$ GeV	Neither lepton should come
		from a Z-boson decay
Baseline selection	$H_T > 300$ GeV	Significant hadronic activity indicative
		of decay of heavy, colored superpartners.
		Also necessary for consistency w/ trigger.
Final selection	$\mathrm{RelIso} < 0.15$	Leptons must be isolated,
		indicating they are prompt
	$\not{E}_T > 30$ GeV	Non-trivial momentum imbalance,
		indicating the escape of invisible particles

of the most and least isolated leptons respectively, and $\not{E}_T$ after each subsequent selection requirement are shown in Figures 6-5, 6-6 and 6-7 for the $\mu\mu$-, ee-, and $e\mu$-channels, respectively. Preselection is represented by the first row. Baseline selection is represented by the second row. The third and fourth rows include the RelIso requirements on the most and least isolated leptons, respectively. The final row further includes the $\not{E}_T$ requirement and represents the yields after the final selection.

A graphical representation of the expected event yields from simulated Standard Model processes after the final event selection as described above is shown in Figure 6-4 for 35 pb^{-1}. The dominant backgrounds are single-top and top-antitop pair production ($t\bar{t}$). Due to the extremely high production cross-section of QCD multi-jet processes, the limited statistics from Monte Carlo simulations cannot be

used to evaluate this background. While it is expected to be sub-dominant or small, the contribution of this background must be accounted for and derived from data.
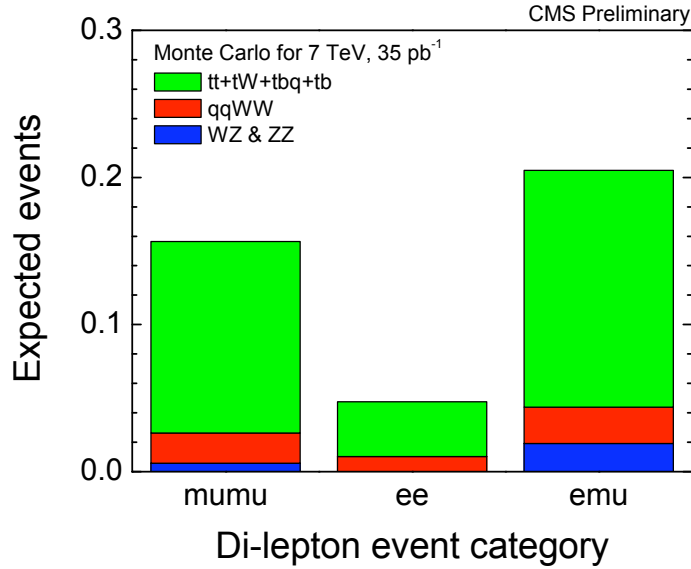
Figure 6-3. Monte Carlo predictions for expected event yields with 35 pb^{-1} of data.

Figure 6-4. Legend for Figures 6-5, 6-6, and 6-7.
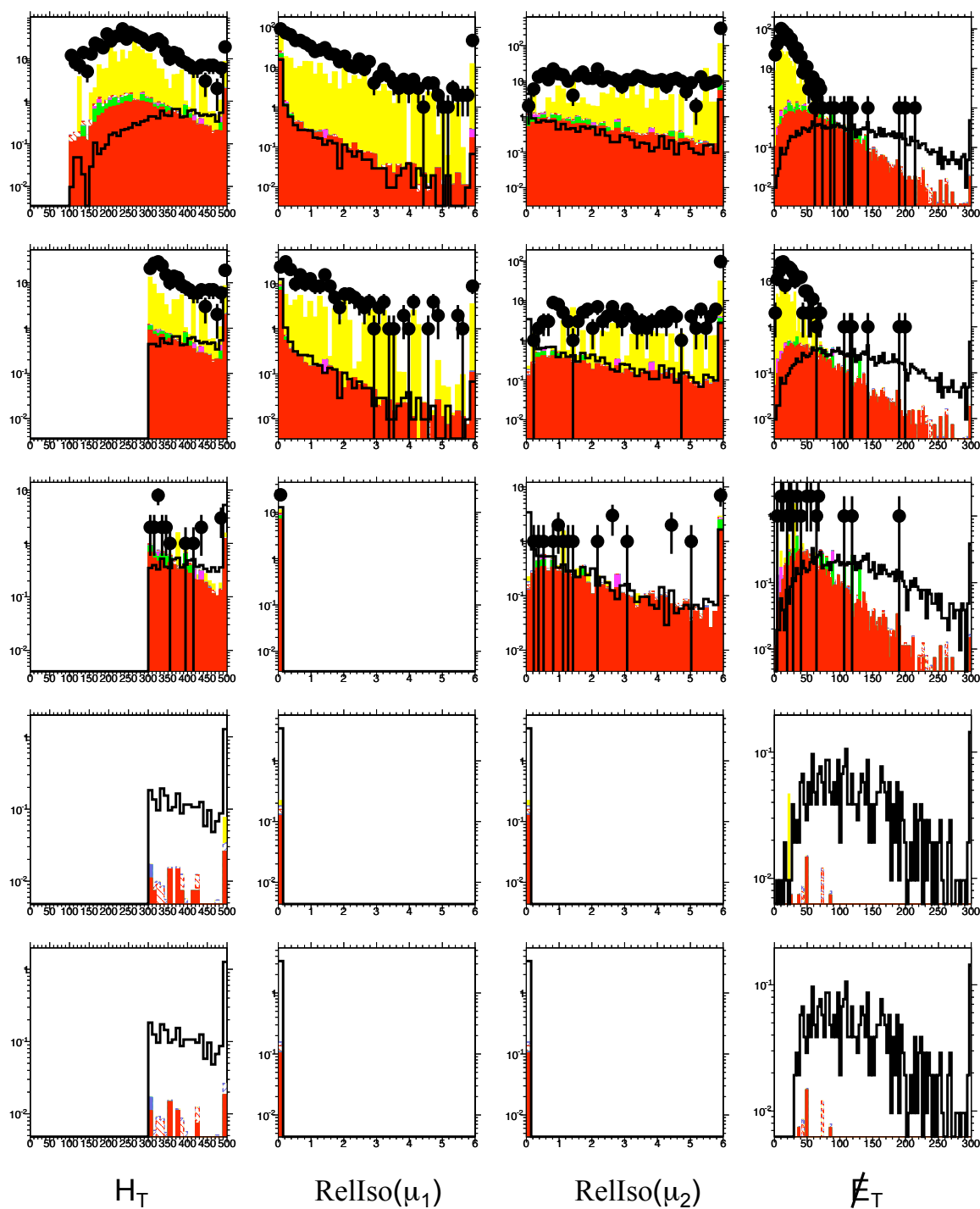
Figure 6-5. Distributions of key observables for the $\mu\mu$-channel. From left to right: H_T, $\mathrm{RelIso}(\mu_1)$, $\mathrm{RelIso}(\mu_2)$, and $\not{E}_T$. The rows from top to bottom represent successive event selection requirements: preselection, baseline selection, $\mathrm{RelIso}(\mu_1) < 0.15$, $\mathrm{RelIso}(\mu_2) < 0.15$, $\not{E}_T > 30$ GeV.
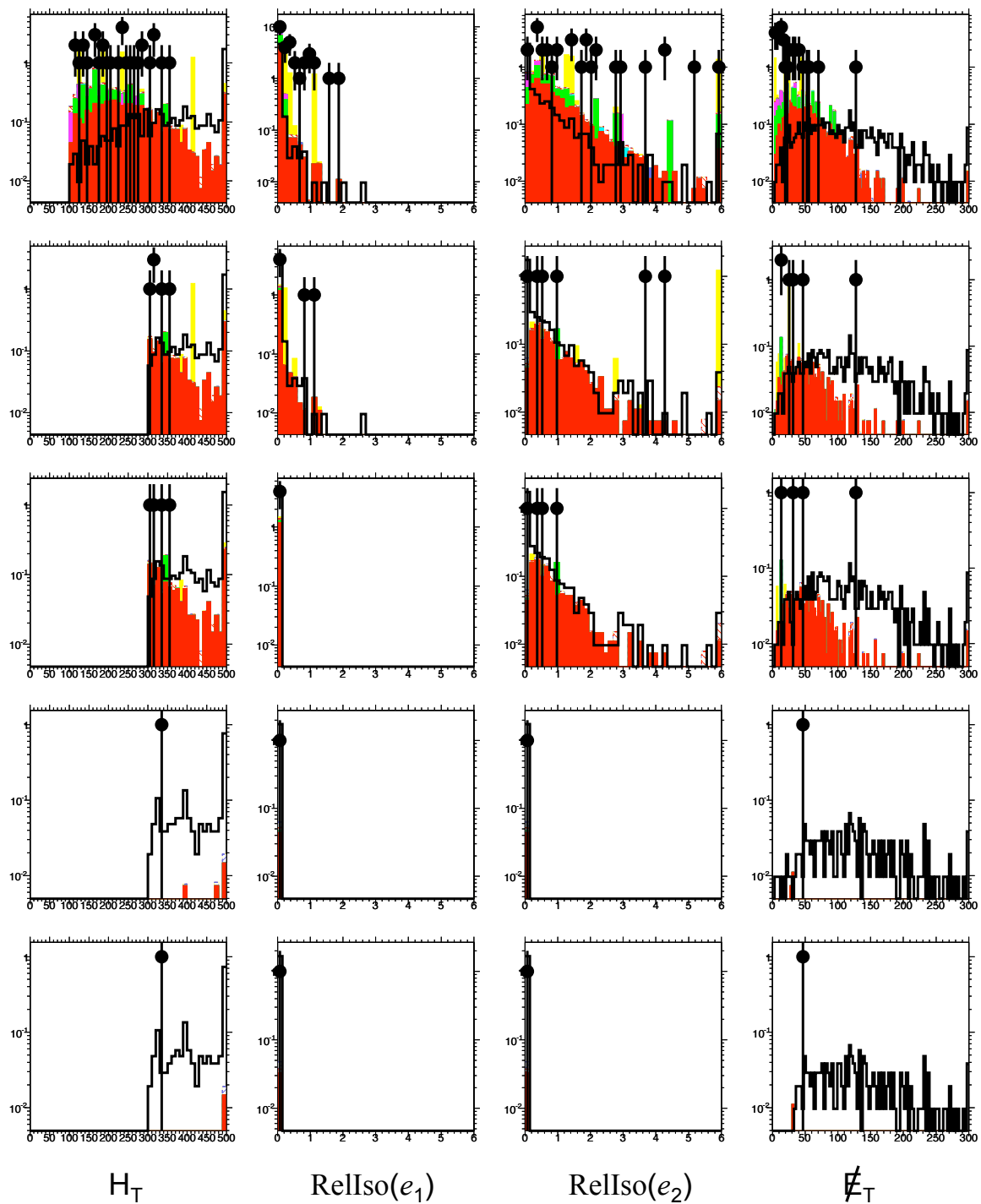
Figure 6-6. Distributions of key observables for the *ee*-channel. From left to right: distributions of H_T, $\mathrm{RelIso}(e_1)$, $\mathrm{RelIso}(e_2)$, and $\not{E}_T$. The rows from top to bottom represent successive event selection requirements: preselection, baseline selection, $\mathrm{RelIso}(e_1) < 0.15$, $\mathrm{RelIso}(e_2) < 0.15$, $\not{E}_T > 30$ GeV.

Figure 6-7. Distributions of key observables for the $e\mu$-channel. From left to right: distributions of H_T, $\mathrm{RelIso}(\ell_1)$, $\mathrm{RelIso}(\ell_2)$, and $\not{E}_T$. The rows from top to bottom represent successive event selection requirements: preselection, baseline selection, $\mathrm{RelIso}(\ell_1) < 0.15$, $\mathrm{RelIso}(\ell_2) < 0.15$, $\not{E}_T > 30$ GeV.

Table 6-4. Event yields after each cut for the $\mu\mu$-channel for 35 pb^{-1}.

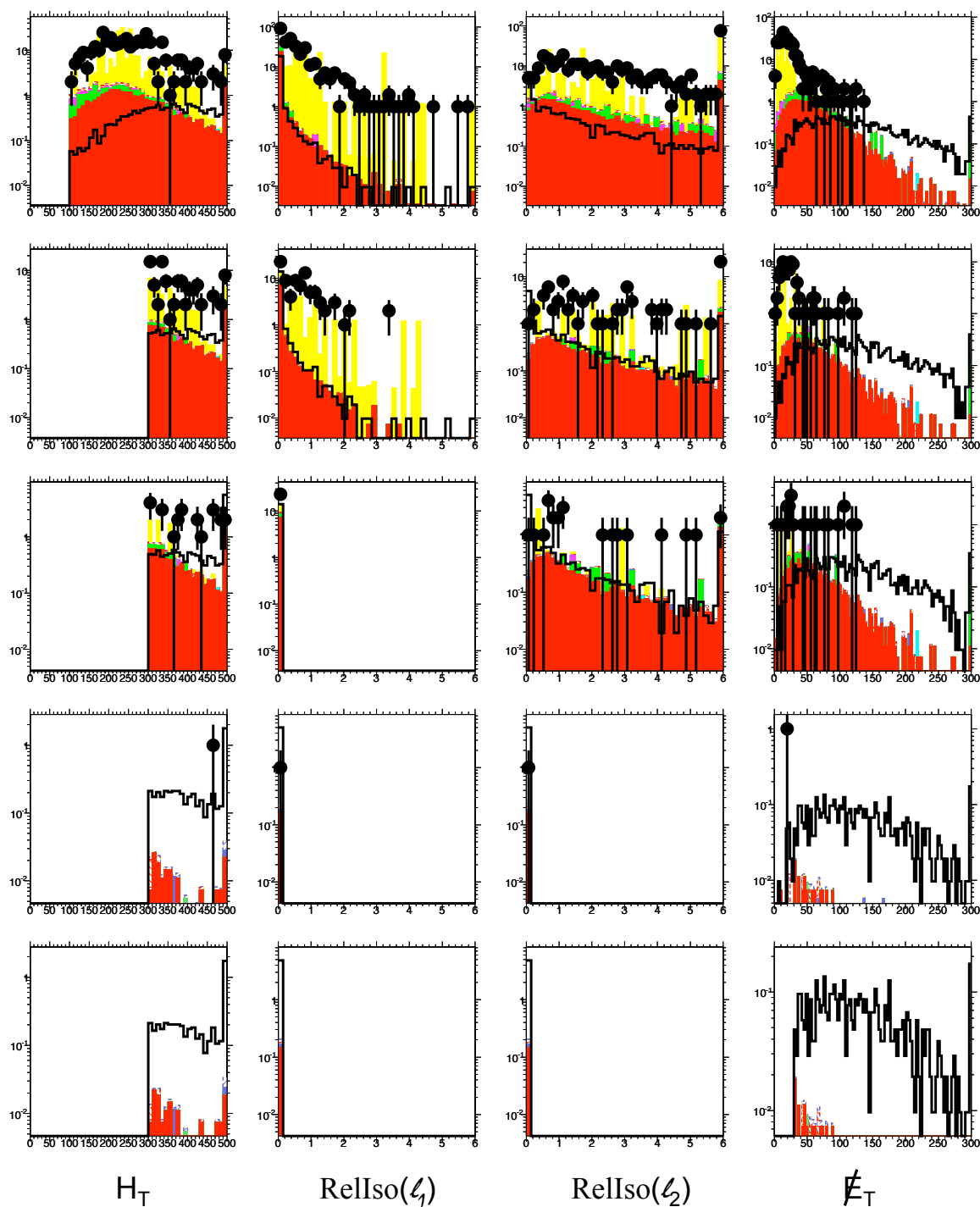| Cut Level	LM0	Data	Tot Bgd	$t\bar{t}$	W+jets	Z+jets	WZ	$W^\pm W^\mp$	ZZ	tW	single-t	$W^\pm W^\pm$	$2x(qq' \to W)$	QCD
Pre-selection	20	685	277	22.3	4.88	0.995	0.0807	0.0364	0.0142	0.531	2.46	0.0594	0.000638	245
Baseline	17.1	223	79.6	10.6	1.41	0.39	0.0346	0.0121	0	0.185	0.653	0.0312	0	66.3
RelIso(μ_1)	12.9	22	11.4	7.22	1.3	0.292	0.0288	0	0	0.117	0.537	0.0307	0	1.9
RelIso(μ_2)	3.42	0	0.224	0.125	0	0	0.00576	0	0	0.00272	0.025	0.0222	0	0.043
$\not{E}_T$	3.32	0	0.157	0.103	0	0	0.00576	0	0	0.00204	0.025	0.0206	0	0

Table 6-5. Event yields after each cut for the ee-channel for 35 pb^{-1}.

Cut Level	LM0	Data	Tot Bgd	$t\bar{t}$	W+jets	Z+jets	WZ	$W^\pm W^\mp$	ZZ	tW	single-t	$W^\pm W^\pm$	$2x(qq' \to W)$	QCD
Pre-selection	5.04	30	13.6	4.93	2.28	0.542	0.0231	0.0364	0.0177	0.152	0.491	0.0347	0.000159	5.06
Baseline	3.82	6	3.04	1.44	0.108	0	0	0	0.00355	0.0163	0.0749	0.0136	0	1.39
RelIso(e_1)	3.46	4	1.51	1.21	0.108	0	0	0	0.00355	0.0122	0.0749	0.0136	0	0.0859
RelIso(e_2)	1.74	1	0.0629	0.0442	0	0	0	0	0.00355	0	0.00416	0.011	0	0
$\not{E}_T$	1.67	1	0.0476	0.0332	0	0	0	0	0	0	0.00416	0.0102	0	0

Table 6-6. Event yields after each cut for the $e\mu$-channel for 35 pb^{-1}.

Cut Tot	LM0	Data	Tot Bgd	$t\bar{t}$	W+jets	Z+jets	WZ	$W^\pm W^\mp$	ZZ	tW	single-t	$W^\pm W^\pm$	$2x(qq' \to W)$	QCD
Pre-selection	21.4	324	234	27.4	6.72	1.97	0.161	0.0607	0.0444	0.875	3.32	0.0912	0.000638	193
Baseline	16.8	78	41.4	9.1	1.19	0.152	0.0519	0.0243	0.0071	0.143	0.562	0.0391	0	30.1
RelIso(ℓ_1)	14.5	21	13.5	7.36	1.19	0.125	0.0461	0.0243	0.00355	0.119	0.487	0.0381	0	4.11
RelIso(ℓ_1)	5	1	0.235	0.166	0	0	0.0173	0	0.00177	0.00136	0.0208	0.028	0	0
$\not{E}_T$	4.86	0	0.205	0.147	0	0	0.0173	0	0.00177	0.00136	0.0125	0.0248	0	0

6.6   Background Evaluation and Associated Uncertainties

In this section the best estimates of the background event rates with the associated systematic uncertainties are given. The Standard Model processes leading to prompt, same-sign di-lepton pairs have very small cross-sections. Hence, the main backgrounds associated with this analysis come with so-called "fake" leptons (e.g., non-prompt leptons passing tight isolation cuts, prompt leptons mis-reconstructed with the wrong charge, etc.) One cannot really expect that the Monte Carlo simulation would accurately predict rates of such "fake" leptons. Thus, this analysis largely relies on measuring the dominant and least certain backgrounds directly from data, which reflects the organization of this section. Background predictions, which are derived from the data itself are usually referred to as *data-driven*, while background predictions that come from simulations are referred to as *Monte-Carlo–based*. This terminology will be used throughout the remainder of this chapter.

Before going further it should be noted that the respective data-driven methods of background estimation do not necessarily map one-to-one onto distinct physics processes. In some cases, one method may cover more than just one background. For example, all processes with a single prompt lepton combined with another coming from a jet (e.g., $t\bar{t}$, tW, W+jets, Z+jets) are evaluated together by the same method. In other cases a single physics process can lead to more then one distinct way of entering the signal region. For example, $t\bar{t}$ can come via its prompt-fake component ($t\bar{t} \rightarrow (\ell\nu b)(jj\bar{b})$, b-jet $\rightarrow \mu + X$) or via the prompt-prompt component ($t\bar{t} \rightarrow (\ell^+\nu\bar{b})(\ell^-\nu b)$, where one of the two prompt leptons is mis-reconstructed with the wrong charge.)

The categorization of the main backgrounds to this search is summarized in Table 6-7. The notation introduced in this table may be referenced in other parts of this chapter. Any generic non-prompt lepton will henceforth be referred to as a "fake" lepton.

Table 6-7. Summary of backgrounds to the same-sign di-lepton search.

Background Type	Sources	Method
Same-sign prompt-prompt (N_{p-p}^{SS})	WZ, ZZ, $W^\pm W^\pm$	Monte-Carlo–based
Opposite-sign prompt-prompt (N_{p-p}^{OS})	Charge-flip in	Data-driven
	$t\bar{t}$, tW, DY, $W^\pm W^\mp$, etc	(Charge-flip method)
Same-sign prompt-fake (N_{p-f}^{SS})	$t\bar{t}$, tW, W+jets, Z+jets	Data-driven
		(BTag & Probe method)
Same-sign fake-fake (N_{f-f}^{SS})	QCD, all-hadronic $t\bar{t}$	Data-driven
		(Factorization method)

Equation 6–2 provides the calculation for the total background prediction. The terms present in this equation will be described in detail in the following sections, as well as their respective uncertainties.

$$N_{bgd}^{tot} = N_{p-p}^{SS} + N_{p-p}^{OS} + N_{f-f}^{SS} + N_{p-f}^{SS} \tag{6–2}$$

6.6.1 Determination of Prompt-Prompt, Same-sign Di-leptons: N_{p-p}^{SS}

Potential sources of prompt, same-sign di-lepton final states in pp-collisions are:

(i)   di-boson production: $q\bar{q} \to WZ$ and ZZ

(ii)   double "W-sstrahlung": $qq \to q'q'W^\pm W^\pm$

(iii)   double parton scattering: $2 \times (q\bar{q} \to W^\pm)$

These processes are not yet established, nor well-measured at the LHC (though a few clean event candidates have been detected). Therefore, to predict event rates associated with these processes one simply has to rely on the theoretical predictions and the associated theoretical uncertainties.

The double parton scattering events are expected to be heavily suppressed by the selection requirements based on hadronic activity. Therefore, such contributions can simply be ignored. However, the double "W-sstrahlung" $qq \to q'q'W^\pm W^\pm$ has all of the prerequisites to mimic the signal (i.e., same sign leptons, $\not{E}_T$, jets) and does contribute at the end.

From the phenomenological point of view, these processes are very much "signal-like" and would have very similar experimental systematic errors to those of the signal (Section 6.7). Table 6-8 summarizes the expected event yields and associated systematic errors for this source of background, which are based on Monte Carlo simulation.

Table 6-8. Event yields and systematic errors for a double "W-sstrahlung" $qq \rightarrow q'q'W^{\pm}W^{\pm}$ and double parton scattering $2 \times (q\bar{q} \rightarrow W^{\pm})$

Di-lepton channel	$\mu\mu$	ee	$e\mu$	total
Number of expected events for VV	0.006	0.000	0.019	0.025
Theoretical systematic error	±0.003	±0.007	±0.010	±0.013
Number of expected events for $qq \rightarrow q'q'W^{\pm}W^{\pm}$	0.021	0.012	0.025	0.058
Theoretical systematic error	±0.011	±0.006	±0.013	±0.029
Total Prompt-Prompt backgrounds	0.026	0.012	0.044	0.083
Experimental errors	±0.005	±0.002	±0.008	±0.015
Total errors	±0.014	±0.007	±0.023	±0.044

6.6.2 Determination of Prompt-Prompt, Opposite-sign Di-leptons: N_{p-p}^{OS}

Based on physics considerations and direct Monte Carlo studies, the charge of electrons is much more likely to be mis-reconstructed than is the charge of muons. In fact, the probability of the latter occurring can simply be ignored, as it is negligible due to the minimum ionizing nature of muons in the momentum range targeted for this analysis. Electrons, on the other hand, can easily emit bremsstrahlung photons while passing through the dense volume of the silicon Tracker. This process can cause small kinks in the reconstructed track that may lead to charge misassignment. However, the electron's energy measurement, largely driven by the ECAL, is hardly affected since the electron and its bremsstrahlung photon(s) are mostly collinear and form one common ECAL supercluster with the total energy of the original electron. The latter feature allows the evaluation of the charge mis-reconstruction rate (charge flip rate) by measuring the number of same-sign di-electron pairs which form an invariant mass that lies within a small window surrounding the Z-boson mass. The di-electron pairs contributing to the Z-boson mass peak should inherently be oppositely charged ($Z \rightarrow e^+e^-$).

The first step in predicting this background is to simply count the number of same-sign di-electrons within the Z mass window after imposing a $\not{E}_T$ veto (to suppress neutrino activity from $W+$jets and $t\bar{t}$), and divide this number by the yield of $Z \to e^+e^-$ events, as in Eq. 6–3.

$$\varepsilon_{flip} = \frac{1}{2} \cdot \frac{N_{Z(e^\pm e^\pm)}}{N_{Z(e^+e^-)}} \tag{6–3}$$

The flip rate for the electrons used in this analysis is measured to be $\varepsilon_{flip} = 0.5 \cdot (5/3642) = 0.0007 \pm 0.0003$ and is consistent with the expectation from Monte-Carlo–based studies.

Next, an analysis is performed with the final selection criteria, except now asking for two opposite-sign di-leptons. The observed event yields are: $8\ \mu^+\mu^-$, $6\ e^+e^-$, and $6\ \mu^\pm e^\mp$ events. Using the measured yields of opposite-sign di-leptons and the measured charge flip rate, one can predict the background rate of events due to prompt, opposite-sign di-leptons ($e\mu$ and ee), where one electron has been reconstructed with the wrong charge. The results are provided in Table 6-9. With the current amount of data, the error on this measurement is largely driven by the small number of same-sign di-electron events observed in the Z-boson mass window.

Table 6-9. Event yields for the analysis with opposite-sign di-lepton pairs, measured probability of a charge flip for electrons, and final data-driven prediction of the rate of events where two original leptons are prompt, but one of them is mis-reconstructed with the wrong charge.

Di-lepton channel	$\mu\mu$	ee	$e\mu$	total
Number of observed OS di-leptons	8	6	6	20
Expected rate of SS di-leptons ($\varepsilon = 0.0007 \pm 0.0003$)	-	$2N_{ee}\varepsilon$	$N_{e\mu}\varepsilon$	
	-	0.0082	0.0041	0.0124
Statistical error	-	± 0.0050	± 0.0025	± 0.006

6.6.3 Determination of Fake-Fake, Same-sign Di-leptons: N_{f-f}^{SS}

The background from QCD multi-jet processes, although not expected to dominate, nevertheless needs careful investigation because it is not well known. A method for

evaluating the QCD background contribution has been developed, which relies on the factorization of three selection criteria: two RelIso requirements (i.e., one for each lepton) and the $\not{E}_T$ requirement. The following generic notation will be used to denote these respective selection requirements:

$$\text{Selection Requirement } a \;\equiv\; \mathrm{RelIso}(\ell_1) < 0.15 \tag{6–4}$$

$$\text{Selection Requirement } b \;\equiv\; \mathrm{RelIso}(\ell_2) < 0.15 \tag{6–5}$$

$$\text{Selection Requirement } c \;\equiv\; \not{E}_T > 30 \text{ GeV} \tag{6–6}$$

The Factorization method relies on the ansatz that these three selection requirements are uncorrelated for QCD processes (fake-fake di-leptons). This assumption is well-motivated because both leptons are guaranteed to be non-prompt and should come from distinct jets. Thus, the RelIso variable should be constructed with a unique set of tracks and calorimeter energy deposits for each lepton, respectively. The main source of $\not{E}_T$ is expected to be due to jet energy mismeasurement and not from the soft neutrino activity accompanying the non-prompt leptons. Based on these expectations, the probability (ε_a) for an event to pass requirement a should be the same regardless of whether or not requirements b or c have already been imposed. This should be true for all permutations of a, b, and c. This is the principle that underlies the Factorization method.

In order to employ the method, it is important to verify that the chosen selection requirements can indeed by factorized. This must be done by proving the relationship in Eq: 6–7.

$$\varepsilon_{abc} = \varepsilon_a \cdot \varepsilon_b \cdot \varepsilon_c \tag{6–7}$$

Thus, each probability (or selection efficiency) must be individually measured on the yields surviving the baseline selection, which are expected to be dominated by QCD events. The product of these respective efficiencies should agree with the

cumulative selection efficiency (ε_{abc}), which is obtained after applying each requirement successively.[3] The prediction for the number of events surviving the final selection requirements from the fake-fake di-lepton backgrounds will be product of the three factorizable efficiencies along with baseline selection yields for each channel. This is shown more formally in Eq. 6–8, where the abstract indices a, b, and c are replaced those indicating the particular selection requirement for each channel.

$$
\begin{aligned}
N^{SS}_{f-f} &= N^{\text{baseline}}_{\mu\mu} \cdot \varepsilon_\mu \cdot \varepsilon_\mu \cdot \varepsilon_{\not{E}_T} \\
&+ N^{\text{baseline}}_{ee} \cdot \varepsilon_e \cdot \varepsilon_e \cdot \varepsilon_{\not{E}_T} \\
&+ N^{\text{baseline}}_{e\mu} \cdot \varepsilon_e \cdot \varepsilon_\mu \cdot \varepsilon_{\not{E}_T}
\end{aligned}
\tag{6–8}
$$

From Tables 6-4, 6-5 and 6-6, it was observed that the total SM background, which passes the baseline selection does not compare very well with data. This is due to the fact that the Monte Carlo simulations cannot faithfully account for the large QCD contribution. The simulated yields are lower by roughly a factor of two. Despite this, it is still worthwhile to use QCD Monte Carlo simulations to validate the Factorization method because the absolute event rates are not needed. Only the principle of factorizability needs to be demonstrated, but this still requires an adequate amount of statistics, however. To augment the statistics in the inclusive QCD multi-jet MadGraph samples, one can appeal to a dedicated sample of events which feature $b\bar{b}$ production. These are listed in Table 6-1, but were not used to calculate the yields in Tables 6-4, 6-5 and 6-6. The expectation is that a significant fraction of leptons in QCD events actually originate from the particular subset of processes which feature b-quarks or b-jets. For this part of the analysis, we find it convenient to combine the inclusive QCD samples with the

---

[3] The cumulative selection efficiency can also be understood as the probability to pass the final selection requirements given that the event has passed the baseline selection requirements.

$b\bar{b}$ samples in order to enhance the number of simulated events with leptons. Special

care is taken to avoid double counting as the inclusive QCD sample does have a small

component of $b\bar{b}$ events (roughly 4%). Table 6-10 shows the baseline event yields from

this QCD+$b\bar{b}$ cocktail sample (scaled by cross-section to 35 pb^{-1}) along with the data.

The scaling factor of the cocktail includes an additional factor of two in order to roughly

normalize the yields to data.[4] One can argue that this factor could be even higher. The

total baseline yields from all Standard Model processes, including the QCD cocktail,

is provided in order to illustrate the fact that the sample is dominated by QCD events

before the RelIso and $\not{E}_T$ requirements are imposed. This fact is vital to the success of

the method because the baseline sample is used as a QCD control sample to derive ε_μ,

ε_e, and $\varepsilon_{\not{E}_T}$.

Table 6-10. Baseline yields for data and Monte Carlo simulated data

Process	$N_{\mu\mu}$	$N_{e\mu}$	N_{ee}
$b\bar{b} : H_T \in [100, 250]$ GeV	0	0	0
$b\bar{b} : H_T \in [250, 500]$ GeV	32.6	15.1	1.94
$b\bar{b} : H_T \in [500, 1000]$ GeV	2.87	0.915	0.0821
$b\bar{b} : H_T \in [1000, \infty]$ GeV	0.0167	0.00518	0.00115
QCD $: H_T \in [100, 250]$ GeV	0	0	0
QCD $: H_T \in [250, 500]$ GeV	84.4	46	0
QCD $: H_T \in [500, 1000]$ GeV	14.2	6.22	0.361
QCD $: H_T \in [1000, \infty]$ GeV	0.0167	0.00518	0.00115
Total QCD +$b\bar{b}$ Cocktail	134	68.3	2.39
Total Standard Model	148	79.8	4.1
Data	223	78	6

The baseline yields are noticeably lopsided in favor of $\mu\mu$ events, giving a ratio

of $N_{\mu\mu}/N_{ee} = 37.2$ in data. This enhancement can be attributed to a combination of 3

factors (ordered by importance):

---

[4] Next-to-leading order cross-sections for such QCD multi-jet processes are not available, nor are proper k-factors. This *ad hoc* normalization to data is a common procedure.

(i)   lower p_T requirements on the muons

(ii)   tighter identification requirements on the electrons (VBTF80)

(iii)   higher reconstruction efficiencies for both non-prompt and prompt muons

The effect of the differences in p_T requirements can be studied simply by equalizing them to 10 GeV for muons and electrons. This yields 38 $\mu\mu$ events (26 $e\mu$ events), which reduces the di-muon/di-electron asymmetry to a factor of 6.3. One must take the square root of this number to obtain the asymmetry in the single lepton production rate, i.e., $\sqrt{6.3} = 2.5$. By appealing to the QCD simulation, we can investigate and validate the sources leading to the remaining asymmetry. Looking at the Monte Carlo truth[5] , we observe that muons from heavy-flavor decays are roughly 3 to 5 times more likely than electrons to pass their respective selections. The effect from this source as well as others are detailed in Table 6-11. In some cases, a source favors electrons over muons. Sources denoted by (*) are not explicitly matched via a generator-level lepton in the Monte Carlo truth. In these cases, the list of generator particles is searched for a stable particle within a cone of $\Delta R < 0.01(0.02)$ of the reconstructed muons (electrons). The sum of all of these sources yields a ratio of observed muons to electrons in our acceptance of 1.9, which is roughly consistent with our observations in data.

Having established that the baseline selection is indeed dominated by QCD, it is now left to show that the selection efficiencies can be factorized. The demonstration will be done piece-wise. First it will be shown that the RelIso requirements are independent for each lepton (i.e., $\varepsilon_{ab} = \varepsilon_a \cdot \varepsilon_b$). In the case that we are dealing with the $\mu\mu$ or ee channels, the relationship can be simplified to $\varepsilon_{ab} = \varepsilon_a^2$. Then, it will be shown that the RelIso requirement is independent of the $\displaystyle{\not}E_T$ requirement (i.e., $\varepsilon_{ac} = \varepsilon_a \cdot \varepsilon_c$).

---

[5] The Monte Carlo truth consists of the list of particles that were actually generated in the event, as opposed to those that were reconstructed by the CMS detector

Table 6-11. Summary of non-prompt lepton origins in simulated QCD

Source	N_μ	N_e	N_μ/N_e
b	$2.34e+03$	656	3.56
$b \to \tau$	59	15	3.93
$b \to c$	328	58	5.66
c	$1.01e+03$	187	5.4
light flavor	15	42	0.357
p (*)	7	38	0.184
$\pi^\pm$ (*)	440	477	0.922
$k^\pm$ (*)	342	106	3.23
k_L (*)	1	2	0.5
γ (*)	2	50	0.04
unmatched	5	759	0.00659
Total	$4.54e+03$	$2.39e+03$	1.9

It is fairly straightforward to show that the RelIso of one lepton is effectively independent of the RelIso of the other in di-lepton QCD events. Figure 6-8 shows that the factorization holds in both the data and the simulation for all three channels to within statistical errors. Here, ϵ_a is represented by dark blue filled circles, ϵ_{ab} is represented in red filled squares, and $\epsilon_a \epsilon_b$ is represented in light blue filled rectangles. For the case of the $e\mu$ channel, $\epsilon_b \neq \epsilon_a$, so ϵ_b is represented separately by black filled triangles. As one can readily observe, the agreement is present for all channels in data and simulation. It is worth emphasizing that one greatly reduces the statistical errors for the measurement of the RelIso selection efficiency ϵ_{ab} by exploiting the relationships given above. The values of ϵ_a and ϵ_b are measured to good statistical precision, while ϵ_{ab} cannot be because it requires simultaneously applying the selection to both leptons, as is illustrated by the sizable errors (red) in Figure 6-8. There simply are not very many events that survive this requirement. While the actual data-driven measurement of these selection efficiencies meant for the QCD prediction will be extracted from the baseline selection yields, the distributions shown in Figure 6-8 come after relaxing the H_T requirement to 200 GeV. This is done in order to enhance statistics.

For completeness a few more checks are performed to ensure that ϵ_a and ϵ_b are mutually independent of each other. Figure 6-9 shows the differential RelIso (μ_2)
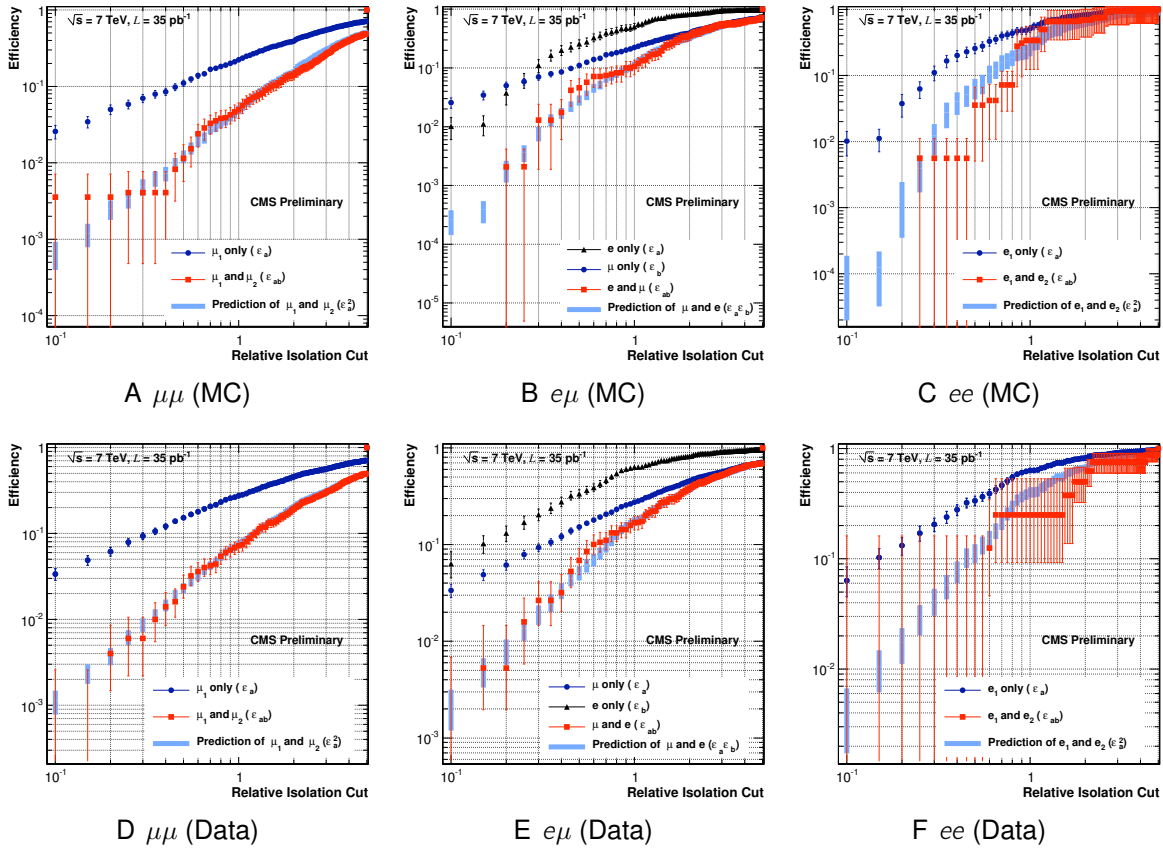
Figure 6-8. RelIso selection efficiencies in QCD simulation (top) and data (bottom) for the $\mu\mu$, $e\mu$, and ee channels respectively.

distribution in bins of RelIso (μ_2). Unfortunately, differential distributions such as these are statistically limited and only coarse binning in RelIso (μ_1) is feasible. However, since we have relaxed the H_T cut from 300 to 200 GeV for this demonstration, some efficiency is lost in the event yields due to the slow turn-on of the H_T triggers. To combat this we can appeal to another trigger, namely, a double-muon trigger to augment the statistics collected by the H_T triggers. This enables a view of RelIso (μ_2) for a thinner slice near our signal region of RelIso (μ_1). In all three plots, the shapes of the two distributions are in agreement to within statistical errors. Similar distributions for the $e\mu$ and ee channels are too statistically limited to reveal anything of substance, so they are not shown here.

A final check of the correlation between the respective RelIso selection requirements can be performed by plotting the 2-dimensional differential distribution of RelIso (ℓ_2) vs

RelIso (ℓ_1) for $\mu\mu$, $e\mu$, and ee events respectively. This is done in Figure 6-10 for data and

QCD simulation, and the correlation factors are displayed in red text in each subfigure.

For the $\mu\mu$ channel a small, but non-negligible, negative correlation factor at a value

of about -0.06 is observed in the data and the QCD simulation. For the $e\mu$ channel

the correlation factors are negligible and for the ee channel statistics are too limited to

draw any further conclusions, so we are forced to rely on Fig 6-8 as evidence that the

factorization principle is valid. Further studies show that the correlation factor goes from

-0.06 to to 0.01 in the QCD simulation as the H_T requirement is restored to is nominal

values of 300 GeV. While it is comforting to see small correlation factors, there will

inevitably be non-QCD processes present in the data surviving the baseline selection,

which could contribute to some subtle correlations. The process of $t\bar{t} \rightarrow b\bar{b}W^+W^-$ for

example, will likely have one isolated lepton (from a W-decay) and one non-isolated

lepton (from a b-quark) if it passes the baseline requirements. The presence of small

correlations will have an impact on the closure tests and will thus be incorporated in the
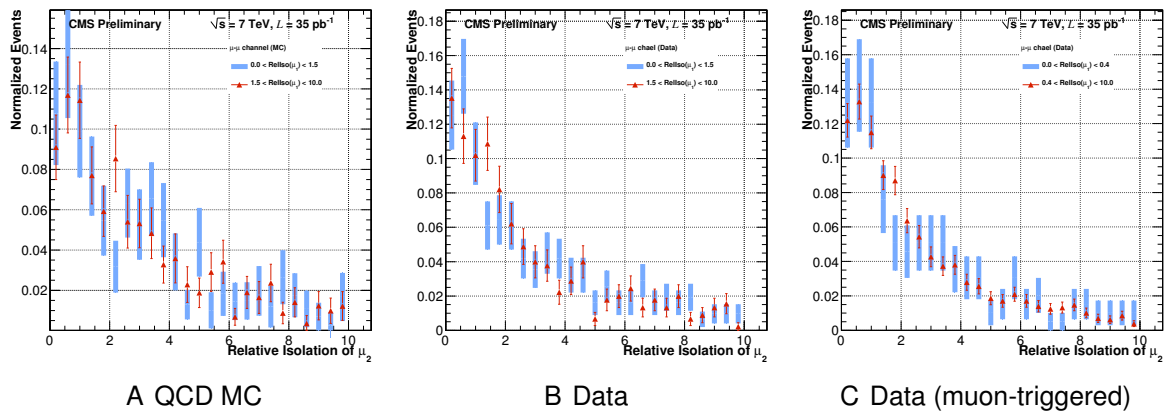
systematic errors quoted for the measurement.

| A QCD MC | B Data | C Data (muon-triggered) |

Figure 6-9. Differential $\mathrm{RelIso}(\mu_2)$ distribution of for $0.0 < \mathrm{RelIso}(\mu_1) < 1.5$ (blue) and for $1.5 < \mathrm{RelIso}(\mu_1 < 10.0$ (red) for QCD simulation (left) and data with only the H_T triggers (middle) and augmented by muon triggers (right).

Having justified the factorization of the RelIso selection requirements on the two

leptons in the event, it is now left to show that the requirement on $\not{E}_T$ can be factorized
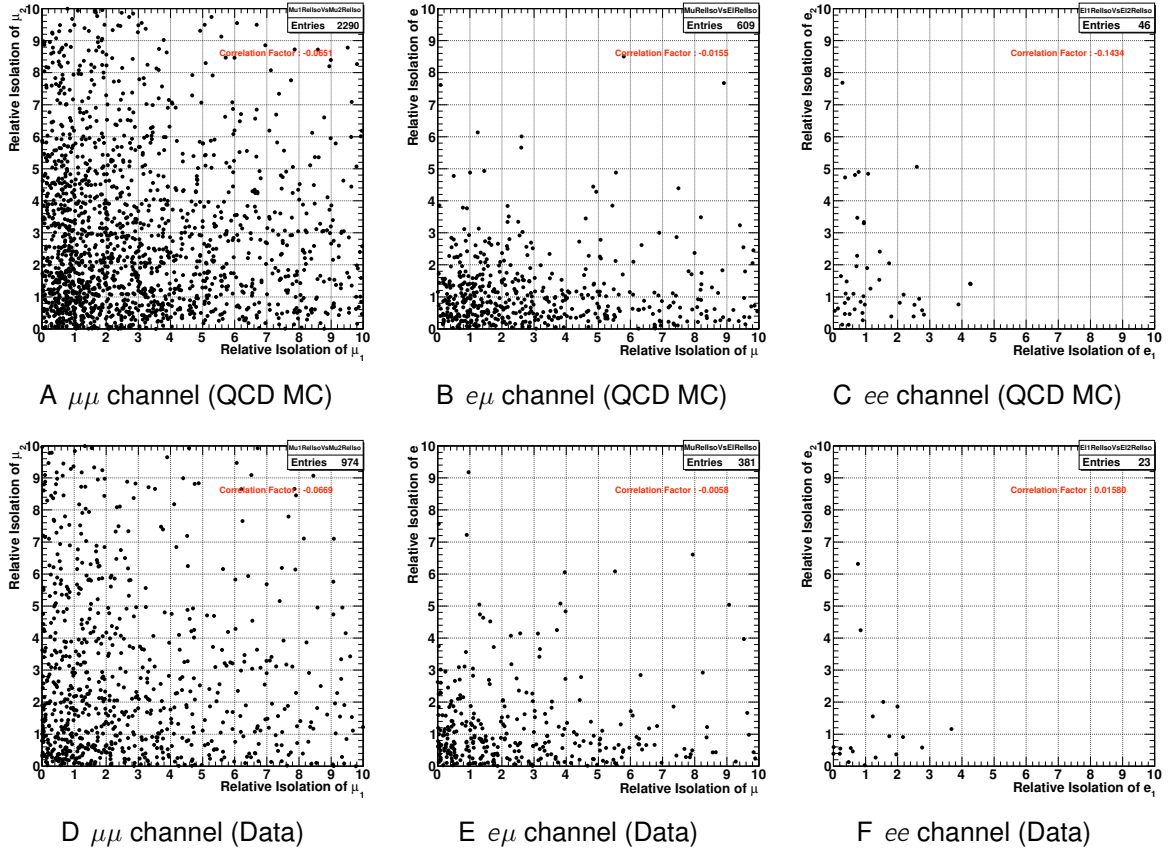
Figure 6-10. Differential distribution of $\mathrm{RelIso}(\ell_2)$ vs $\mathrm{RelIso}(\ell_1)$ for QCD simulation (top) and data (bottom).

from the RelIso requirement on one of the two leptons. Figure 6-11 shows the RelIso selection efficiency for muons (left) and electrons (right) for different values of the $\not{E}_T$ requirement for QCD simulation (top) and data (bottom). The curves from the QCD simulation are in good agreement, and this demonstrates that the factorization holds for QCD events. It is worth emphasizing that we do not expect the curves to overlap perfectly in the data due to the presence of non-QCD processes (e.g $t\bar{t}$). Because we will measure the RelIso efficiencies in data, which will presumably contain non-QCD events, we will impose an inverted $\not{E}_T$ requirement at a value below 20 GeV, where we expect contributions from QCD to dominate. The effects of this inverted requirement on data can be seen by the light blue-shaded curve in Figure 6-11.
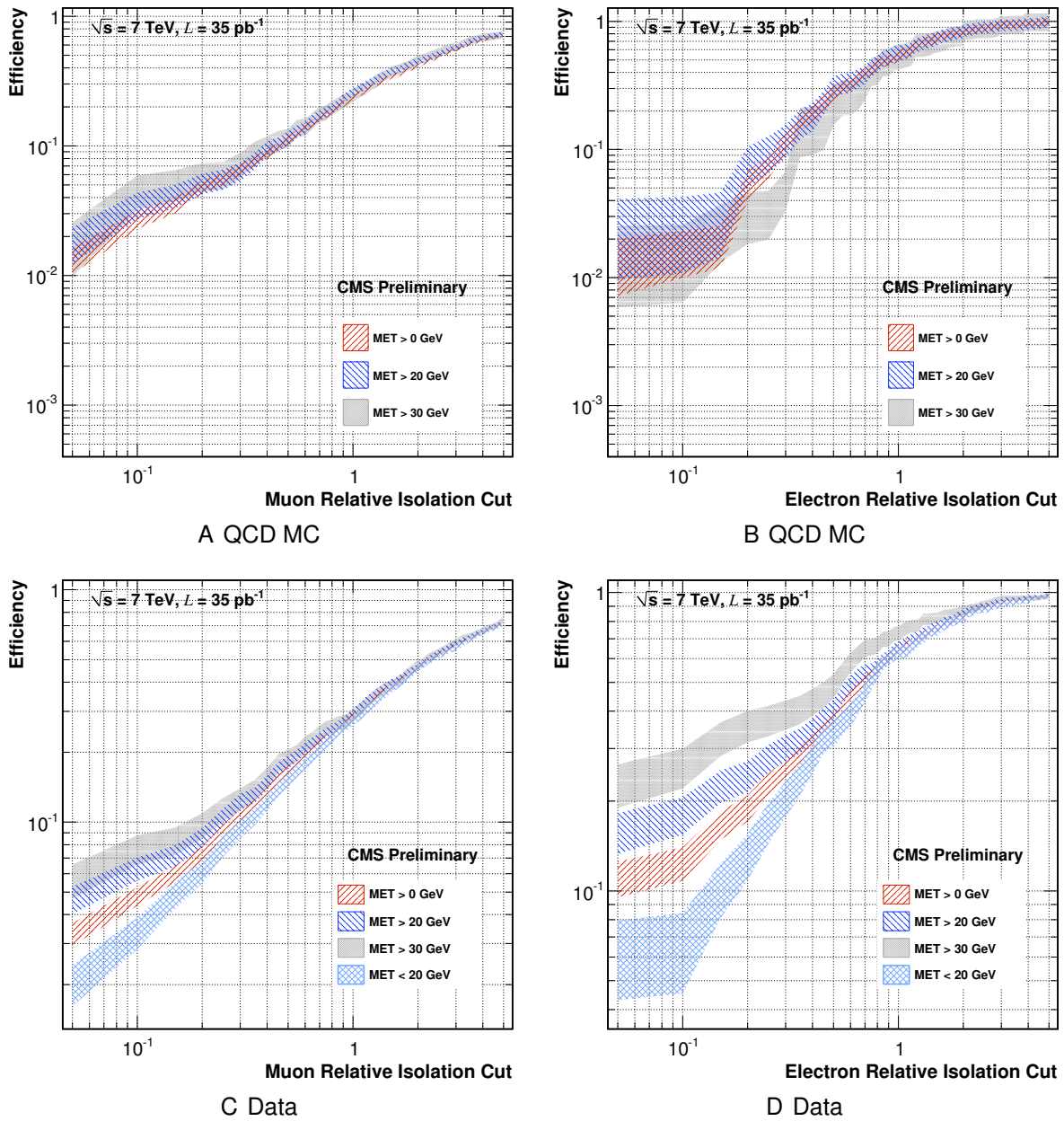
Figure 6-11. Efficiency of $\mathrm{RelIso}\,(\ell_1)$ as a function of the $\not{E}_\mathrm{T}$ requirement for simulated QCD (top) and data (bottom) for $\ell_1 = \mu$ (left) and $\ell_1 = e$ (right). The distributions in data, are not expected to demonstrate factorization due to the non-negligible presence of other backgrounds.

With the mutual independence of the three selection requirements established, it is now left to measure the values for ε_μ, ε_e, and $\varepsilon_{\not{E}_T}$ individually from the events passing the baseline selection. Figure 6-12 shows the event yields and cut efficiencies as a function of the selection requirement on RelIso for muons coming from $\mu\mu$ and $e\mu$ candidate events for collision data and Monte Carlo simulated data. It is worth reemphasizing that while measuring the selection efficiency of the RelIso requirement, the $\not{E}_T$ requirement is inverted at a value of 20 GeV to mitigate any biases due to $t\bar{t}$ and potentially signal. Here, the QCD portion of the simulated data is shown separately from the Standard Model to illustrate its behavior. Figure 6-13 shows the same distribution, only now for electrons coming from ee and $e\mu$ candidate events. Again, the QCD is shown separately from, as well as combined with, the rest of the Standard Model simulation samples. Figure 6-14 shows the event yields and efficiencies as a function of the requirement on $\not{E}_T$ for $\mu\mu$ events. The shapes are qualitatively very similar for all three channels. When measuring the cut efficiency on the $\not{E}_T$ observable, the RelIso requirement is inverted on both leptons at a value of 0.2 to avoid potential biases from signal and non-QCD processes.

The largest uncertainty with respect to this measurement is expected to be statistical. This is due mainly to the fact that the measurement consists of multiplying the values of four observables, which each obey Poisson statistics and will derive from samples that are scantly populated. As will be shown the statistical errors for the QCD prediction for each channel will range from $50\% - 100\%$ despite clever attempts to increase the sample population without biasing the measurement. Nonetheless, despite the large uncertainties which will come from poor statistics, other systematic uncertainties need to be accounted for in the measurement.

A common method for assessing systematic errors and biases in a data-driven measurement usually involves performing a "closure test" on a Monte Carlo simulated sample that is meant to serve as pseudo-data. In such a test we would measure the
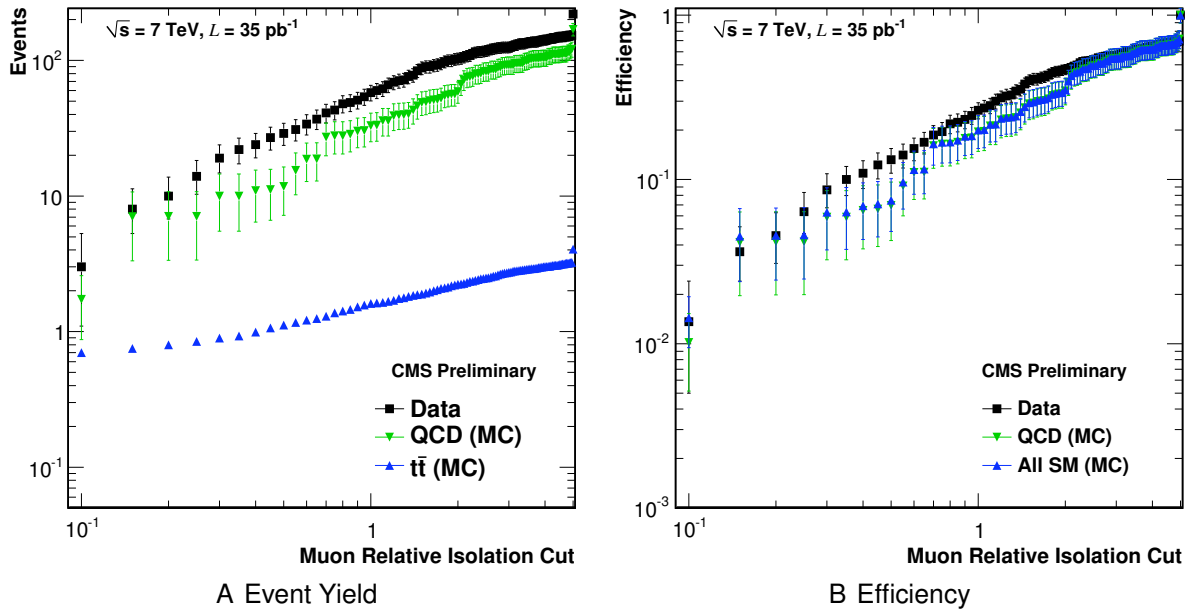
Figure 6-12. Event yields (left) and selection efficiency (right) given as a function of the cut on the muon Relative Isolation taken from $\mu\mu$ and $e\mu$ events passing the baseline selection.
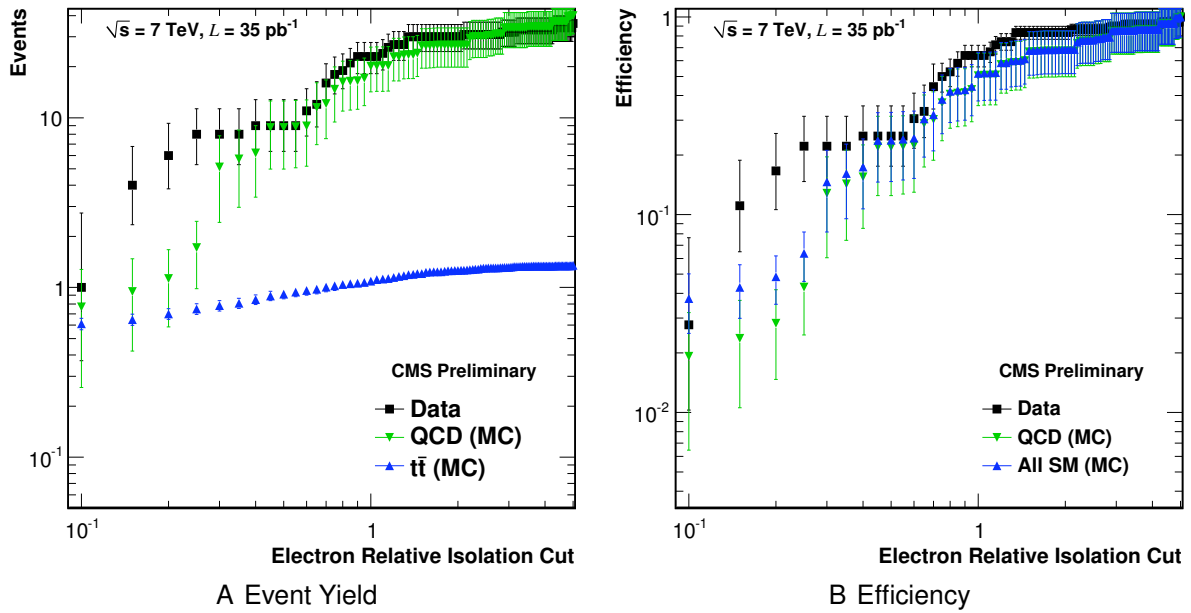

Figure 6-13. Event yields (left) and selection efficiency (right) given as a function of the cut on the electron Relative Isolation taken from ee and $e\mu$ events passing the baseline selection.
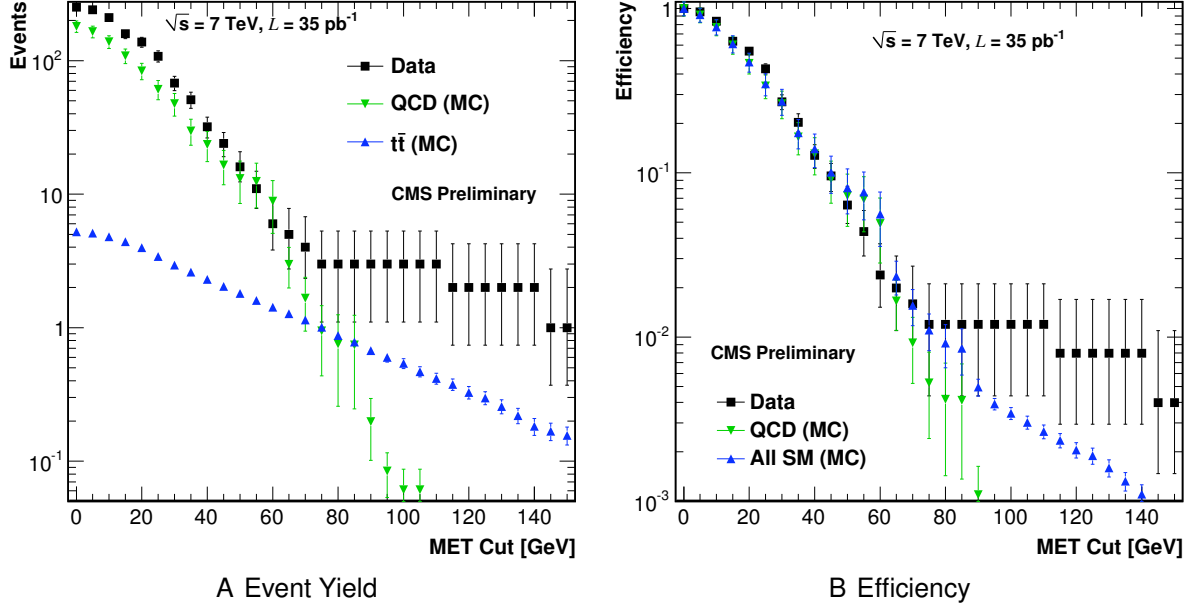
Figure 6-14. Event yields (left) and selection efficiency (right) given as a function of the cut on the $\not{E}_T$ taken from $\mu\mu$ events passing the baseline selection.

four observables, N^{baseline}, ε_μ, ε_e, $\varepsilon_{\not{E}_T}$, then take the appropriate product to derive the prediction for each channel, and finally compare the prediction with the number of events which survive once all of the selection requirements are applied (i.e., baseline selection, $\text{RelIso}\,(\ell_1)$, $\text{RelIso}\,(\ell_2)$, $\not{E}_T$). These two numbers will be referred to as $N_{\text{predicted}}$ and N_{observed}, respectively. If the method is valid then the relationship in Eq. 6–9 is verified and the closure test is satisfied.

$$
\begin{aligned}
N_{\text{observed}} &= N_{\text{predicted}} \\
\rightarrow N^{\text{baseline}} \cdot \varepsilon_{abc} &= N^{\text{baseline}} \cdot \varepsilon_a \cdot \varepsilon_b \cdot \varepsilon_c
\end{aligned}
\tag{6–9}
$$

Unfortunately, a complete closure test as described by Eq. 6–9 cannot be performed because there simply are not enough QCD events available in the simulation. This is one of several factors which heavily motivated the data-driven measurement of the QCD background in the first place. We will never be able to simulate enough QCD

events to check Eq. 6–9 directly. As a consolation we can redefine N^{observed} and $N^{\text{predicted}}$ and instead test for the following relationships in a piecewise manner:

$$N^{\text{baseline}} \cdot \varepsilon_{ab} = N^{\text{baseline}} \cdot \varepsilon_a \cdot \varepsilon_b \qquad (6\text{--}10)$$

$$N^{\text{baseline}} \cdot \varepsilon_{ac} = N^{\text{baseline}} \cdot \varepsilon_a \cdot \varepsilon_c \qquad (6\text{--}11)$$

We have already shown that these relationships hold qualitatively by the agreement shown in Figures 6-8 and 6-11, but more quantitative comparisons can help to reveal any systematic uncertainties. We begin with a test of the first relationship and we focus on the $\mu\mu$ channel as it has the most statistics. Even though we do not perform the full QCD prediction here by multiplying all three efficiencies, the single lepton efficiency is small enough, that when squared (or multiplied by the opposite-flavor lepton efficiency for the $e\mu$ channel), very few (if any) events are expected to survive. Unfortunately, the QCD simulation samples do not provide enough statistics to allow for a test of even this partial closure test. However, we can try to perform the partial closure test directly in the data, which is QCD-dominated (particularly once the inverted cut on the $\not{E}_T$ is applied), and can supply the sufficient statistics to test Eq. 6–10. As one can readily observe by comparing the red points in Figure 6-8A with Figure 6-8D, the latter (data) is better populated at low values of the RelIso observable. Still, given that the final selection requires $\text{RelIso} < 0.15$, we will have to test for closure at that value and we barely cannot, even with greater statistics afforded by the data. To overcome this we can try to invite more events into the baseline selection yields by appealing to muon-triggered data. Recall, we relax the H_T selection requirement from 300 GeV to 200 GeV to validate the Factorization method and check for closure. This relaxation comes at the cost of trigger efficiency from the main H_T triggers employed in this analysis (Table 6-2), but we can recover many events for this purpose by supplementing the main triggers with muon triggers. By doing this we obtain a similar distribution in Figure 6.6.3 to

what was obtained in 6-8D with solely the H_T triggers, except now the lowest bins are occupied, albeit scarcely.

In Figure 6-16A, we show the results of the partial closure test on data of Eq. 6–10. At the nominal selection requirement of $\mathrm{RelIso} < 0.15$, we see that the method closes, although there is some variation at the adjacent selection requirement values which are likely due to statistical fluctuations combined with fine binning. The trend is quite clear that for the majority of RelIso selection requirements, there is very good agreement between prediction and observation. The gray band represents a $\pm 25\%$ spread which foreshadows the systematic uncertainty that will be assigned to the method from the results of the closure test. With few exceptions, all points are within this band.
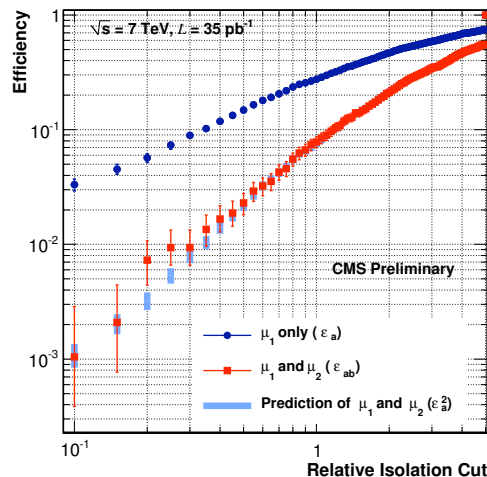

Figure 6-15. RelIso factorization in the $\mu\mu$ channel after adding muon-triggered events.

To test for closure of the relationship in Eq. 6–11, we are forced to rely on simulation if we want to perform the test with the same-sign di-lepton topology, as it is too difficult to perform the test in a control region in data. Figures 6-16B and 6-16C show results from the Monte-Carlo–based closure test of the relationship in Eq. 6–11. More concretely, we compare the values of the $\mathrm{RelIso}(\mu)$ selection efficiency obtained in the control region ($\not{E}_T < 20$ GeV) with the efficiency observed in the signal region ($\not{E}_T > 30$ GeV). The former constitutes the prediction while the latter constitutes the observation. The ratio
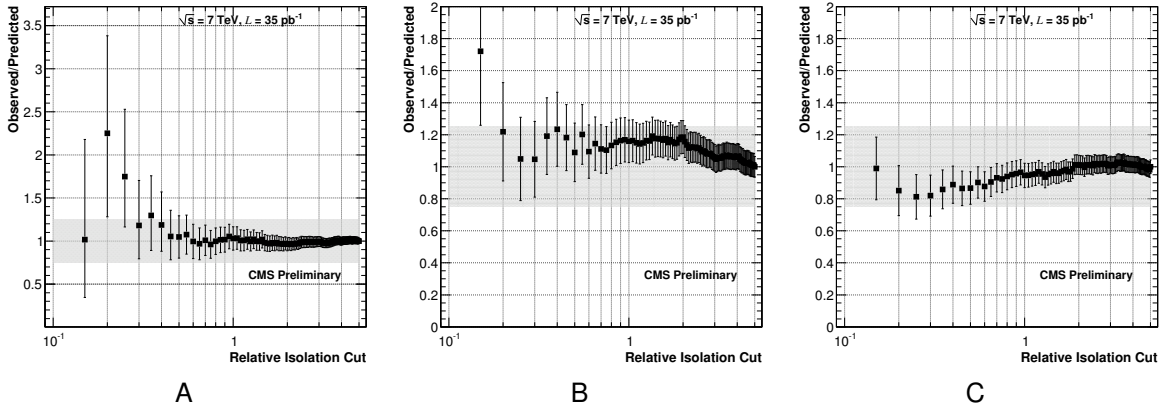
Figure 6-16. Closure tests of relationships in Eqs. 6–10 for $H_T > 200$ GeV (left) and Eqs. 6–11 for $H_T > 200$ GeV (middle) and $H_T > 100$ GeV (right) using single-lepton events.

of the two is plotted as a function of the $\mathrm{RelIso}(\mu)$ requirement for the case where the H_T requirement is relaxed to 200 GeV and further relaxed to 100 GeV. For the former (6-16B) the closure test is quite stable across a wide range of values for the RelIso requirement and most points reside well within the $\pm 25\%$ band surrounding unity. The lone outlier occurs at the nominal value of the RelIso requirement (0.15) where statistical fluctuations are quite probable. To see if the outlier at $\mathrm{RelIso} < 0.15$ is due to non-statistical effects one can check to see if the fluctuation persists after the H_T requirement is relaxed to 100 GeV, which is done in Figure 6-16C. It is observed that test of closure is achieved in this case and all points maintain a short distance from unity and reside well within the $\pm 25\%$ band.

One can also attempt to test for closure of the relationship in Eq. 6–11 by using a single-lepton QCD control region in data, where statistics are much more plentiful than in the same-sign di-lepton case. This allows the H_T requirement to be maintained at its nominal value of 300 GeV, without sacrificing too many events. Figure 6-17 shows the RelIso selection efficiency for muons (red) and electrons (blue) as a function of the requirement on the $\not{E}_T$. As one can readily observe, the dependence is strong and the cuts do not factorize in the region defined by $d_0 < 0.1$ mm, which is contaminated by

many events containing prompt leptons from W-decays. The region defined by the inversion of this d_0 requirement, however, is dominated by events with non-prompt leptons from heavy-flavor decays or hadron decays-in-flight, and thus constitutes a very pure QCD control region where the closure test can be performed. It is worth exploring how dramatically the cocktail of non-prompt leptons changes in composition as one goes from the signal region ($d_0 < 0.2$ mm) to this QCD control region ($d_0 > 0.1$ mm). This was checked in QCD simulation. In the signal region, the composition of fake leptons in QCD is 45% fake and 55% heavy-flavor, while for the control region it is 25% fake and 75% heavy-flavor. It is observed that the RelIso selection efficiency is quite stable with respect to the requirement on the $\not{E}_T$ in this QCD control region, and this observation is expected to hold independent of the relative fractions of fake leptons from fake and heavy-flavor sources respectively.
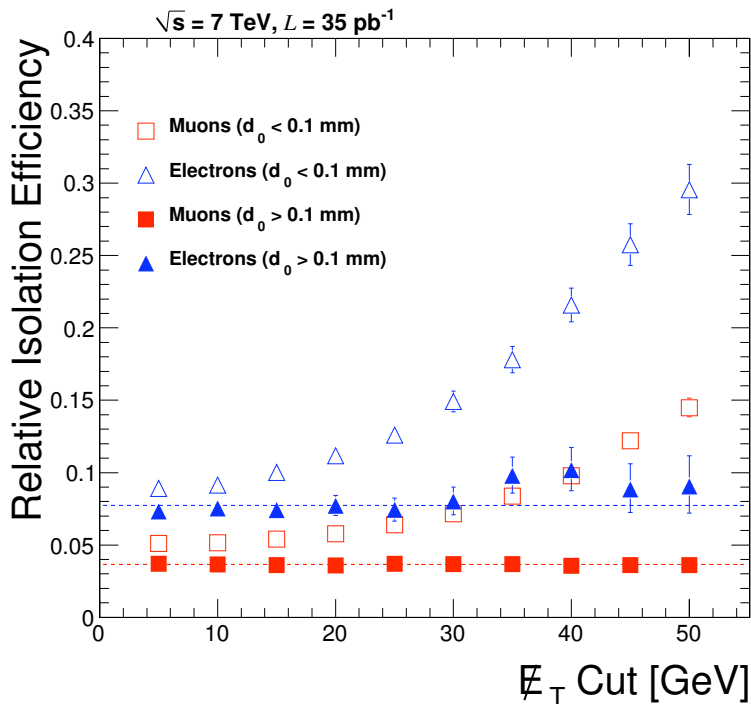

Figure 6-17. Demonstration that the RelIso and $\not{E}_T$ selections factorize using a single lepton QCD control region in data.

It can be concluded that the three selection requirements chosen after the baseline selection do indeed factorize quite well. A uniform 25% systematic uncertainty is

assigned to the measurement of N_{f-f}^{SS} and 100% correlation for all three channels is assumed in order to cover the spread of values obtained in the closure tests.

Another possible source of systematic uncertainty that has not directly been discussed may come from the inversion of the $\not{E}_T$ requirement when measuring the RelIso selection efficiency or likewise from the inversion of the RelIso requirement when measuring the $\not{E}_T$ selection efficiency. This is simply another way for correlations of the two observables to bias the efficiency measurement of either one. As Figures 6-8, 6-9, 6-10, and 6-11 demonstrated, any existing correlations whether present in the underlying physics or introduced by the detector are hardly noticeable. Nonetheless, one can see how the selection efficiency of RelIso varies as the inverted requirement for the $\not{E}_T$ is changed and vice versa. This is done in Figure 6-18 for both RelIso (bottom) and $\not{E}_T$ (top) for both $H_T > 300$ GeV (left) and $H_T > 100$ GeV (right). As can be readily observed the measured selection efficiencies are very stable with respect to the values of the inverted selection requirements. Deviations are observed on the level of $\sim 1\%$. Thus, no systematic uncertainty is attributed to this effect.

As discussed earlier the sample of events passing the baseline selection is expected to be dominated by QCD, but it most certainly will not be without other backgrounds, and potentially signal. The presence of these other backgrounds directly enhances the value of N^{baseline} and will hence directly enhance the value of $N^{\mathrm{predicted}}$. From the Monte-Carlo–based baseline selection yields N^{baseline} is observed to have 6.4%, 11.6%, and 34.5% contamination from non-QCD processes for the $\mu\mu$, $e\mu$, and ee channels respectively. These biases can be factored in asymmetrically as a source of systematic uncertainty for the final measurement. This uncertainty is asymmetric because the presence of these other backgrounds will serve only to increase the value of $N^{\mathrm{predicted}}$ from the true number of QCD events. Their presence cannot make the predicted number any smaller than it would otherwise be.
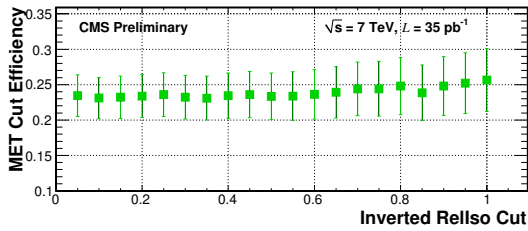
A QCD Monte Carlo ($H_T > 300$)
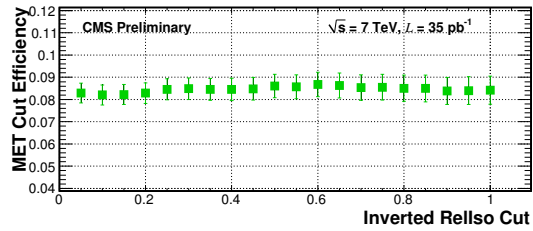
B QCD Monte Carlo ($H_T > 100$)
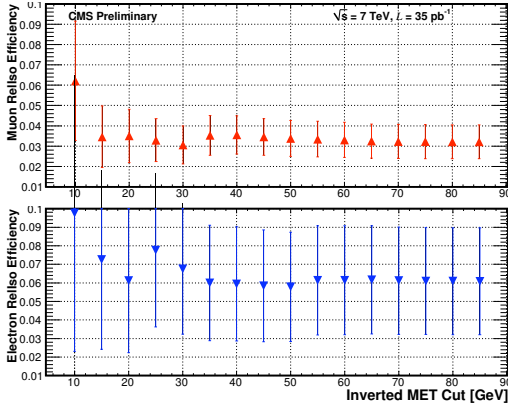
C QCD Monte Carlo ($H_T > 300$)

D QCD Monte Carlo ($H_T > 100$)
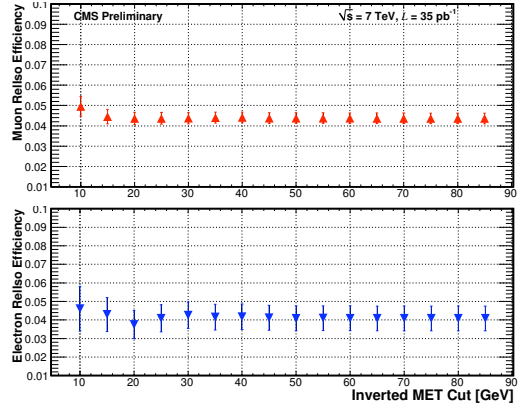
Figure 6-18. Testing the stability of the observed $\not{E}_T$ selection efficiency (green) for various values of the inverted RelIso requirment (top) and the stability of the observed RelIso selection efficiency of muons (red) and electrons (blue) for various values of the inverted $\not{E}_T$ requirement (bottom).

Similar to the situation with N^{baseline}, there exists some contamination from non-QCD processes in the events that survive the RelIso and $\not{E}_T$ requirements respectively. The amount of contamination for each measured selection efficiency can be inferred by comparing the green and blue distributions in Figures 6-12B, 6-13B, and 6-14B respectively. Anticipating the requirement on these observables to be 0.15 and 30 GeV for RelIso and $\not{E}_T$ respectively, it is determined that the former will invite a systematic uncertainty of -10% and -80% for the cases of muons and electrons respectively, while the latter will invite a systematic uncertainty of -3%.

A final source of systematic error may come from the presence of pile-up events (PU). The effects of pile-up on the RelIso selection efficiencies can be taken to be negligible. The proof of this lies in the fact that the two RelIso requirements do indeed

factorize in the data (implying a successful closure test on these two observables). Thus, whatever effects are in the data due to pile-up do not affect this underlying premise, which is vital to the success of the method. It is worth exploring the effects of pile-up on the $\not{E}_T$ requirement, since it is a global observable that is sensitive to all of the activity reconstructed in the event. This can be studied by evaluating the $\not{E}_T$ selection efficiency for both single and multiple vertex events.[6] This test was performed, and for single vertex events an efficiency of $18/71 = 25.4\% \pm 6.0\%$ is observed, while for multiple vertex events an efficiency of $50/180 = 27.8\% \pm 4.0\%$ is observed. These calculated efficiencies are statistically consistent with one another.

A separate test was also performed to study how pile-up may affect the baseline selection efficiency, which is simply constituted by an H_T requirement. Events passing the pre-selection requirements were separated into single-vertex and multiple-vertex samples. The efficiency for events from the former sample to further pass the baseline selection requirement is observed to be $51/120 = 44.6\% \pm 6.0\%$, while the efficiency for events from the latter sample to pass the baseline selection is observed to be $204/478 = 41.6\% \pm 3.0\%$. The two efficiencies are statistically consistent, indicating that the effects of pile-up, if present, are benign. Therefore, this measurement does not incur any systematic errors due to pile-up effects.

In Table 6-12, all of the sources of uncertainty for both the individual observables and the final measurement of $N^{SS}_{\bar{f}-f}$ are summarized. Values shown in Table 6-12 reflect the final selection requirements for RelIso and $\not{E}_T$, respectively. The relative uncertainty on the closure tests given in Table 6-12 will be applied to the final measurement of each channel. The final ingredients for the data-driven prediction are given in Tables 6-13, 6-14, 6-15. The uncertainties which are asymmetric will be taken conservatively to be symmetric (using the larger error) for the final predictions.

---

[6] The presence of multiple primary vertices indicates the presence of pile-up

144

Table 6-12. Summary of uncertainties on observables of Factorization method.

Observable	Uncertainty	Comment
$N_{\mu\mu}^{\text{baseline}}$	± 14.93 (7%)	statistical
	-14.27 (6.4%)	bias due to p-f contamination (Table 6-10)
$N_{e\mu}^{\text{baseline}}$	± 8.83 (11%)	statistical
	-9.05 (11.6%)	bias due to p-f contamination (Table 6-10)
N_{ee}^{baseline}	± 3.28 (55%)	statistical
	-2.07 (34.5%)	bias due to p-f contamination (Table 6-10)
$\text{RelIso}(\mu)$ efficiency	± 0.015 (42%)	statistical
	-0.004 (10%)	bias due to p-f contamination. (Figure 6-12)
	negligible	bias due to $\not\!E_T$ cut inversion. (Figure 6-18C)
$\text{RelIso}(e)$ efficiency	± 0.077 (70%)	statistical
	-0.089 (80%)	bias due to p-f contamination. (Figure 6-13)
	negligible	bias due to $\not\!E_T$ cut inversion (Figure 6-18C)
$\not\!E_T$ efficiency	± 0.028 (10%)	statistical
	-0.008 (3%)	bias due to p+f contamination. (Figure 6-14)
	negligible	bias due to isolation cut inversion (Figure 6-18A)
$N_{\text{predicted}}$(all channels)	± 0.45 (25%)	statistical uncertainty on closure test (Figure 6-16)

Table 6-13. Control region yields for prediction of fake-fake di-leptons

Observable	$\mu\mu$	ee	$e\mu$	total
Baseline event yields	223	6	78	317
Number of events for the RelIso measurements ($\not\!E_T < 20$ GeV)	94	2	32	128
Number of muons passing $\text{RelIso} < 0.15$	6	–	2	8
Number of electrons passing $\text{RelIso} < 0.15$	–	1	3	4
Number of events for the $\not\!E_T$ measurements ($\text{RelIso} > 0.2$)	194	2	55	251
Number of events passing $\not\!E_T > 30$	58	0	10	68

Table 6-14. Selection efficiencies of fake-fake di-leptons

Observable	Selection Efficiency
$\text{RelIso}(\mu)$ selection efficiency	$\varepsilon_\mu = 0.036 \pm 0.015$
$\text{RelIso}(e)$ selection efficiency	$\varepsilon_e = 0.111 \pm 0.077$
$\not\!E_T$ selection efficiency	$\varepsilon_{\not\!E_T} = 0.271 \pm 0.028$

Table 6-15. Data-driven background prediction of fake-fake di-leptons

	$N_{\mu\mu} \cdot \varepsilon_\mu^2 \cdot \varepsilon_{\not\!E_T}$	$N_{ee} \cdot \varepsilon_e^2 \cdot \varepsilon_{\not\!E_T}$	$N_{e\mu} \cdot \varepsilon_\mu \cdot \epsilon_e \cdot \epsilon_{\not\!E_T}$	total
Prediction	0.078	0.020	0.084	0.183
Statistical+Systematic error	± 0.060	± 0.028	± 0.084	± 0.169

6.6.4 Determination of Prompt-Fake, Same-Sign Di-leptons: N^{SS}_{p-f}

As Monte-Carlo–based studies suggest (Tables 6-4, 6-5 and 6-6), it is expected that the main background component in this search is due to $t\bar{t}$ production. In $t\bar{t}$ events it is natural to have relatively large H_T and $\not{E}_T$. Two isolated, same-sign leptons appear in $t\bar{t}$ events when one lepton comes from a W-decay (prompt lepton) and another fake lepton from a b-jet (isolated by chance). In order to evaluate this background, a dedicated data-driven method has been developed referred to as the BTag-and-Probe method.

Using the knowledge that the fake leptons from $t\bar{t}$ production come from semi-leptonic b-decays, one can attempt to model the RelIso distributions for muons and electrons by studying QCD events which feature $b\bar{b}$ production. In order to get a good sample of leptons originating from b-jets, one must study jet-triggered data and employ an algorithm to tag b-jets. For this analysis, an algorithm which uses information from a well-reconstructed secondary vertex is employed, which gives a purity of 99%. According to studies with QCD simulation, leptons which are reconstructed far away in $\eta - \phi$ space from a chosen tagged b-jet, i.e. with $\Delta R(\text{jet}, \ell) > 1$, have a 95% probability to originate from the other recoiling b-jet in the event. [7] The tagged b-jet constitutes the *tag* and the distant lepton constitutes the *probe* for this tag-and-probe method. A variety of data-driven measurements in many different contexts rely on tag-and-probe methods. The main advantage of such methods is that it allows one to study a desired observable (e.g., RelIso) by selecting a desired topology (in this case $b\bar{b}$ events) without biasing the measurement of the observable with any systematic uncertainties from the technique or algorithm used to select the events. For this study, it may seem natural to search near or within the b-tagged jet for a lepton, but this will certainly bias the RelIso measurement in some unknown way by convoluting the systematic uncertainties involved in the b-jet

---

[7] In roughly 5% of the cases the lepton will originate from an additional jet in the event from FSR, ISR, or multi-jet production.

tagging algorithm or the jet reconstruction algorithm. Instead, we use the knowledge that b-quarks are produced in pairs via QCD processes, so that from the tagging of one b-jet, one can infer the presence of a partner b-jet (usually pointed opposite in ϕ for di-jet events).

Events are required to have $H_T > 100$ GeV, which yields a p_T distribution of the partner b-jets that is very similar to b-jets in $t\bar{t}$ events. Alternatively, by requiring $H_T > 150$ or $H_T > 50$ GeV, the b-jets in this control sample become noticeably harder or softer with respect to the characteristic p_T scale of b-jets in $t\bar{t}$ production. Although the $H_T > 100$ GeV selection requirement greatly helps to unite the kinematics of b-jets in the control sample with that of $t\bar{t}$ production, the residual differences are still too large to ignore. A re-weighting procedure must be done to compensate for these remaining differences.

In order to re-weight the $b\bar{b}$ events, it is necessary to appeal to two other observables: the probe-lepton's transverse momentum, p_T, and the total jet multiplicity in the event, N_{jet}. The RelIso selection efficiency demonstrates a dependence on these two variables, which have very different spectra in QCD and $t\bar{t}$ events. However, for a given range in p_T and jet multiplicity, it is observed that the distributions of RelIso in QCD and $t\bar{t}$ are very similar. Therefore, the following measurements are needed to derive the prediction of $t\bar{t}$ events in the signal region in data:

(i) RelIso selection efficiencies, $\epsilon(i, j)$, where i and j represent bins in p_T and N_{jet} in b-tagged events.

(ii) Probability density function, $\omega(i, j)$, of finding a lepton with transverse momentum $p_T(i)$ from a b-jet in $t\bar{t}$ events with jet multiplicity, N_{jet}.

Both the muon momentum spectra from b-jets and the jet multiplicity are expected to be much better modeled in the Monte Carlo simulation than is the RelIso observable, so it is safe to calculate $\omega(i, j)$ using simulated $t\bar{t}$ events. A total selection efficiency can be

obtained for muons and electrons respectively, by multiplying these two quantities, i.e.,

$$< \varepsilon >^{(b)} = \sum_{i,j} \epsilon(i,j) \cdot \omega(i,j) \qquad (6\text{--}12)$$

In Figures 6-19A and 6-19B the final re-weighted RelIso templates for muons and electrons, as measured in the b-enriched control sample are shown. For comparison, the results obtained from re-weighting simulated QCD events is shown as well, along with the expected RelIso distribution from fake leptons in $t\bar{t}$ simulation. The level of agreement between the re-weighted QCD simulation and $t\bar{t}$ simulation constitutes a successful closure test of the method. It is not expected that the re-weighted data should match the RelIso distribution from $t\bar{t}$ simulation. As mentioned earlier, the simulation cannot be trusted to faithfully model the behavior of the RelIso observable for fake leptons. The RelIso selection efficiencies are explicitly stated in the text on the plots in Figures 6-19A and 6-19B, which represent the fraction of events in the first bin (of width 0.15). For muons the observed efficiency is $< \varepsilon >_{\mu}^{(b)} = 0.029^{+0.003}_{-0.002}$ while for electrons the observed efficiency is $< \varepsilon >_{e}^{(b)} = 0.036^{+0.013}_{-0.008}$. The uncertainties are statistical only.
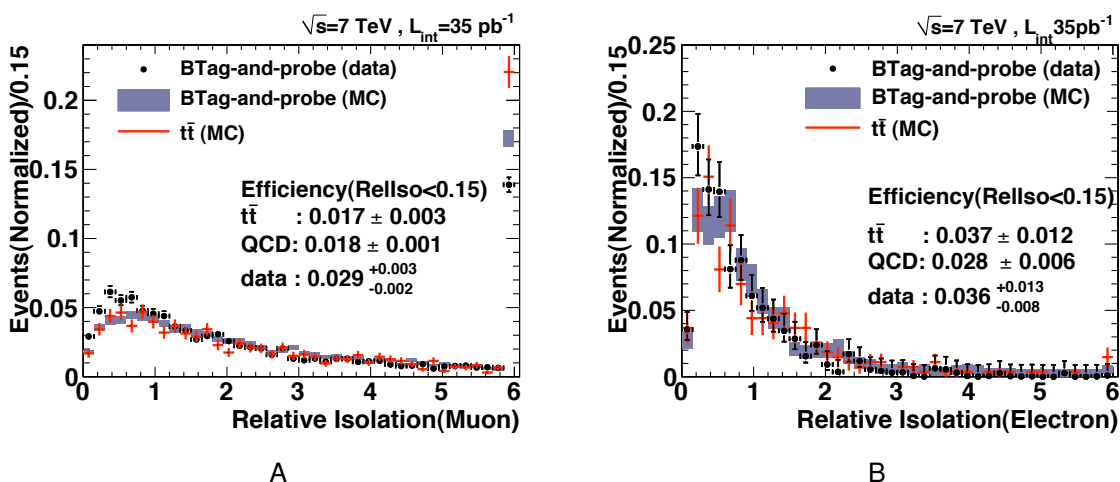

Figure 6-19. Final RelIso template for muons (left) and electrons (right).

To fully execute this data-driven background prediction in data, the analysis is performed by imposing all of the final selection criteria used in the signal search, with one exception. The RelIso requirement on the least isolated lepton is inverted and required to be above the nominal value 0.15. This semi-final selection will be referred to as the *sideband region*. The observed events are expected to be mostly from $t\bar{t}$ production (with a very small contribution from W+jets). There is also potentially a non-trivial contribution from the fake-fake backgrounds which were discussed in Section 6.6.3, but this can be subtracted from the sideband yields using the efficiencies derived for the fake-fake prediction. Before performing this subtraction in the data, the following numbers of same-sign di-lepton events are observed in the sideband: 11 $\mu\mu$, 2 ee, 6 $e\mu$, and 5 μe (the last lepton denotes the one that is least isolated).

After the fake-fake subtraction is performed, these sideband yields for each channel can be multiplied by the corresponding average probabilities to pass the RelIso requirement, which finally gives the data-driven prediction for the total number of prompt-fake di-leptons which populate the signal region: $N_{f-f}^{SS} = 0.52 \pm 0.24$ (stat) ± 0.26 (sys). This number represents the combination of all channels. The details of the calculation are provided in Table 6-16.

As indicated by the uncertainties given for N_{f-f}^{SS}, a few different sources of systematic error have been studied for the BTag-And-Probe measurement. The largest contribution comes from the statistical precision of the Monte-Carlo–based closure test. Another source of error is determined by evaluating how $<\varepsilon>^{(b)}$ changes in response to variations in the event selection conditions (e.g., $H_T > 150$ GeV or $H_T > 50$ GeV). This is found to be sub-dominant. An attempt is made to account for the unknown W+jets contamination in the sideband by artificially enhancing its Monte-Carlo–based expectation by a factor of two, and evaluating if the measured values of $<\varepsilon>^{(b)}$ deviates away from the value given by $t\bar{t}$ simulation. In a similar vein, tests were performed in simulation to check if an artificially enhanced fraction of fake leptons from sources other

than b-decays can lead to any significant variations in the measured value of $< \varepsilon >^{(b)}$. The contributions from all of these possible sources of systematic uncertainty are added in quadrature to arrive at a total systematic uncertainty on $< \varepsilon >^{(b)}$ of 54(29)% for electrons (muons).

Table 6-16. Data-driven background prediction of prompt-fake di-leptons.

Observable	$\mu\mu$	ee	$e\mu$	μe	total
Events in sideband	11 ± 3.3	2 ± 1.4	6 ± 2.2	5 ± 2.4	24 ± 4.9
f-f (sideband)	4.2 ± 2.2	0.3 ± 0.4	2.3 ± 2.5	0.7 ± 0.4	7.5 ± 4.5
p-f (sideband)	6.8 ± 4.2	1.7 ± 1.5	3.7 ± 3.6	4.3 ± 2.6	16.6 ± 6.4
p-f (signal region)	0.20 ± 0.14	0.06 ± 0.07	0.12 ± 0.11	0.16 ± 0.14	0.52 ± 0.35

6.6.5 Validation of the Background Composition in the Sideband Data

As a final check to illustrate that the composition of the background to this search is understood, one can attempt to account for the individual contributions to the sideband yields using Standard Model Monte Carlo samples combined with the data-driven prediction of the QCD backgrounds. Figure 6-20A shows the $\text{SM}_{\text{MC}}+\text{QCD}_{\text{data}}$ prediction for the sideband for each channel separately and combined. The actual yields in data are represented by black markers. The data and $\text{SM}_{\text{MC}}+\text{QCD}_{\text{data}}$ agree quite well. The Factorization method predicts that the QCD component (fake-fake) of the sideband should be $31\% \pm 19\%$. Figure 6-20B is meant to illustrate the same principle, but applied to the opposite-sign di-lepton topology. Here, the data-driven fake-fake measurement is performed on opposite-sign baseline selection yields, but with the RelIso and $\not{E}_{\text{T}}$ selection efficiencies derived from the same-sign di-lepton yields. Again, good agreement between data and $\text{SM}_{\text{MC}}+\text{QCD}_{\text{data}}$ is observed.

The Factorization method's classification of the backgrounds in the sideband can be further validated by appealing to another independent data-driven method, which can be referred to as the "d_0 Template Fitting method". This method exploits the differences in the d_0 spectra of prompt and non-prompt leptons. Again, it is assumed that the sideband yield is dominated by two topologies (i.e., "fake-fake" and "prompt-fake") as indicated by Table 6-16. These assumptions are summarized in Table 6-17. Relying
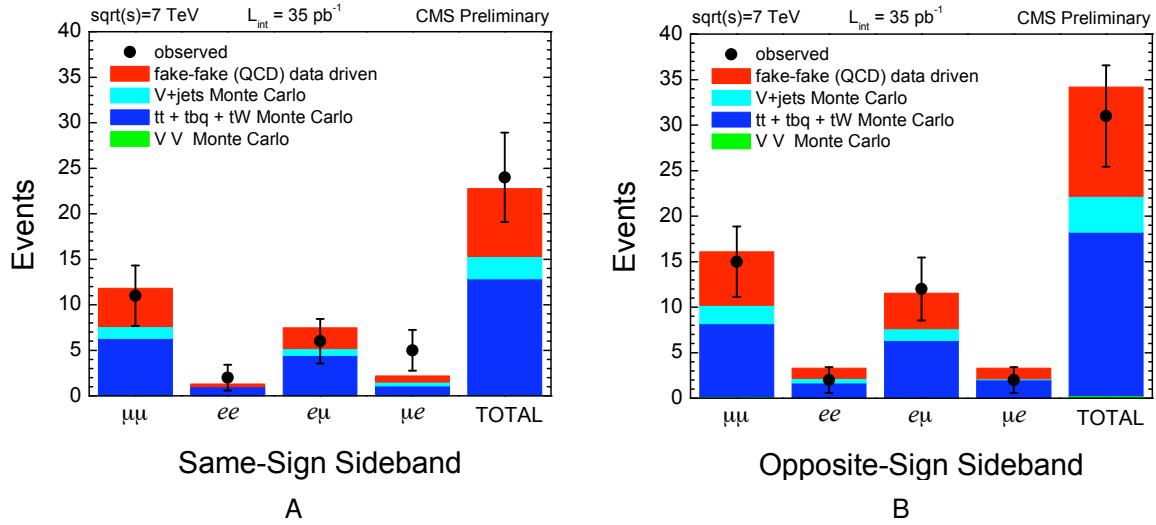
Figure 6-20. Summary of background contributions for sideband events in data and simulation shown for the same-sign di-lepton topology (left) and the opposite-sign di-lepton topology (right). Here, the cut on the least isolated lepton is relaxed.

on this well-motivated assumption, the d_0 requirement is completely relaxed on the isolated lepton in the di-lepton pair. Then, two d_0 templates must be derived from data. One template is meant to model the d_0 spectrum for prompt leptons and is taken from a Z control region in data. The other template is meant to model the d_0 spectrum for non-prompt leptons and is taken from a QCD control region in data. The selection requirements used to define these two control regions are provided in Table 6-18.

Table 6-17. Topologies present in the sideband

Isolated Lepton	Non-isolated Lepton	Proportion
Prompt	Prompt	negligible
Prompt	Fake	α
Fake	Prompt	negligible
Fake	Fake	$1 - \alpha$

Before deriving the templates a few issues must be addressed. In particular, one must determine whether or not the precision and accuracy of the d_0 observable is sufficient when it is measured with respect to the beamspot (as is done throughout the rest of this analysis) versus some other reference point, like the event reconstructed

Table 6-18. Control regions for the d_0 Template Fitting method

Observable	Z-Control	QCD-Control
Leptons	2 with opposite-sign	≥ 1
RelIso	< 0.15	> 0.4
Mass [GeV]	$\in [76, 106]$	$\in [5, 76]$ or $\in [106, \infty]$
H_T [GeV]	> 100	> 300
$\not{E}_T$ [GeV]	< 20	< 20

primary vertex, which is chosen simply as the one with the most degrees of freedom (i.e., most tracks emerging from it) in the case of multiple pile-up events. Figure 6-21 shows the d_0 spectra for these two choices in the Z control region (left) and the QCD control region (right). For the former, is clear that the primary vertex gives a more δ-like function, which is desirable, while for the latter a softer spectrum is observed in the core, which is undesirable. The trade-off does not seem to merit a switch to the primary vertex here. Thus, it is justified to continue to take the measurement from the beamspot, which is common on CMS.
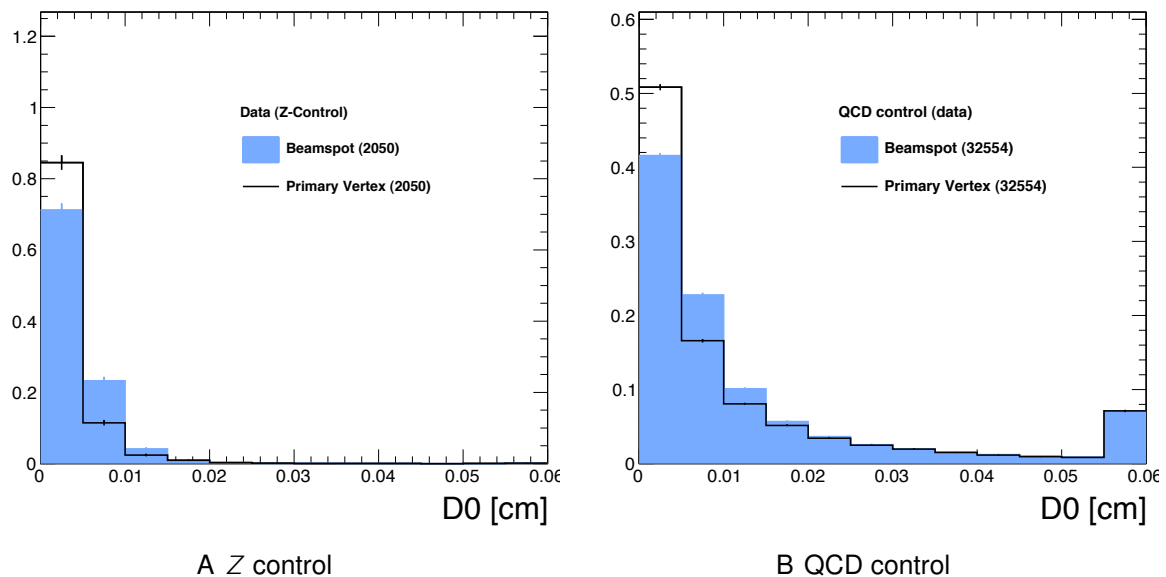

A Z control

B QCD control

Figure 6-21. The distribution of d_0 measured from the beamspot (blue) and measured from the reconstructed primary vertex (black) for the Z-control region (left) and the QCD control region (right).

Another detail that cannot be overlooked is the slight difference in d_0 spectra between fake muons and fake electrons. This is shown in Figure 6-22. As discussed in Section 6.6.3, in heavy-flavor decays electrons are less likely to be reconstructed than muons. Thus, the tail of the distribution for fake electrons is milder. Differences between prompt muons and prompt electrons are shown to be negligible. In the ideal case it would be desirable to avoid combining electrons and muons into a common d_0 template and simply perform two separate fits on the sideband data (one for isolated electrons and one for isolated muons); however, the sideband data is too statistically limited to perform such a treatment. As an alternative, it is enough to simply derive the templates for electrons and muons individually and then combine them into a single template in proportion to the electron:muon ratio in the sideband. The electron:muon ratio in the sideband, once the d_0 cut is relaxed, proves to be $1 : 2$.
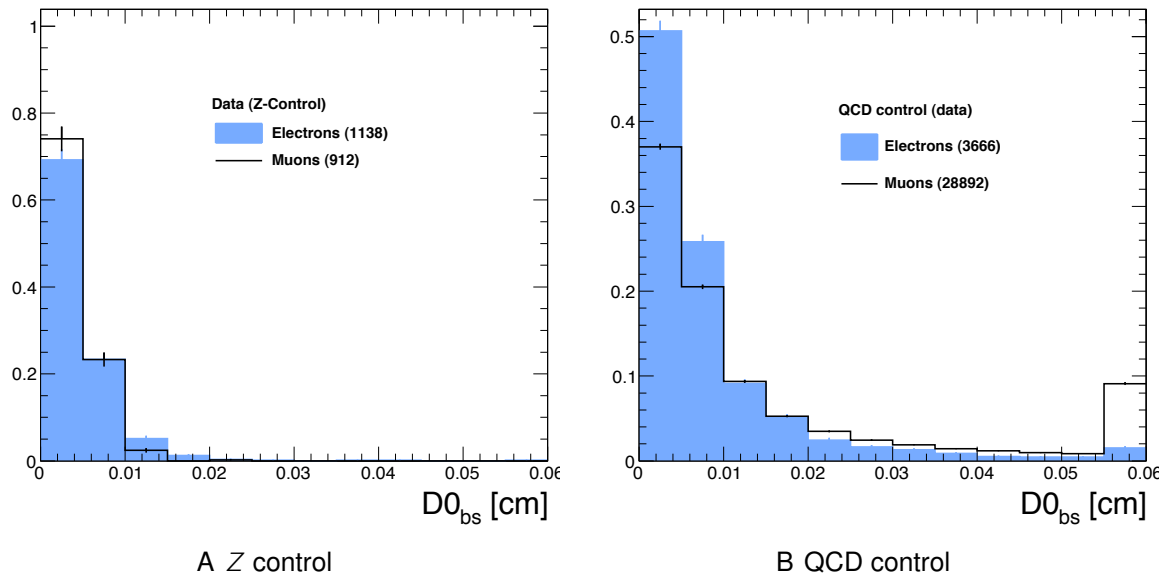

A Z control   B QCD control

Figure 6-22. The distribution of d_0 for electrons (blue) and muons (black) for the Z control region (left) and the QCD control region (right).

Once respective templates for prompt and non-prompt leptons are derived, they can be added together with weights α and $1 - \alpha$, which are optimized via a binned maximum-likelihood fit to the d_0 spectrum of the isolated lepton in the sideband data.

Figure 6-23A shows the prompt and non-prompt templates normalized to unity on overlaid with the data, which is also normalized to unity. The extended tail is clearly visible for non-prompt leptons. Figure 6-23B shows the same plot, but now the templates are scaled to best fit the data. The maximum likelihood fit yields a value of $\alpha = 0.51 \pm 0.24$, which represents the proportion of events attributable to the "prompt-fake" topology. The proportion of events attributable to the "fake-fake" topology is therefore $1 - \alpha = 0.49 \pm 0.24$. The value of $-2\ln(\text{likelihood})$ is plotted as a function of α in Figure 6-23C.

In order to compare with the results from the Factorization method the value of $1 - \alpha$ must be adjusted to the value it would be with the d_0 requirement restored to its nominal value of 0.2 mm. This can be done if one knows the d_0 selection efficiencies for prompt and non-prompt leptons, respectively. Fortunately, this can be measured these directly from the templates, which gives $\varepsilon_{d_0} = 80.2\%(100\%)$ for non-prompt (prompt) leptons. Thus, the "fake-fake" contribution to the sideband $\varepsilon_{d_0} \cdot (1 - \alpha)/(\varepsilon_{d_0} \cdot (1 - \alpha) + \alpha)) = 0.43 \pm 0.25$, which is statistically consistent with the prediction from the Factorization method.
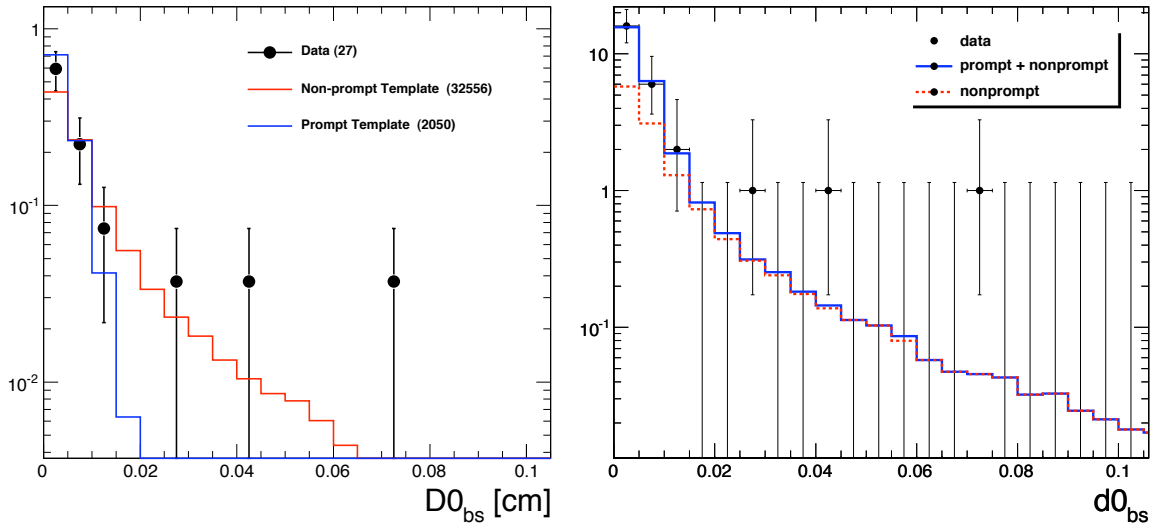
A Templates (before fit)

B Templates (after fit)
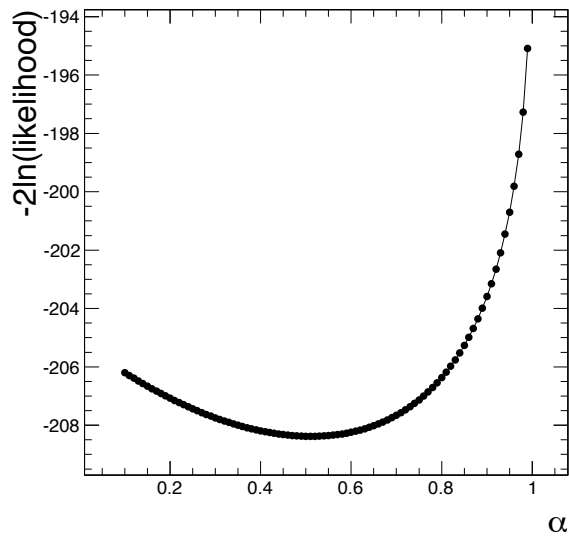
C $-2ln$(likelihood) vs. α

Figure 6-23. Prompt (blue) and non-prompt (red) templates normalized to unity on top of data (top-left). The same templates scaled by weights which were optimized by a maximum likelihood fit (top-right). The value of $-2\ln$(likelihood) as a function of α (bottom).

6.6.6 Summary of Background Rates

Table 6-21 and Figure 6-24 summarize the expected event yields for all background contributions. We can now re-write Eq. 6–2 in all of its detail. This is done in Eq. 6–13 where the dependence of the prompt-fake measurement on the efficiencies derived for the fake-fake measurement is clearly illustrated.

$$
\begin{aligned}
N_{bgd}^{tot} \;=\;& N_{p-p}^{SS} + N_{p-p}^{OS} + \\[4pt]
& N_{\mu\mu}^{\text{baseline}} \cdot \varepsilon_\mu \cdot \varepsilon_\mu \cdot \varepsilon_{\not{E}_T} + \\[4pt]
& N_{e\mu}^{\text{baseline}} \cdot \varepsilon_\mu \cdot \varepsilon_e \cdot \varepsilon_{\not{E}_T} + \\[4pt]
& N_{ee}^{\text{baseline}} \cdot \varepsilon_e \cdot \varepsilon_e \cdot \varepsilon_{\not{E}_T} + \\[4pt]
& (N_{\mu\mu}^{\text{sideband}} - N_{\mu\mu}^{\text{baseline}} \cdot \varepsilon_\mu \cdot (1 - \varepsilon_\mu) \cdot \varepsilon_{\not{E}_T}) \cdot <\varepsilon>_\mu^{(b)} + \\[4pt]
& (N_{e\mu}^{\text{sideband}} - N_{e\mu+\mu e}^{\text{baseline}} \cdot \varepsilon_e \cdot (1 - \varepsilon_\mu) \cdot \varepsilon_{\not{E}_T}) \cdot <\varepsilon>_\mu^{(b)} + \\[4pt]
& (N_{\mu e}^{\text{sideband}} - N_{e\mu+\mu e}^{\text{baseline}} \cdot \varepsilon_\mu \cdot (1 - \varepsilon_e) \cdot \varepsilon_{\not{E}_T}) \cdot <\varepsilon>_e^{(b)} + \\[4pt]
& (N_{ee}^{\text{sideband}} - N_{ee}^{\text{baseline}} \cdot \varepsilon_e \cdot (1 - \varepsilon_e) \cdot \varepsilon_{\not{E}_T}) \cdot <\varepsilon>_e^{(b)}
\end{aligned}
\tag{6–13}
$$

The algebraic expression for N_{bgd}^{tot} given in Eq. 6–13 helps to guide the error propagation. The calculation is performed by varying this expression separately for each source of uncertainty. Table 6-19 shows the absolute statistical uncertainty for each term in the expression as well as its absolute variation on the total background estimate N_{bgd}^{tot}. Table 6-20 summarizes systematic uncertainties for the respective measurements and their respective impacts on the total background estimate. It should be emphasized that the errors are in most cases dominated by the low statistics of the events in the control samples; hence, in the future they are expected to scale with luminosity as $1/\sqrt{\int L \, dt}$.

Table 6-19. Statistical errors of terms used in the calculation of N^{tot}_{bgd}

Term	δ(Term)	$\delta(N^{tot}_{bgd})$
N^{OS}_{p-p}	0.006	0.006
$N^{\text{baseline}}_{\mu\mu}$	14.93	< 0.01
N^{baseline}_{ee}	3.28	< 0.01
$N^{\text{baseline}}_{e\mu}$	8.83	< 0.01
$N^{\text{sideband}}_{\mu\mu}$	3.32	0.10
N^{sideband}_{ee}	1.41	0.05
$N^{\text{sideband}}_{\mu e}$	2.24	0.08
$N^{\text{sideband}}_{e\mu}$	2.45	0.07
ε_μ	0.015	0.03
ε_e	0.077	0.03
$\varepsilon_{\not{E}_T}$	0.028	< 0.01
$<\varepsilon>^{(b)}_\mu$	0.003	0.03
$<\varepsilon>^{(b)}_e$	0.013	0.08

Table 6-20. Systematic errors involved in calculation of N^{tot}_{bgd}

Source	$\delta(N^{tot}_{bgd})$
Uncertainty on N^{SS}_{p-p}	0.041
Biases due to f-p contamination in N^{baseline} , ε_μ , ε_e , $\varepsilon_{\not{E}_T}$	0.02
Uncertainty on closure test for N_{f-f}	0.05
Uncertainties on BTag-and-Probe $<\varepsilon>^{(b)}$	0.21
Uncertainty on W+jets component in N_{p-f}	0.15

Table 6-21. Summary of event yields for all background sources and assigned systematic errors.

| Phenomenological Sorting	$\mu\mu$	ee	$e\mu$	total	comments
Prompt-Prompt same-sign di-leptons	0.026	0.012	0.044	0.083	theory + simulation
$qq \rightarrow q'q'W^{\pm}W^{\pm}$, $2 \times (q\bar{q} \rightarrow W^{\pm})$, WZ, ZZ	$\pm$0.013	$\pm$0.006	$\pm$0.022	$\pm$0.041	
Prompt-Prompt opposite-sign di-leptons with a charge flip	-	0.008	0.004	0.012	fully data-driven
($t\bar{t}$, tW, WW)	-	$\pm$0.005	$\pm$0.003	$\pm$0.006	
Prompt-fake same-sign di-leptons	0.197	0.060	0.264	0.522	fully data-driven
($t\bar{t}$, tX, $W + jets$)	$\pm$0.136	$\pm$0.067	$\pm$0.110	$\pm$0.354	
Fake-fake same-sign di-leptons	0.078	0.020	0.084	0.183	fully data-driven
(QCD, all-hadronic $t\bar{t}$)	$\pm$0.060	$\pm$0.028	$\pm$0.042	$\pm$0.169	
Total background estimate (as to be used in the analysis)	0.30	0.10	0.40	0.80	mostly data-driven
	$\pm$0.13	$\pm$0.07	$\pm$0.18	$\pm$0.33	
Total background as predicted by simulation (without QCD)	(0.16)	(0.05)	(0.21)	(0.41)	for comparison only
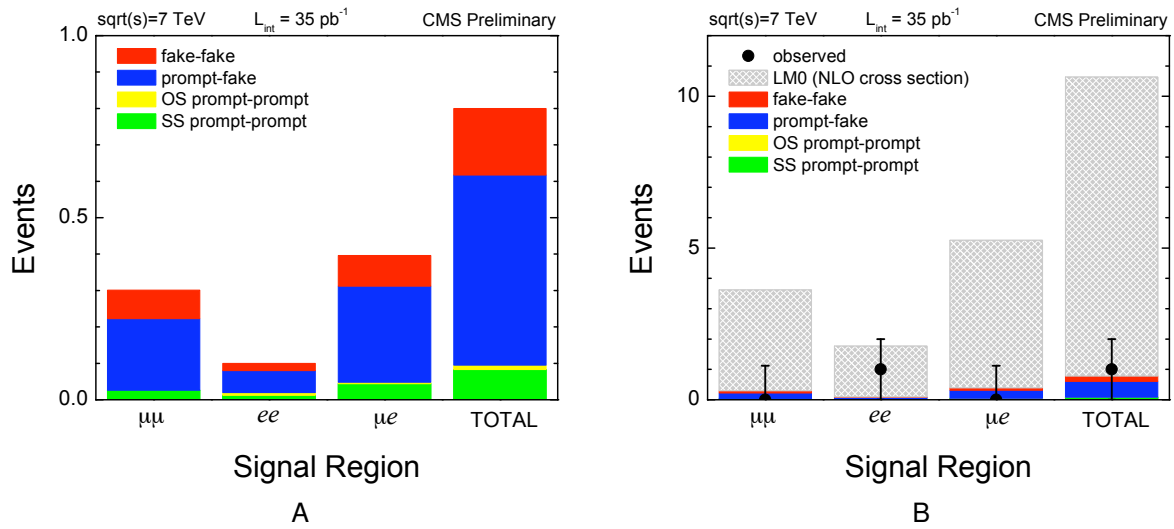
Figure 6-24. Final predictions for the expected event rates at 35 pb^{-1} (left) and with LM0 included (right). All predictions except for $qqWW + WZ + ZZ$ are fully data-driven.

6.7   Signal yield and uncertainties

Before proceeding with the discussion of systematic errors associated with the signal event yield, it is important not to entangle two distinct goals: One may pursue the goal of exploring one (or a set of) fully defined model(s) (e.g. mSUGRA with some set of parameters). Setting limits in this case is reduced to a yes or no answer for a given set of the model parameters. The theoretical uncertainties on the model itself would influence one's judgment on whether or not the model (or some range of model parameters) can be excluded. Alternatively, given the enormous range of free parameters in the unconstrained MSSM, scanning over a very constrained subset of parameters (e.g. mSUGRA) may not yield a satisfactory or reliable result. Thus, one may want to present search results as model-independent limits on the product of the cross section (σ), branching ratios (BR), and the experimental acceptance (A). This is certainly a very attractive option; however, it requires stating certain disclaimers on which models can and cannot be tried against such generically stated limits. The main concern here is that the experimental reconstruction of a particular observable is not always constant and has a finite resolution. This leads to the fact that the acceptance for a particular signal is not a universal quantity and depends on the actual distributions of the prime observables in the model.

Systematic errors will be discussed in the context of these two approaches. The model-dependent systematic errors will be illustrated on the example of the LM0 benchmark point. In order to make the limit on $\sigma \times BR \times A$ applicable to any model, it is necessary to provide the parameterized acceptance functions for all observables used in the analysis.

6.7.1   Theoretical Uncertainties

These uncertainties are applicable only for setting limits on a concrete model with a given set of parameters. The main contributions to theoretical uncertainties (once

all model parameters are fixed) are associated with the scale of the QCD coupling (Section 2.1.3) and the proton parton density functions (*pdf*'s).

For gluino/squark production in mSUGRA models, the *pdf* uncertainties translate to about a $10 - 13\%$ systematic error on the cross-sections [73]. The cited range covers the energy scale from 2 TeV (Tevatron) to 14 TeV (LHC). This analysis will apply a 13% uncertainty in order to be conservative.

The systematic errors of the cross-section arising from QCD scale variations depend very strongly on the energy of collisions. At the NLO level calculations, they were estimated to range from $40 - 50\%$ at the Tevatron to $5 - 10\%$ at 14 TeV LHC [73]. The 7 TeV collision energy used in the 2010 LHC run falls right in between; hence, it is necessary to evaluate the mSUGRA cross-section sensitivity to renormalization and factorization scales used in the pQCD calculations [62] by varying them by a factor of 2 up and down, which over the last few years has become a common convention. Thus, the uncertainty obtained for the LM0 benchmark point is 18%, which is consistent with the expectation given the numbers mentioned above.

6.7.2   Instrumental Uncertainties

6.7.2.1   Luminosity

The current uncertainty on the integrated luminosity in CMS is 11% [74], which is measured by the method of "zero-counting" using the HF calorimeter.

6.7.2.2   Muon selection efficiencies and validation

The muon reconstruction efficiency as obtained from Monte Carlo simulation is shown in Figure 6-25. The results are shown as a function of p_T of the simulated muon for the barrel and endcap muon systems, respectively. The muon reconstruction efficiency, as derived from data using the classical Tag-and-Probe method using J/ψ and Z events, is consistent with the Monte Carlo modeling at a level better than 5% [66]. Also shown in Figure 6-25 are curves (blue) which are fit to the points. The functional

form used for the fits relies on three parameters and is given by:

$$\epsilon(p_T^\mu) = \mathrm{par}(1) + \mathrm{par}(2) \cdot \left(\mathrm{erf}\left(\frac{p_T^\mu - p_T^{\mu,\mathrm{thresh}}}{\mathrm{par}(3)} \right) - 1 \right) \qquad (6\text{–}14)$$

where $p_T^{\mu,\mathrm{thresh}}$ represents the muon p_T threshold of 5 GeV used in this analysis.

The $\mathrm{RelIso}(\mu)$ selection efficiencies for LM0 events are shown in Figure 6-26 as a function of the p_T of the reconstructed muon for the barrel and endcap muon systems, respectively. The blue curves represent fits based on the formula given in Eq. 6–14. It should be noted that the selection efficiency for prompt muons in LM0 events is generally lower than it is for prompt muons coming from $Z \rightarrow \mu\mu$ events of the Standard Model. This is due to the increased presence of hadronic activity in SUSY events featuring colored production. Prompt leptons in such events can overlap with jets from other parts of the cascade decays by accident, thus giving the appearance of a non-isolated, and hence non-prompt lepton. Figure 6-27 shows the product of the reconstruction and RelIso selection efficiencies with similar fits performed.

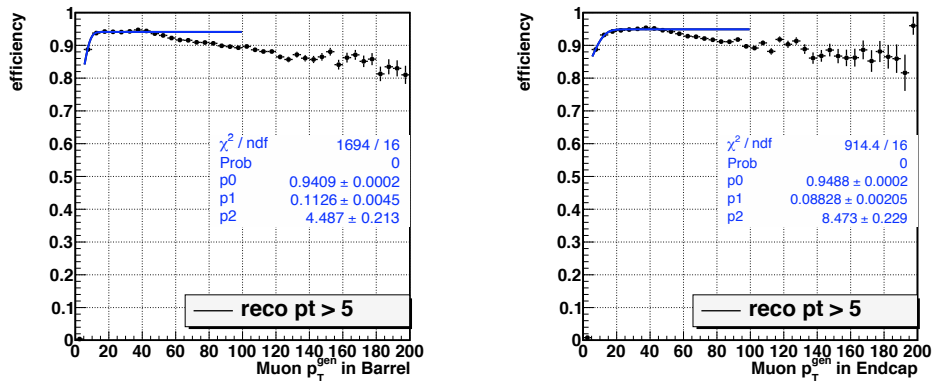Figure 6-25. Muon reconstruction efficiency versus simulated muon p_T with $|\eta| < 1.2$ (left) and $1.2 < |\eta| < 2.4$ (right). The reconstructed muon is required to have $p_T^{\mathrm{reco}} > 5$ GeV.

It is important to note that the traditional Tag-and-Probe method which is used to measure RelIso selection efficiencies in a data-driven way is not applicable to SUSY
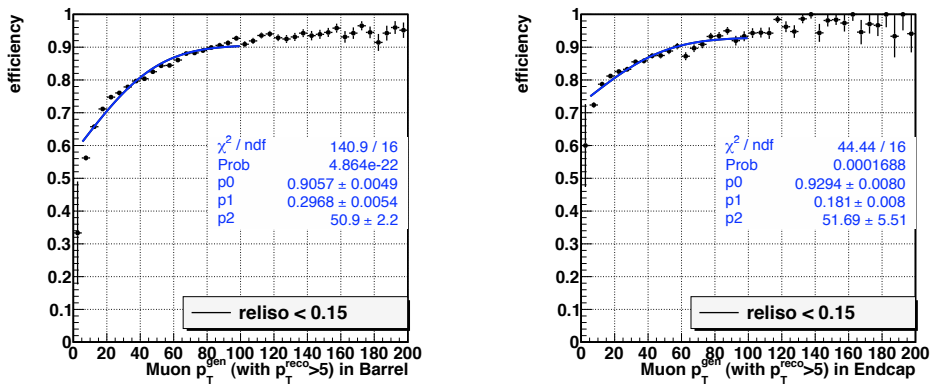
Figure 6-26. $\mathrm{RelIso}(\mu)$ selection efficiency for reconstructed muons versus p_T for $|\eta| < 1.2$ (left) and $1.2 < |\eta| < 2.4$ (right).
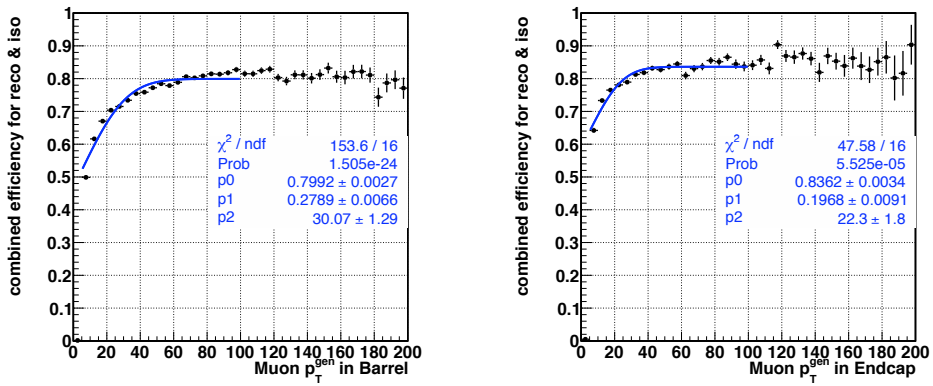

Figure 6-27. Product of muon reconstruction and RelIso selection efficiencies versus p_T for $|\eta| < 1.2$ (left) and $1.2 < |\eta| < 2.4$ (right).

for at least two reasons. First, leptons from SUSY production, although prompt, may nevertheless be much softer than those in Z and W decays. The p_T spectrum of leptons in the process will definitely be important if one uses the RelIso variable to select events. Second, leptons from SUSY production, live in a substantially busier hadronic environment than leptons in Z and W decays. Such intense hadronic energy flow, inherent to the processes being searched for, will certainly have a detrimental effect on the performance of the RelIso selection efficiency.

To evaluate the $\mathrm{RelIso}(\mu)$ selection efficiency for LM0-like prompt muons in the LM0-like multi-jet environment, the method of Lepton Kinematic Templates (LKT) is used, which was designed for evaluating a RelIso selection efficiency for events with multiple prompt leptons from an arbitrary momentum spectrum and with an arbitrarily dense jet activity. The method naturally takes into account kinematic correlations between multiple muons in signal events. The LKT method was first introduced in [66] and was used in the first W/Z cross-section measurements on CMS [75].

In brief, the LKT method can be described as follows: $Z \rightarrow \mu\mu$ events are selected from data and random isolation cones in $\eta - \phi$ space are thrown at regions in the detector. Then, the 3-momenta of n leptons from simulated signal events are sampled and combined with the activity inside the random isolation cone to perform the RelIso calculation. The value n can vary on an event by event basis and should also be sampled from the signal model under study. Next, the selection efficiency per event (not per lepton) for different values (bins) of hadronic activity in Z-events is measured. The number of charged tracks in the event is used as a convenient measure of the hadronic activity. Finally, the measured efficiencies in bins of hadronic activity are re-weighted to match the hadronic activity distribution expected in the signal under the study.

Figure 6-28 (left) shows the track multiplicity distribution for $Z \rightarrow \mu\mu$ events in simulation (red line) and data (blue points). The same distribution from LM0 (black dashed line) is also shown. The difference in hadronic activity between the two processes is reflected in the separation of the curves. Figure 6-28 (right) shows the LKT method applied to the LM0 benchmark point. The red points show the $\mathrm{RelIso}(\mu)$ selection efficiency for LM0-like LKT's thrown in simulated $Z \rightarrow \mu\mu$ events. The blue points show the same distribution for $Z \rightarrow \mu\mu$ events in data. One can clearly see the strong linear dependence of the $\mathrm{RelIso}(\mu)$ selection efficiency on the level of hadronic activity in Z events for both simulation and data. The black crosses show the $\mathrm{RelIso}(\mu)$ selection efficiency in the LM0 benchmark sample after all of the other

final selection requirements have been applied. The single hollow-squared marker represents the average selection efficiency for LM0 according to simulation. It is evident that the measurements done with Z events can be linearly extrapolated using the track multiplicity to match the RelIso selection efficiency in the context of a busier environment which is characteristic of a SUSY process. This constitutes the closure test of the LKT method. Therefore, the simulation can be trusted to faithfully model the RelIso selection efficiency for prompt, signal-like leptons in a busy hadronic environment. The variations between the LM0 RelIso selection efficiency and extrapolations using Z events either from simulation or from data gives a measure of a possible systematic error of about 3%.
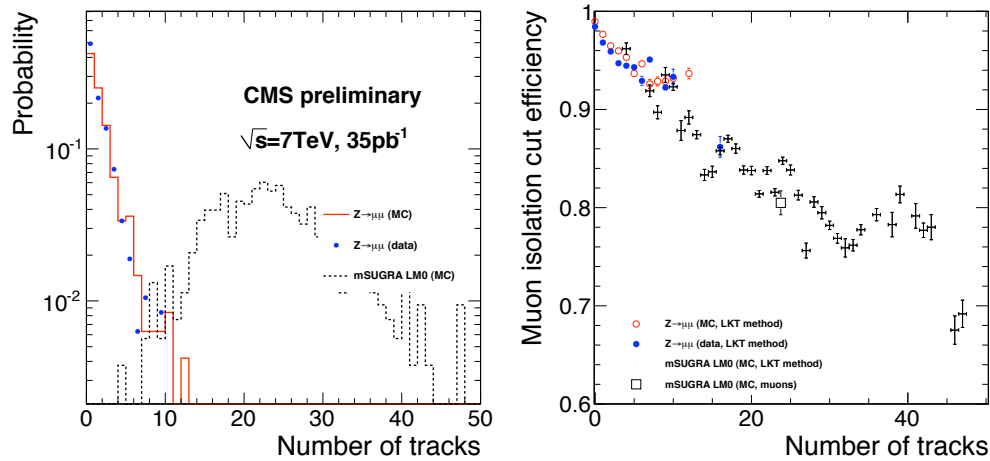

Figure 6-28. Distributions of number of tracks in simulated $Z \rightarrow \mu\mu$ events (red), data (blue), and in LM0 events (black) (left). Prediction of $\mathrm{RelIso}(\mu)$ selection efficiency for LM0 events obtained by extrapolation of measurements done with simulated Z events (right).

6.7.2.3 Electron selection efficiencies and validation

The electron reconstruction and $\mathrm{RelIso}(e)$ selection efficiencies as obtained from simulation are shown in Figures 6-29 and 6-30, respectively, while the product of the two are shown in Figure 6-31. The functional form given in Eq . 6–14 is used to fit a curve (blue) to each efficiency distribution. Here, $p_T^{e,\mathrm{thresh}}$ represents the electron p_T

threshold of 10 GeV that is used for this analysis. The parameters for the fits performed on the combined efficiencies are given in Section 6.7.3.

Electrons suffer from significantly more sources of reconstruction inefficiencies, than muons do. Muons pass through matter much more easily, owing to their minimum-ionizing nature, and as a consequence are less likely to have destructive interactions which could jeopardize their measurements. The faithful simulation of an electron's passage through the detector material is consequently much more difficult to achieve. Thus, relying on the reconstruction efficiency from simulation must be done with care. To evaluate the sensitivity of the LM0 signal event yield to the possible uncertainties in the electron reconstruction efficiency, a re-weighting procedure is performed on all simulated events containing reconstructed electrons according to possible variations from the expected efficiency. The observed yields of LM0 events are observed to vary by $\pm 8\%$ as a result of this test.
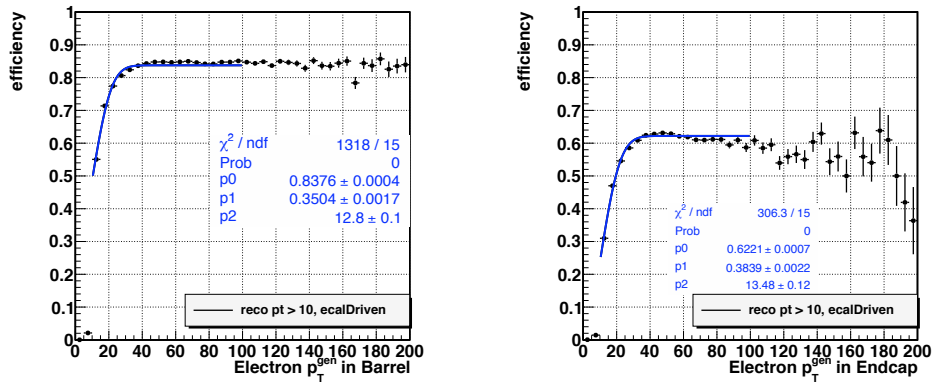

Figure 6-29. Electron reconstruction efficiency versus simulated electron p_T for $|\eta| < 1.5$ (left) and $1.5 < |\eta| < 2.4$ (right). The reconstructed electron is required to have $p_T^{reco} > 10$ GeV.

To validate the full electron selection efficiency, it is convenient to exploit the previously observed agreement between data and simulation for the selection efficiency of muons. Since the expected rates of $Z \rightarrow \mu\mu$ and $Z \rightarrow ee$ events are the same, it
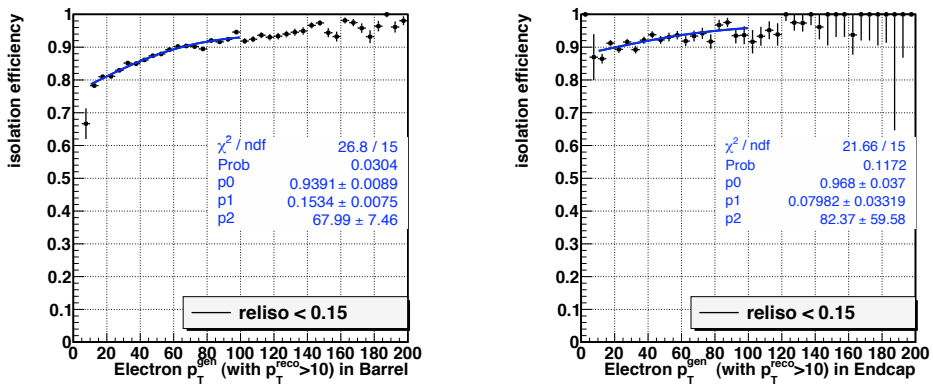
Figure 6-30. $\mathrm{RelIso}(e)$ selection efficiency versus p_T for $|\eta| < 1.5$ (left) and $1.5 < |\eta| < 2.4$ (right).
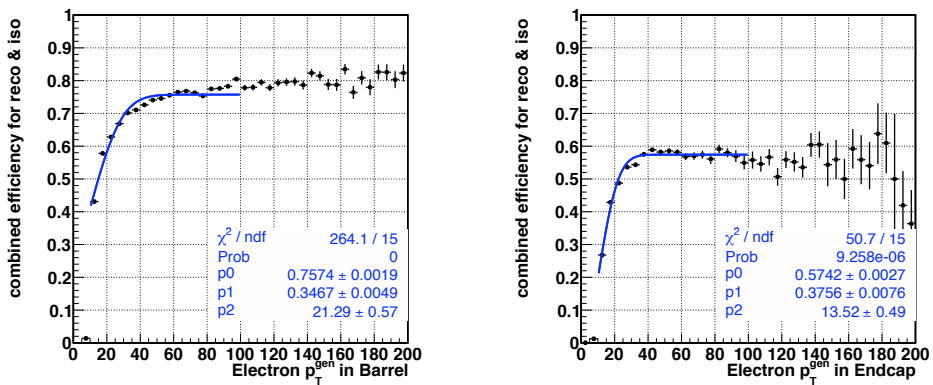

Figure 6-31. Product of electron reconstruction and $\mathrm{RelIso}(e)$ selection efficiencies versus p_T for $|\eta| < 1.5$ (left) and $1.5 < |\eta| < 2.4$ (right).

is sufficient to compare the ratios of electron and muon yields in data and simulation using Z events. Figure 6-32 shows such ratios with all electron identification and RelIso selection requirements applied. Electrons and muons used for these plots are taken from di-electron and di-muon events that agree with the Z boson decay hypothesis: $|m_{e^+e^-} - m_Z| < 30$ GeV. The purity of such a selection is very high. One can see that e-to-μ ratios in data and simulation agree to within 5%, which gives a measure of

possible systematic errors in the modeling of the electron reconstruction, identification, and RelIso performance.
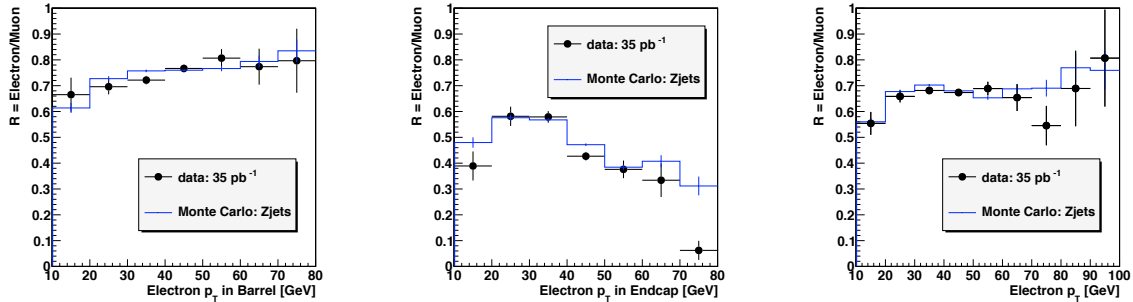

Figure 6-32. Ratios of electron and muon yields (data and simulation) in p_T bins for events with di-electrons and di-muons within the Z-peak for the ECAL barrel (left), ECAL endcap (middle), and combined (right).

6.7.2.4 H_T and $\not{E}_T$ selection efficiencies

Figure 6-33 (left) demonstrates that the reconstructed H_T^{reco} is not expected to have any offsets with respect to the true (generator-level) value of H_T^{gen} formed by the scalar p_T sum of the outgoing partons in the hard-scatter[8] . This agreement is expected in principle once the jet energy scale (JES) is properly calibrated. Figure 6-33 (right) shows the probability of reconstructing H_T^{reco} with a value of 300 GeV or higher as a function of the generator-level value H_T^{gen}. Similar distributions are shown in Figure 6-34 for the $\not{E}_T$ observable[9] .

Figure 6-35 illustrates the difference between the reconstructed and generator-level H_T (left) and $\not{E}_T$ (right) observables. These distributions are fit with a Guassian curve to demonstrate the effect of the finite detector resolution. The resulting standard deviations

---

[8] The generator-level H_T^{gen} is built from "stable" (status=1) generator particles provided in the Monte Carlo truth.

[9] The generator-level $\not{E}_T$ is calculated from the stable particles provided in the Monte Carlo truth which would be visible to the CMS detector.
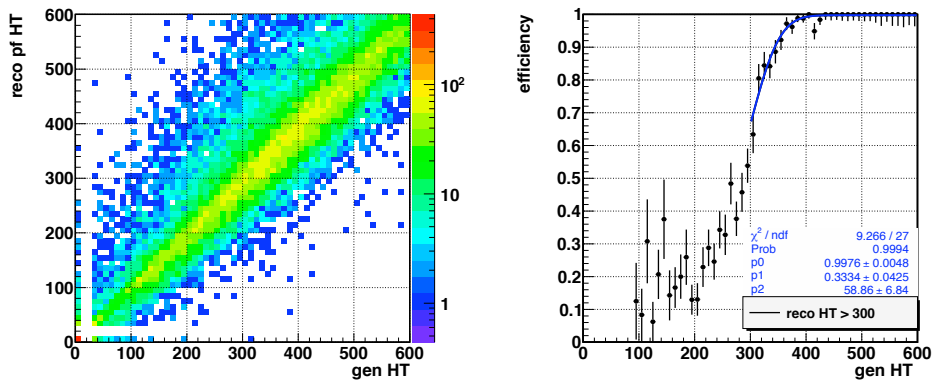
Figure 6-33. Reconstructed H_T^{reco} vs. generator-level H_T^{gen} (left). Probability of reconstructing an event with $H_T > 300$ GeV for a given H_T at the generator level (right).
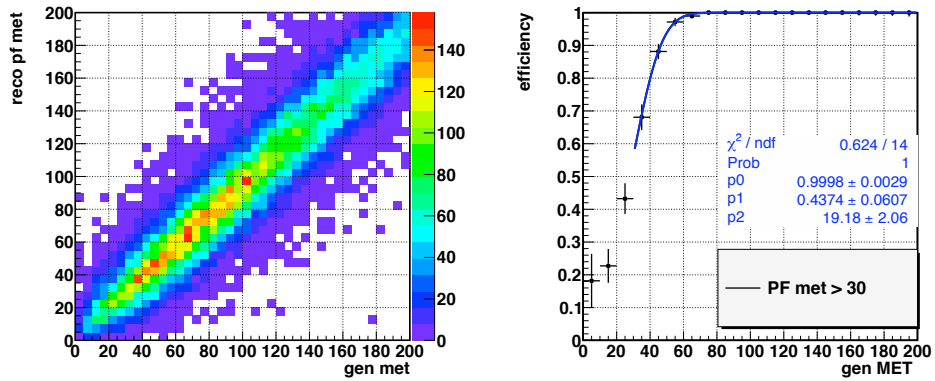

Figure 6-34. Reconstructed $\not{E}_T^{reco}$ vs. generator-level $\not{E}_T^{gen}$ (left). Probability of reconstructing an event with $\not{E}_T > 30$ GeV for a given $\not{E}_T$ at the generator level (right).

(σ_{H_T} and $\sigma_{\not{E}_T}$) of these Gaussian fits can be used for smearing the true values of these observables given by the Monte Carlo truth, in order to model the response of the CMS detector.

Systematic errors on the efficiencies of the H_T and $\not{E}_T$ selection requirements are strongly correlated and are thus evaluated on simply the combined selection efficiency of the two. To evaluate the systematic error due to uncertainties in the jet energy scale,
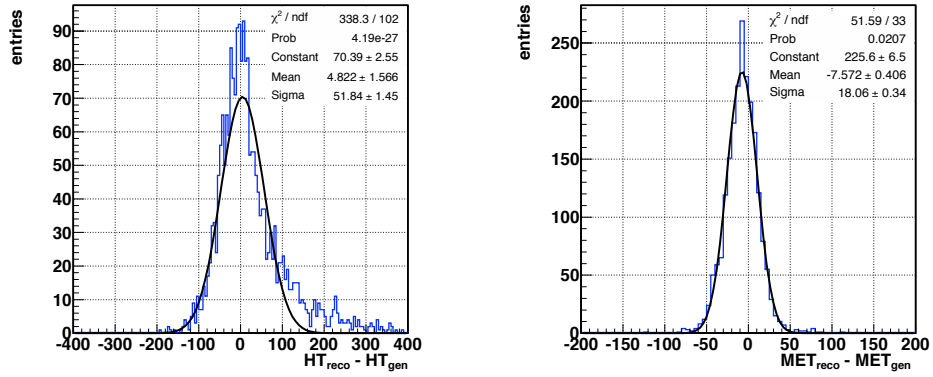
Figure 6-35. Distributions of $H_T^{reco} - H_T^{gen}$ for events with $H_T^{gen} > 300\,GeV$ (left) and $\slashed{E}_T^{reco} - \slashed{E}_T^{gen}$ for events with $H_T^{gen} > 300\,GeV$ and $\slashed{E}_T^{gen} > 30\,GeV$ (right).

the LM0 sample is used to vary simultaneously the energies of all jets and $\slashed{E}_T$ (after subtracting the contribution from leptons) by $\pm 5\%$. The observed change in the event yields after applying the $H_T > 300$ GeV, $N_{jets} \geq 2$, and $\slashed{E}_T > 30$ GeV requirements is $+4.4\%$ and -7.5%, respectively. An overall systematic error of $\pm 8\%$ is thus applied to the H_T and $\slashed{E}_T$ selection requirements.

6.7.2.5 Trigger efficiency

The H_T trigger efficiencies are measured directly from data using events recorded via a muon trigger path, which is assumed to be orthogonal. Muons do not influence the H_T trigger, since they interact only minimally with the calorimeters and, hence, do not bias the measurement. Figure 6-36 shows the H_T trigger efficiencies for events with a given H_T reconstructed offline. More details can be found in Table 6-22. One can see that events with $H_T > 300$ GeV reconstructed offline pass the H_T triggers used in this analysis with nearly 100% efficiency. The systematic errors on the trigger efficiency measurements are driven by the statistics of the measurement. Based on Figure 6-36, a conservative 5% error is assigned.
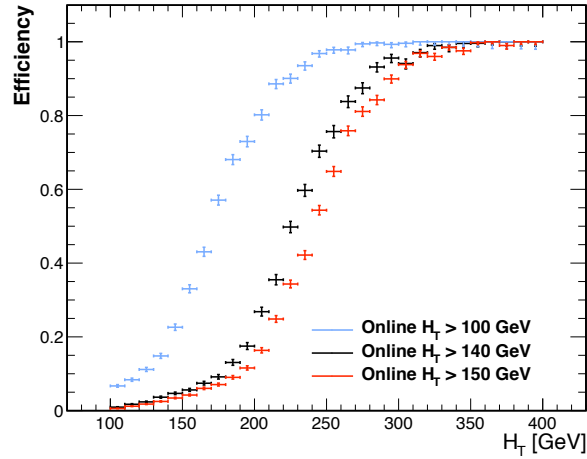
Figure 6-36. H_T trigger efficiency vs reconstructed H_T. The efficiency is measured using data obtained with muon triggers.

Table 6-22. H_T trigger efficiencies for the data set used in the analysis.

Triggers used during different running periods	HT100U	HT140U	HT150U
Integrated luminosity recorded/used (pb^{-1})	7.4	9.5	17.8
Efficiency of individual triggers	100%	95%	90%

6.7.2.6 Crosschecks

To validate that the final selection efficiencies are understood for events featuring two same-sign prompt leptons, $H_T > 300$ GeV, and $\not{E}_T > 30$ GeV, the analysis is repeated for opposite-sign di-lepton events with the exact same final selection requirements. In total, 20 events are observed (8 $\mu^\pm\mu^\mp$, 6 $e^\pm e^\mp$, and 6 $\mu^\pm e^\mp$), which are in reasonable agreement with the expected background (about 14 events). The opposite-sign di-lepton topology is expected to be dominated by $t\bar{t}$ events with two prompt leptons. This cross-check further validates the final selection efficiency for signal-like events.

6.7.3 Summary: Signal Acceptance and Uncertainties

In order to construct an upper limit on $\sigma \times BR \times A^{\text{experiment}}$, which is applicable to a wide range of models, it is necessary to provide parameterizations that can allow one to calculate the experimental acceptance for any signal model with arbitrary distributions for the observables used in the analysis. The production cross-section (σ) and the branching ratios (BR) depend on the model of interest. The experimental acceptance $A^{\text{experiment}}$ relates to the overall efficiency of the final selection criteria used in the analysis (Table 6-3). The parameterization is as follows:

- Generator-level H_T should be smeared using a Gaussian distribution with σ_{H_T} from Figure 6-35A and then a requirement of $H_T > 300$ GeV is to be applied,

- Generator-level $\not{E}_T$ should be smeared using a Gaussian distribution with $\sigma_{\not{E}_T}$ from Figure 6-35B and then a requirement of $\not{E}_T > 30$ GeV is to be applied

- 2 prompt same-sign leptons must be produced in the event

- Muons must have $p_T > 5$ GeV and $|\eta| < 2.4$

- Electrons must have $p_T > 10$ GeV and $|\eta| < 2.4$

- Non-prompt muons and electrons from signal events can be considered to be lost

- Selection efficiency (including reconstruction, identification and RelIso) for prompt muons and electrons is parameterized as in Eq. 6–14.

By applying these requirements to the generator-level objects coming from the Monte Carlo truth, one obtains the overall experimental acceptance $A^{\text{experiment}}$ for a wide range of models to pass the final selection.

Table 6-23 shows the values of parameters $\text{par}(1)$, $\text{par}(2)$, and $\text{par}(3)$. Table 6-24 summarizes the the values of the signal acceptance systematics (and also theoretical uncertainties for the LM0 benchmark point).

6.8 Final Results

Table 6-25 and Figure 6-24 summarize the expected and observed event yields, together with the estimated systematic errors. Only 1 event is observed to pass the final

Table 6-23. Observables used in the analysis and parameterization of their acceptance for signal-like events.

Observable used in the analysis	par(1)	par(2)	par(3)
Prompt muons with $p_T > 5$ GeV and $|\eta| < 1.2$	0.79	0.28	30
Prompt muons with $p_T > 5$ GeV and $1.2 < |\eta| < 2.4$	0.84	0.20	22
Or without subdividing into central/forward η regions	0.76	0.23	21
Prompt electrons with $p_T > 10$ GeV and $|\eta| < 1.5$	0.76	0.35	21
Prompt electrons with $p_T > 10$ GeV and $1.5 < |\eta| < 2.4$	0.57	0.38	14
Or without subdividing into central/forward η regions	0.68	0.37	17
$H_T > 300$ GeV, built from > 1 jets with $E_T > 30$ GeV and $|\eta| < 2.4$	$\sigma_{H_T} = 52$ GeV		
$\not{E}_T > 30$ GeV, built from observable transverse energy flow	$\sigma_{\not{E}_T} = 18$ GeV		

Table 6-24. Signal yields and systematic errors

	$\mu\mu$	ee	$e\mu$	Total
Expected signal events (LM0)	3.32	1.67	4.86	9.85
Isolated (prompt) muons with $p_T > 5$ GeV and $|\eta| < 2.4$ (6%)	12%	-	6%	-
Isolated (prompt) electrons with $p_T > 5$ GeV and $|\eta| < 2.4$ (10%)	-	20%	10%	-
Hadronic energy flow reconstruction	-	-	-	8%
Trigger	-	-	-	5%
Luminosity	-	-	-	11%
Total Experimental Acceptance Errors	19%	23%	19%	18%
LM0 cross section at NLO due to PDF uncertainties	-	-	-	13%
LM0 cross section at NLO due to QCD scale uncertainties	-	-	-	18%
Total errors for LM0	29%	32%	29%	32%

selection, which is consistent with the total background expectation of $N_{bkd}^{tot} = 0.80 \pm 0.33$. For comparison, if supersymmetry existed with the model parameters of LM0, a rate of 9.9 events would be expected (not counting the background). The "anatomy" of the observed event is discussed in the Appendix.

Given there is no observed excess of events in the signal region, it is natural to calculate exclusion limits. To this end, two results will be presented:

(i)   Limits on cross section times acceptance $\sigma \times BR \times A^{\text{experiment}}$

(ii) Limits on the mSUGRA parameters

Table 6-25. Summary of expected and observed event yields, together with the overall systematic errors

	$\mu\mu$	ee	$e\mu$	total
Total background estimate	0.30 ± 0.13	0.10 ± 0.07	0.40 ± 0.18	0.80 ± 0.33
Observed events	0	1	0	1
LM0 expectation	3.32	1.67	4.86	9.9
LM0 signal yield systematic errors	27%	30%	27%	26%

6.8.1 Limits on $\sigma \times BR \times A^{\text{experiment}}$

To calculate limits on cross-section times acceptance $\sigma \times BR \times A^{\text{experiment}}$, it is convenient to combine the three channels together into a single counting experiment.[10] Tables 6-24 and 6-25 provide all of the necessary information for setting the exclusion limits from this search. The expected background rate is 0.80 with a relative uncertainty of 38%. The error on the signal acceptance was determined to be 18%. It is assumed that the errors on the background measurement and the signal acceptance are uncorrelated and that they each follow a log-normal distribution for error pdf's. The Bayesian approach is used to set the limits using a flat prior pdf on $\sigma \times BR \times A^{\text{experiment}}$. Technically, the calculation is performed by the LandS software [76], which gives us the following result:

$$\sigma \times BR \times A^{\text{experiment}} < 0.13 \text{ pb at 95\% C.L.}$$

For comparison, the LM0 model predicts $\sigma \times BR \times A^{\text{experiment}} = 9.85/35 = 0.28$ pb and is therefore reliably excluded by this search.

Table 6-23 shows the values of the experimental acceptance parameterization. These parameters allow one to predict $\sigma \times BR \times A^{\text{experiment}}$ for any given model to test whether it is be excluded at 95% C.L. by this search. The NLO cross-section for LM0 is 57.6 pb. The theoretical acceptance for the selection requirements used in the analysis is about 1.2%, and the experimental acceptance is about 38%.

### 6.8.2 Limits on the mSUGRA Parameter Space

The event yields (using LO cross-sections) for a $\mathbf{m}_0$ vs. $\mathbf{m}_{1/2}$ mSUGRA parameter-plane with $\tan(\beta) = 3$, $\mathbf{A}_0 = 0$ GeV, and $\mu > 0$ are shown in Figure 6-37A. The `SoftSUSY` program [77] is used to calculate the SUSY particle mass spectrum. The `SUSY-Hit` program [78] is then applied in order to account for radiative corrections to the mass

---

[10] It was checked that doing a more sophisticated combination of three channels with a proper correlations of systematic errors gives negligible improvement

spectra and branching ratios. Signal events are then generated with Pythia6 [58] and filtered for two prompt leptons (e, μ and τ) with $p_T > 4$ GeV and $|\eta| < 2.5$. Finally, the events are propagated through the CMS Fast Simulation, which simulates the detector response, and then are subsequently reconstructed using version 3.8.6 of CMSSW. Due to the filter applied during the event generation step, some events in which one of the same-sign leptons is non-prompt, but happens to be isolated by accident, are lost. This loss is evaluated to be at the level of 5% according to the LM0 simulation sample. All models points on the plane that are expected to yield more than 4.5 events passing the final selection per 35 pb^{-1} are subsumed by the contour, and are hence excluded at 95% C.L.

It is important to show the level of precision obtainable from the parameterization provided in Table 6-23. Figure 6-37B compares two exclusion contours on the $\mathbf{m}_0$ vs. $\mathbf{m}_{1/2}$ plane. One is derived from the CMS Fast Simulation samples (solid blue curve), where the magenta band represents the theoretical uncertainty. Another is derived from the signal acceptance model described in Section 6.7.3, which is applied to generator-level objects (black dashed curve). NLO cross-sections are used for both curves.[11] The agreement between the two curves demonstrates the robustness of the signal acceptance parameterization in the context of mSUGRA. It gives those who are external to the CMS collaboration and cannot access or employ CMSSW or the CMS Fast Simulation a reliable way to test various models of new physics against the exclusion limits set by this search. Also shown in Figure 6-23 are the exclusions curves set by previous searches performed by other experiments, which are weaker, in general, than the limits set by this search.

---

[11] A common k-factor of 1.5 is used for all model points on the plane
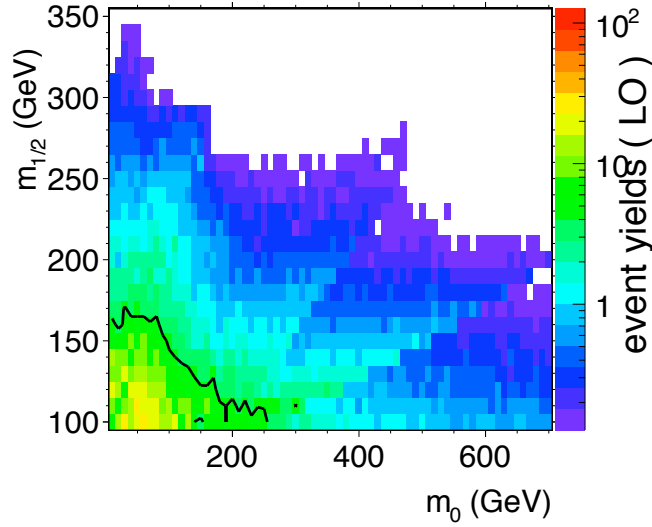
A Event yields at LO
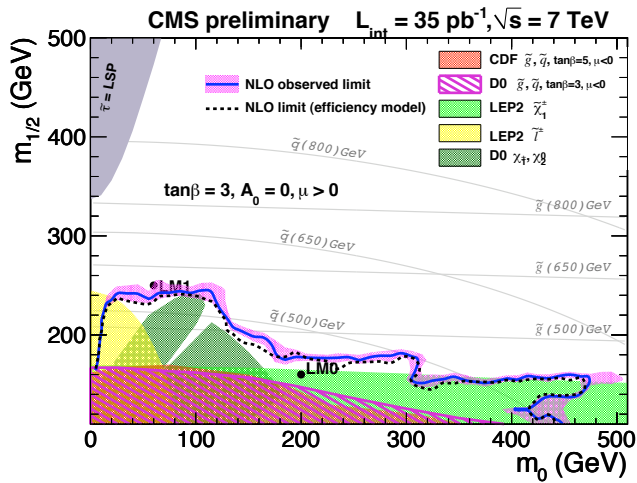
B Exclusion contours

Figure 6-37. Expected event yields for mSUGRA models on the $\mathbf{m}_0$ - $\mathbf{m}_{1/2}$ plane for 35 pb^{-1} of data (top). Exclusion contour in the $\mathbf{m}_0$ - $\mathbf{m}_{1/2}$ plane (bottom). Contours subsume all mSUGRA model points that yield more than 4.5 events per 35 pb^{-1} of data (i.e., $\sigma \times BR \times A^{\text{experiment}} > 0.13$ pb).

CHAPTER 7
CONCLUSION

The results of a search for a signal of new physics involving events with 2 same-sign leptons, jets, and missing transverse energy have been presented. This is the first search featuring this event topology to be performed at the LHC with the CMS experiment. It relies on data collected in the 2010 LHC run at a collision energy of $\sqrt{s} = 7$ TeV, and corresponds to a total integrated luminosity 35 pb^{-1}. In the signal region defined by the event selection criteria of this analysis, 1 event is observed, which is statistically consistent with the total expected background rate from the Standard Model of $N^{tot}_{bgd} = 0.80 \pm 0.33$ events. The main backgrounds to this search are predicted using a variety of robust data-driven methods, which have been thoroughly validated with collision data or in some cases with the help of simulations.

Given the lack of an observed excess of events in the defined signal region, exclusion limits are calculated on the parameter space of supersymmetry models with universal scalar and gaugino masses at the GUT scale. The general limit on the cross-section σ times the event acceptance, A, described above is $\sigma \times BR \times A^{\text{experiment}} <$ 0.13 pb at 95% C.L. A parameterization of the experimental acceptance, $A^{\text{experiment}}$, is also provided, which can be used to test a variety of models against the limits set by this search.

Efforts are underway to perform a similar search with the data recorded by the LHC in 2011, which is expected to be as much as a few inverse femtobarns by the end of the year. Preliminary studies indicate that the selection criteria used in this analysis will continue to be greatly sensitive to new physics processes featuring the studied topology up to approximately 400 pb^{-1}, beyond which the systematic uncertainties prohibit any further limit setting or discovery potential. It is expected that the statistical uncertainties incurred on the various components to the background measurements will scale inversely with the square-root of the integrated luminosity. Some data-driven

methods employed in this analysis may also be improved to perhaps decrease the incurred systematic uncertainties. It in anticipated that some version of this analysis will be carried out by the Summer of 2011, when the LHC increases the amount of collision data by over an order of magnitude. This author eagerly awaits this new opportunity to possibly make a discovery that will forever change our understanding of the fundamental particles.

APPENDIX: ANATOMY OF THE OBSERVED SIGNAL EVENT

After applying all the final selection requirements on 35 pb^{-1} of data, a single event survives from the *ee* channel. Event 156279004 was recorded during LHC Fill 1439 and CMS Run 148822 on October 24, 2010.

A 3-dimensional display depicts the topology of this surviving event in Figure A-1. For illustration purposes the muon system and tracking detectors are suppressed in the display. Labels denote the reconstructed particle flow jets, the two candidate same-sign electrons, and the particle flow $\not{E}_T$ vector. Tracks are depicted in green and are suppressed below $p_T < 0.5$ GeV. Hadronic and electromagnetic components of the calorimeter towers are represented by blue and red respectively. Energy components from calotowers with $E_T < 0.3$ GeV are suppressed. Reconstructed particle flow jets are shown in turquoise, while the electron tracks are displayed in blue. The $\not{E}_T$ vector is depicted by a red arrow and labeled "PFMet". There are two reconstructed primary vertices which are not visible in Figure A-1, but both electrons emerge from the same vertex located at (0.08593 cm, 0.0190 cm, 3.406 cm).

Kinematic and other details pertaining to these reconstructed objects are provided in Tables A-1, A-2, and A-3 for the jets, electrons, and $\not{E}_T$ respectively. The H_T calculation for this event yields a value of 337.6 GeV, which is safely above the threshold used in the analysis. None of the jets are identified as originating from b-quarks by the "Track Counting High Purity" discriminator denoted by the column heading "B-Tag" in Table A-1. Typically, b-jets will have values above 3.0 for this variable. The leading jet does point directly toward the transition region of the ECAL Barrel and ECAL Endcap, where the jet energy response can tend to be compromised. This effect should be compensated for by the jet energy scale corrections performed on the particle flow jets.

As can be seen from Figure A-1, the event is rather clean. The electrons are well separated from one another as well as the jets in the event. The lesser isolated of the two electrons (i.e. e_2) just barely passes the $\text{RelIso} < 0.15$ requirement (calculated with

cone size of $\Delta R = 0.3$) ; however, it would fail if the cone were enlarged to $\Delta R = 0.4$, while the more isolated electron would continue to pass easily as is shown in Table A-2. This may be a hint that the former may not actually be a prompt electron.

Table A-3 shows the $\not{E}_T$ calculations as performed by various algorithms which are executed during the event reconstruction. Particle Flow $\not{E}_T$ and Track-Corrected Calo-$\not{E}_T$ are considered to have the best performance and their magnitudes agree to within 7 GeV. The former, which is used in this analysis, is well beyond the selection requirement of 30 GeV.

More data will be needed to draw any further conclusions about the viability of this event to serve as a candidate for new physics. Its observation is perfectly consistent with the Standard Model expectation for this analysis.

Table A-1. Summary of jet content in observed signal event

Label	P_T (GeV)	η	ϕ (rad)	EM Fraction	B-Tag	ΔR(jet,e_1)	ΔR(jet,e_2)
J_1	156.9	1.47	-2.14	0.310	1.69	3.64	0.91
J_2	83.5	-1.35	-2.90	0.045	-0.73	2.99	2.95
J_3	58.9	2.03	1.95	0.093	-0.50	3.53	1.37
J_4	38.6	1.45	0.26	0.294	0.20	2.59	3.00

Table A-2. Summary of leptons attributes in observed signal event

Label	P_T (GeV)	η	ϕ (rad)	q	d_0 (mm)	RelIso (Cone=0.3)	RelIso (Cone=0.4)
e_1	75.9	-1.14	0.40	-1	0.015	0.000	0.0458
e_2	20.0	1.60	-3.04	-1	-0.006	0.144	0.363

Table A-3. Summary of $\not{E}_T$ calculations in observed signal event

Algorithm	E_T (GeV)	ϕ (rad)
Particle-Flow $\not{E}_T$	45.6	0.52
Track-corrected calorimeter $\not{E}_T$	52.6	0.66
Raw calorimeter $\not{E}_T$	23.5	1.00
TypeI-corrected calorimeter $\not{E}_T$	113.0	0.43

PFMet

J_4

J_3

e_1

e_2

J_1

J_2

CMS Experiment at LHC, CERN
Data recorded: Sun Oct 24 09:04:09 2010 EDT
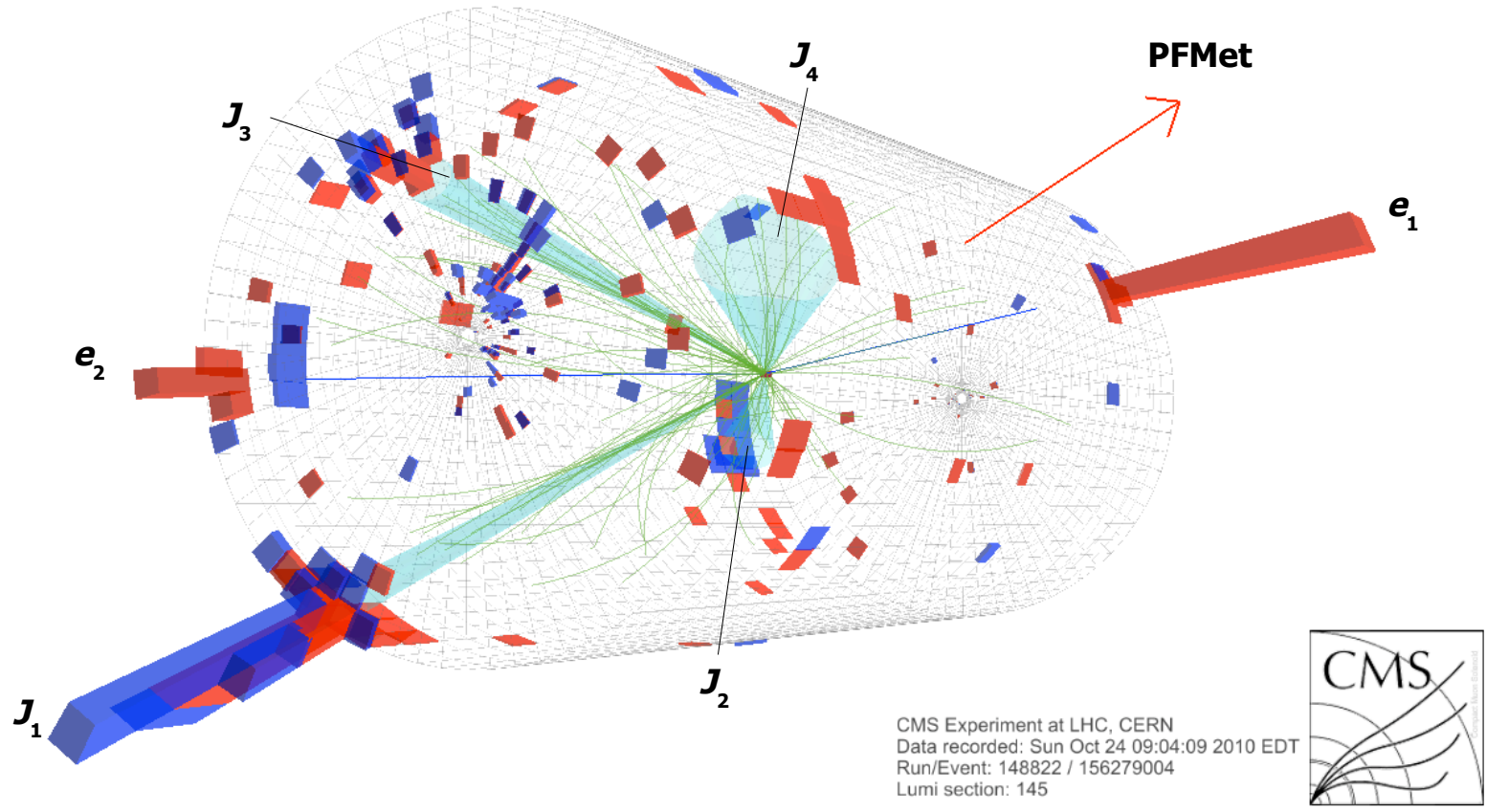Run/Event: 148822 / 156279004
Lumi section: 145

CMS

Figure A-1. 3D event display of the *ee* event observed in the signal region

REFERENCES

[1] D. Gross and F. Wilczek, "Ultraviolet Behavior of Non-Abelian Gauge Theories", *Phys. Rev. Lett.* **30** (1973) 1343–1346.

[2] S. Weinberg, "A Model of Leptons", *Phys. Rev. Lett.* **19** (1967) 1264–1266.

[3] M. Maltoni et al., "Status of global fits to neutrino oscillations", *New Journal of Physics* **6** (2004), no. 1, 122.

[4] L. Wolfenstein, "Neutrino oscillations in matter", *Phys. Rev.* **D17** (1978) 2369–2374.

[5] Super-Kamiokande Collaboration, "Evidence for oscillation of atmospheric neutrinos", *Phys. Rev. Lett.* **81** (1998) 1562–1567, arXiv:hep-ex/9807003.

[6] J. Hanc, S. Tuleja, and H. M., "Symmetries and conservation laws: Consequences of Noether's theorem", *American Journal of Physics* **72** (April, 2004) 428–435.

[7] M. Peskin and D. Schroeder, "An Introduction To Quantum Field Theory". Westview Press, 1995.

[8] P. Ramond, "Field Theory : A Modern Primer (Frontiers in Physics Series, Vol 74)". Westview Press, 2001.

[9] M. Srednicki, "Quantum Field Theory". Cambridge University Press, 2007.

[10] A. Zee, "Quantum Field Theory in a Nutshell: Second Edition". Princeton University Press, 2010.

[11] K. Nakamura and P. D. Group, "Review of Particle Physics", *Journal of Physics G: Nuclear and Particle Physics* **37** (2010), no. 7A, 075021.

[12] P. Mohr, B. Taylor, and D. Newell, "CODATA recommended values of the fundamental physical constants: 2006", *Rev. Mod. Phys.* **80** (Jun, 2008) 633–730.

[13] B. Delamotte, "A hint of renormalization", *Am. J. Phys.* **72** (Dec, 2002) 170–184. 10 p.

[14] G. 't Hooft, "Renormalization of Massless Yang-Mills Fields", *Nucl. Phys.* **B33** (1971) 173–199.

[15] B. Lee, C. Quigg, and H. Thacker, "Weak interactions at very high energies: The role of the Higgs-boson mass", *Phys. Rev. D* **16** (Sep, 1977) 1519–1531.

[16] D. Dicus and V. Mathur, "Upper Bounds on the Values of Masses in Unified Gauge Theories", *Phys. Rev. D* **7** (May, 1973) 3111–3114.

[17] J. Gunion et al., "The Higgs Hunter's Guide". Westview Press, 2000.

[18] G. Kane, "Modern Elementary Particle Physics: Updated Edition". Westview Press, 1993.

[19] R. Mohapatra and G. Senjanović, "Neutrino Mass and Spontaneous Parity Nonconservation", *Phys. Rev. Lett.* **44** (Apr, 1980) 912–915.

[20] S. Martin, "A Supersymmetry Primer", arXiv:hep-ph/9709356.

[21] H. Baer and X. Tata, "Weak Scale Supersymmetry: From Superfields to Scattering Events". Cambridge University Press, 2006.

[22] S. Dimopoulos and D. Sutter, "The supersymmetric flavor problem", *Nuclear Physics B* **452** (1995), no. 3, 496 – 512.

[23] M. Guchait and D. Roy, "Like-sign dilepton signature for gluino production at the CERN LHC including top quark and Higgs boson effects", *Phys. Rev. D* **52** (Jul, 1995) 133–141.

[24] H. Dreiner, M. Guchait, and D. Roy, "Like sign dilepton signature for gluino production at the CERN LHC with or without R conservation", *Phys. Rev. D* **49** (Apr, 1994) 3270–3282.

[25] R. Barnett, J. Gunion, and H. Haber, "Discovering supersymmetry with like-sign dileptons", *Physics Letters B* **315** (1993), no. 3-4, 349 – 354.

[26] K. Matchev and D. Pierce, "New backgrounds in trilepton, dilepton and dilepton plus tau jet SUSY signals at the Tevatron", *Phys. Lett.* **B467** (1999) 225–231, arXiv:hep-ph/9907505.

[27] K. Matchev and D. Pierce, "Supersymmetry reach of the Tevatron via trilepton, like sign dilepton and dilepton plus tau jet signatures", *Phys. Rev.* **D60** (1999) 075004, arXiv:hep-ph/9904282.

[28] H. Cheng, K. Matchev, and M. Schmaltz, "Bosonic supersymmetry? Getting fooled at the CERN LHC", *Phys. Rev. D* **66** (Sep, 2002) 056006.

[29] F. Almeida, Jr. et al., "Same-sign dileptons as a signature for heavy Majorana neutrinos in hadron-hadron collisions", *Physics Letters B* **400** (1997), no. 3-4, 331 – 334.

[30] Y. Bai and Z. Han, "Top-antitop and Top-top Resonances in the Dilepton Channel at the CERN LHC", *J. High Energy Phys.*

[31] G. Kane et al., "Study of constrained minimal supersymmetry", *Phys. Rev. D* **49** (Jun, 1994) 6173–6210.

[32] M. Battaglia et al., "Proposed post-LEP benchmarks for supersymmetry", *Eur. Phys. J.* **C22** (2001) 535–561, arXiv:hep-ph/0106204.

[33] Muon $g - 2$ Collaboration, "Measurement of the Negative Muon Anomalous Magnetic Moment to 0.7 ppm", *Phys. Rev. Lett.* **92** (Apr, 2004) 161802.

[34] CDF Collaboration, "Inclusive Search for New Physics with Like-Sign Dilepton Events in $p\overline{p}$ Collisions at $\sqrt{s} = 1.96$ TeV", *Phys. Rev. Lett.* **98** (Jun, 2007) 221803.

[35] D∅ Collaboration, "Search for associated production of charginos and neutralinos in the trilepton final state using 2.3 fb-1 of data", *Physics Letters B* **680** (2009), no. 1, 34 − 43.

[36] D∅ Collaboration, "Search for squarks and gluinos in events with jets and missing transverse energy using 2.1 fb^{-1} of $p\overline{p}$ collision data at $\sqrt{s}$=1.96 TeV", *Phys. Lett. B*.

[37] "LHC Machine", *JINST* **3** (2008), no. 08, S08001.

[38] CMS Collaboration, "The CMS experiment at the CERN LHC", *JINST* **3** (2008), no. 08, S08004.

[39] ATLAS Collaboration, "The ATLAS experiment at the CERN Large Hadron Collider", *JINST* **3** (2008), no. 08, S08003.

[40] ALICE Collaboration, "The ALICE experiment at the CERN LHC", *JINST* **3** (2008), no. 08, S08002.

[41] LHCb Collaboration, "The LHCb Detector at the LHC", *JINST* **3** (2008), no. 08, S08005.

[42] LCHf Collaboration, "The LHCf Detector at the CERN Large Hadron Collider", *JINST* **3** (2008), no. 08, S08006.

[43] TOTEM Collaboration, "The TOTEM Experiment at the CERN Large Hadron Collider", *JINST* **3** (2008), no. 08, S08007.

[44] "Summary of the analysis of the 19 September 2008 incident at the LHC.", technical report, CERN, Geneva, Oct, 2008.

[45] "LHC to run at 3.5 TeV for early part of 2009-2010 run rising later", Technical Report CERN PR13.09, CERN, Geneva, August, 2009.

[46] "Annual Report", Technical Report CERN Annual report 2009, Geneva.

[47] CMS Collaboratoin, "CMS Luminosity Public Results", April, 2011. https://twiki.cern.ch/twiki/bin/view/CMSPublic/LumiPublicResults2010.

[48] CERN, "Chamonix 2011 Workshop on LHC Performance". CERN, Geneva, (2011). Organiser: Steve Myers.

[49] CMS Collaboration, "Electromagnetic calorimeter commissioning and first results with 7 TeV data", Technical Report CMS-NOTE-2010-012, CERN, Geneva, July, 2010.

[50] E. Yazgan, "The CMS Barrel Calorimeter Response to Particle Beams from 2 to 350 GeV/c. oai:cds.cern.ch:1127308", Technical Report CMS-CR-2008-040, CERN, Geneva, June, 2008.

[51] S. Abdullin et al., "Design, performance, and calibration of CMS forward calorimeter wedges", *The European Physical Journal C - Particles and Fields* **53** (2008) 139–166. 10.1140/epjc/s10052-007-0459-4.

[52] "The CMS muon project: Technical Design Report". Technical Design Report CMS. CERN, Geneva, 1997.

[53] G. Charpak, "High-accuracy, two-dimensional read-out in multiwire proportional chambers", *Nuclear Instruments and Methods*.

[54] F. Rademakers and R. Brun, "ROOT: an object-oriented data analysis framework", *Linux J.* **1998** (July, 1998).

[55] D. Lange, "The CMS Reconstruction Software", Technical Report CERN-CMS-CR-2011-002, CERN, Geneva, Jan, 2011.

[56] G. Brumfiel, "High-energy physics: Down the petabyte highway", *Nature News* (Jan, 2011).

[57] J. Alwall et al., "MadGraph/MadEvent v4: the new web generation", *Journal of High Energy Physics* **2007** (2007), no. 09, 028.

[58] T. Sjostrand, M. S., and P. Skands, "PYTHIA 6.4 Physics and Manual", *JHEP* **05** (2006) 026.

[59] J. Allison et al., "Geant4 developments and applications", *IEEE Transactions on Nuclear Science* **53** (Feb, 2006) 270–278.

[60] CMS Collaboration, "Comparison of the Fast Simulation of CMS with the first LHC data",.

[61] CMS Collaboration, "Search for new physics with same-sign isolated dilepton events with jets and missing transverse energy at the LHC", *JHEP* **06** (2011) 077, arXiv:1104.3168.

[62] R. H. W. Beenakker and M. Spira, "PROSPINO: A Program for the Production of Supersymmetric Particles in Next-to-leading Order QCD", arXiv:hep-ph/9611232.

[63] ATLAS Collaboration, "Search for Supersymmetry Using Final States with One Lepton, Jets, and Missing Transverse Momentum with the ATLAS Detector in $\sqrt{s} = 7\ TeV\ pp$ Collisions", *Phys. Rev. Lett.* **106** (Mar, 2011) 131802.

[64] CMS Collaboration, "Search for Physics Beyond the Standard Model in Opposite-Sign Dilepton Events at sqrt(s) = 7 TeV", arXiv:1103.1348.

[65] CMS Collaboration, "Search for supersymmetry in pp collisions at 7 TeV in events with jets and missing transverse energy", *Physics Letters B* **698** (2011), no. 3, 196 – 218.

[66] CMS Collaboration, "Performance of muon identification in pp collisions at $\sqrt{s}$ = 7 TeV", *CMS Physics Analysis Summary* **CMS-PAS-MUO-10-002** (2010).

[67] CMS Collaboration, "Electron reconstruction and identification at $\sqrt{s}$=7 TeV", *CMS Physics Analysis Summary* **CMS-PAS-EGM-10-004** (2010).

[68] CMS Collaboration, "Commissioning of the Particle-Flow Reconstruction in Minimum-Bias and Jet Events from pp Collisions at 7 TeV", *CMS Physics Analysis Summary* **CMS-PAS-PFT-10-002** (2010).

[69] CMS Collaboration, "Particle–Flow Event Reconstruction in CMS and Performance for Jets, Taus, and $\not{E}_T$", *CMS Physics Analysis Summary* **CMS-PAS-PFT-09-001** (2009).

[70] M. Cacciari, G. Salam, and G. Soyez, "The anti-k_T jet clustering algorithm", *JHEP* **04** (2008) 063.

[71] CMS Collaboration, "Jets in 0.9 and 2.36 TeV pp Collisions", *CMS Physics Analysis Summary* **CMS-PAS-JME-10-001** (2010).

[72] CMS Collaboration, "Jet Performance in pp Collisions at $\sqrt{s}$=7 TeV", *CMS Physics Analysis Summary* **CMS-PAS-JME-10-003** (2010).

[73] W. Beenakker et al., "Squark and Gluino Production at Hadron Colliders", *Nuclear Physics B* **492** (1997) 51.

[74] CMS Collaboration, "Measurement of CMS Luminosity", *CMS Physics Analysis Summary* **CMS-PAS-EWK-10-004** (2010).

[75] CMS Collaboration, "Measurement of the W and Z inclusive production cross-sections at $\sqrt{s} = 7$ TeV with the CMS experiment at the LHC", *CMS Physics Analysis Summary* **CMS-PAS-EWK-10-002** (2010).

[76] M. Chen, "LandS: A statistical tool for calculating limits and significance", April, 2011. https://mschen.web.cern.ch/mschen/LandS/index.html.

[77] "SOFTSUSY: A program for calculating supersymmetric spectra", *Computer Physics Communications* **143** (2002), no. 3, 305 – 331.

[78] A. Djouadi, M. M. Muhlleitner, and M. Spira, "Decays of Supersymmetric Particles: the program SUSY-HIT (SUspect-SdecaY-Hdecay-InTerface)", *Acta Phys. Polon.* **B38** (2007) 635–644.

BIOGRAPHICAL SKETCH

Ronald Charles Remington ("Ronny") was born in Daytona Beach, Florida to Thomas and Angel Remington. Ronny grew up in Ormond Beach, Florida and attended Seabreeze High School. During the winter of 2002, he was invited to compete against a hundred other high school students for the James Edward Oglethorpe (JEO) scholarship, a prestigious award that granted 4 years of full tuition, room and board to attend Oglethorpe University, a selective liberal arts school in Atlanta, Georgia. The competition featured a discussion session and a writing component, with each focused on Thomas Kuhn's philosophical work, "The Structure of Scientific Revolutions". It was during his preparations for this competition that he first encountered some of the revolutionary ideas that initiated the era of modern physics. He was quickly romanticized by these ideas, and as a result was able to discuss them fluently in the context of Kuhn's work. His performance during the competition earned him the scholarship. He accepted and enrolled in the Fall of 2002 as a student-athlete playing for the varsity soccer team and as a JEO scholar. While at Oglethorpe, Ronny earned a B.Sc. degree in physics with honors with a second major in mathematics. Upon graduating he enrolled at the University of Florida for graduate school in physics, where he joined the experimental high-energy physics group and later the CMS collaboration under the direction of Professor John Yelton.